A New Spin on Horizontal-Branch Stars: Anomalous Abundances and Rapid Rotation Rates

Thesis by

Bradford B. Behr

In Partial Fulfillment of the Requirements

for the Degree of

Doctor of Philosophy

California Institute of Technology

Pasadena, California

2000

(Submitted 16 May 2000)

Acknowledgments

I am deeply indebted to both of my thesis advisors, Jim McCarthy and Judy Cohen, for their guidance and support throughout the formulation, execution, and completion of this research project. Jim patiently tutored me on the finer points of stellar physics, echelle design, observing techniques, spectral reduction, and abundance analysis. More importantly, though, he put me in the driver's seat and gave me a chance to prove that I knew what I was doing, even entrusting me with much precious HIRES time. These results would not have reached fruition without Judy, who skillfully balanced my intellectual autonomy with the need to get the damn thing done. Her comments and suggestions (not to mention additional Keck time) were invaluable in refining the analyses, and I benefited enormously from her experience and wisdom throughout the publication process and job search.

Members of my thesis committee also played significant roles in this project, and in my development as a professional scientist. George Djorgovski made many valuable contributions to the scientific aspects of this work, from the suggestion to examine M13 and its prominent gap (including the contribution of observing time towards this end), to the subtle bit of wordplay that comprises the title of this document. Roger Blandford not only served on the committee, but furthermore, has taught me much of what I know about teaching, and I hope to someday possess a small fraction of the lecturing skill that he exhibited in Ay 1. Thanks also go to Neill Reid for guidance with aspects of the photometry, and to Peter Goldreich for stepping in on short notice to fill Neill's spot on the committee.

This work would not have been possible without the prodigious collecting area of the Keck I telescope and the exquisite spectral resolution of the HIRES spectrograph. I applaud Jerry Nelson, Gerry Smith, Steve Vogt, and many others for creating such marvelous machines, and salute a bevy of Keck observing assistants, including Joel Aycock, Teresa Chelminiak, Barbara Schaefer, and Terry Stickel, for making them work.

Although Palomar data did not figure directly in these results, my observing time on the 200-inch and 60-inch played an integral role in my development as an observer, and I always enjoyed visits to my "summer home" in the mountains. Thanks go to Skip Staples, Karl Dunscombe, and Rick Burruss for their steady hands on the telescope helms; to Hal

Petrie, John Henning, Steve Kunsman, Jeff Phinney, Dave Tennent, and Greg Van Idsinga for keeping the old scopes humming like new; to Bob Thicksten, Mike Doyle, and Merle Sweet for keeping the aforementioned crew in line; to Jean Mueller and Kevin Rykoski for their hospitality over at the 48-inch dome; to Bob Brucato, Anna-Marie Hetman, and Carlton Parker for on-campus administrative operations; and finally to Dipali and Rose for the best observatory cuisine in the observable universe.

In the near field, I owe many of the denizens of Robinson a huge debt of gratitude. Cheryl Southard provided a marvelous computing environment, and tolerated my scratch space hogging and quota overflows. I thank Shri Kulkarni, in his capacity as department EO, for his efforts to foster a positive environment for the students, and for generous supplementary financial support at various junctures. Lastly, I am convinced that the department would fall apart without Diane Fujitani, Gita Patel, Sandy Lester, Nanci Candelin, plus the rest of the admin staff, and then we wouldn't get any science done at all.

I made use of many excellent software tools and databases in pursuit of these results. Michael Lemke's LINFOR package and Robert Kurucz's ATLAS atmosphere modeling codes played a pivotal role, and I thank both authors for making these facilities available. Tim Pearson's PGPLOT is more than pretty good; it rocks. Photometric data from Manuela Zoccali and Patrick Durrell were instrumental in specifying photospheric parameters for the key clusters M13 and M15. I saved many hours (and many many trees) thanks to the online NASA ADS literature archives and the ADC and Simbad data repositories.

And finally, I have been enormously lucky to have such friends, both within and beyond the department, to keep me sane, fed, entertained, and happy: Roy, for good tunes in the office (not including the Hungarian rock opera); Pensri, for the pumpkin soup and other exquisite comestibles; Steve and Dave, for doing the dishes and keeping the amps turned down; Brian, for weightlifting and beer; Yama, for barbeque *par excellence* and Trudy, for remarkable patience; Marc, for keeping the beat; Andrew, for sharing the soccer helm; Ben, for variety, ambience, and duck farming; Alice, for scintillating discussions as we jogged through the early morning mists; Dave, for also caring about teaching people; Virginia, for making me laugh and keeping me distracted during the final months; PJ and Jared, for providing refuge in Northern California; Beaker, for high lift and low drag; Ali, for handling the art and language so I could be a Philistine power-geek; and Mom & Dad, for both the nature and the nurture, and 30 years of love and support.

Abstract

High-resolution spectroscopy of blue horizontal-branch stars in metal-poor globular clusters reveals remarkable differences in photospheric composition and rotation rate between cooler and hotter stars. For the cooler stars ($T_{\rm eff} < 11000\,{\rm K}$), the derived abundances are in good agreement with the canonical cluster metallicities, and we confirm the range of $v \sin i$ rotation velocities, some as high as $40\,{\rm km\,s^{-1}}$, previously reported in the literature. In the hotter stars, however, metals are enhanced by factors of 100 or more, and helium is depleted by as much as two orders of magnitude. In addition, the hot stars are almost exclusively slow rotators, with $v \sin i < 8\,{\rm km\,s^{-1}}$. The anomalous abundances are due to atomic diffusion mechanisms — gravitational settling of helium, and radiative levitation of metals — in the stable, non-convective atmospheres of these hot stars. The enhanced metal content in the stellar photospheres can alter the emergent spectral energy distributions, creating the photometric "gaps" observed in the clusters' color-magnitude diagrams. We discuss the connections between rotation and the diffusion mechanisms, and explore potential implications regarding the internal structure and evolution of these stars.

Contents

List of Figures

List of Tables

Chapter 1 Introduction

Globular clusters (GCs) are comprised of chemically homogeneous and coeval populations of stars, and therefore represent excellent systems for testing stellar models. Observations of the photometric and spectroscopic properties of stars at different stages of stellar evolution, represented by the various sequences and branches that appear in a cluster's color-magnitude diagram (CMD), can be compared to predicted isochrones and loci, not only to evaluate the accuracy of the models, but also to derive fundamental characteristics of the clusters themselves, such as distance and age. This approach has played a pivotal role in the development of stellar astrophysics, and has also helped establish the proper scales for Galactic and extragalactic distances and cosmological ages.

The horizontal branch (HB), an evolutionary stage characterized by core helium burning and shell hydrogen burning, is particularly useful for probing a variety of aspects of post-main-sequence evolution because its photometric properties are very sensitive to stellar composition and structure. A particular star's position along the color axis of the HB, for instance, depends strongly on its metallicity and the amount of mass loss it encountered earlier in its evolution, so the distribution of stars along the HB locus offers important clues towards understanding the mechanisms which drive mass loss. In addition, stars that reside on the blue horizontal branch (BHB) have lost a significant fraction of their envelopes, and mass layers which were previously deep within the star are now visible at the surface, so we may gain some insights into the internal structure and dynamics of the star at earlier times.

However, it appears that our understanding of the HB phase and its precursors is incomplete, as many HB stars exhibit characteristics which are not adequately explained by canonical stellar theory. The wide variety of HB color morphologies observed in Galactic globular clusters, ranging from short stubby red HBs to long extended "blue tails," cannot be explained on the basis of cluster metallicity alone, and it has proven difficult to identify which other parameters may be relevant. Many clusters also show perplexing "gaps" in the distribution of stars along the BHB. Furthermore, measurements of individual BHB stars indicate that many are rotating much faster than one would predict, and that others have

anomalously low surface gravities.

The primary intent of this thesis project is to observe a representative sample of these BHB stars at high spectral resolution, to discover new clues regarding these peculiarities and their implications for larger issues. In particular, we investigate the surface composition and rotation rates of BHB stars spanning a range of effective temperatures in several different metal-poor GCs. In §2, we provide background regarding the evolutionary pathways that bring a star from the main sequence to the HB, and identify the factors and mechanisms that play a role in this process. Prior observational work on BHB stars, particularly measurements of their abundances and rotations, are summarized in §3. The target sample for this study is introduced in §4, and the observations, spectral reduction, and abundance and rotation measurement procedures are detailed in §5. We present our results in §6, and §7 describes our current understanding of the relevant mechanisms. In §8, we summarize our findings and their implications, and offer some suggestions for future research avenues.

Chapter 2 Evolutionary context

2.1 Overview of post-main-sequence stellar evolution

The observed characteristics of HB stars in globular clusters are closely tied to their prior evolution, so it is important to review the stages that an intermediate-mass star goes through in order to reach the HB. The stars that currently populate the HBs of old, metal-poor GCs were originally Population II main-sequence stars of $\sim 0.8 M_{\odot}$, powered by hydrogen core burning. After 10 to 12 Gyr of main-sequence lifetime, all of the hydrogen in the core is converted to helium, and the fusion moves to a thick shell surrounding the inert helium core. The luminosity of this hydrogen-burning shell exceeds that of the original main-sequence core, and the star swells in diameter, moving redwards in the HR diagram along the subgiant branch. As the helium core accretes mass and becomes more degenerate, the luminosity of the hydrogen-burning shell continues to rise, and the star ascends the red giant branch (RGB), increasing in diameter and luminosity while maintaining a roughly constant effective temperature.

As the star's envelope expands and cools, the surface gravity diminishes, and coupled with the increased photospheric opacity and luminosity, this leads to strong mass loss, particularly at the uppermost tip of the RGB. The amount of envelope mass that is lost depends strongly on the luminosity of the hydrogen-burning shell, and the time spent in this high-luminosity phase. The exact mechanisms underlying RGB mass loss are still poorly understood, but from the observed photometric morphologies of later phases of evolution, we know that as much as 0.1–0.3 $M_{\odot}$ must be removed from the star during this stage.

The star's ascent of the RGB does not continue indefinitely, of course. The fusion shell has been producing helium "ash" at an ever-increasing rate, and the degenerate helium core grows more and more massive. Ultimately, at $M_{\rm core} \simeq 0.5 M_{\odot}$, the central temperature and pressure in the core becomes high enough to ignite triple-α helium fusion. Because the core is supported by degeneracy pressure, not thermal gas pressure, the equilibrium which normally governs the fusion reaction rate is not present, and the 3-α reaction spreads rapidly throughout the core in the so-called "helium flash." The resulting addition of

thermal energy to the core lifts the degeneracy and prompts a significant reorganization of the star's internal structure. A nondegenerate helium-burning core is established, and the hydrogen-burning shell is reduced in luminosity because the steep pressure gradient above the degenerate core is no longer present. When the star regains equilibrium, then, it is less luminous, but appears at a higher $T_{\rm eff}$, because the enormous convective envelope of the red giant stage has disappeared and the stellar diameter has decreased significantly.

The star spends roughly 100 Myr on the HB, decreasing slightly in surface temperature and increasing slightly in luminosity as more helium is deposited upon the core by the H-burning shell. Eventually, helium becomes depleted in the center of the core, and the triple-α burning moves to a shell around the inert carbon and oxygen that now occupies the center, in a manner closely analogous to the previous departure from the main sequence. If the envelope is sufficiently massive ($M_{\rm env} > 0.1 M_{\odot}$), and can provide enough pressure to maintain the shell burning, the star evolves upwards and redwards into an asymptotic giant-branch (AGB) star, which will ultimately shed nearly all of its remaining envelope via thermal pulsations and stellar winds to become a planetary nebula. If the HB envelope is too small, the star will increase in luminosity but then turn bluewards, appearing briefly as a so-called AGB-manqué object before joining the white dwarf cooling track.

2.2 HB color morphology and the second-parameter problem

The actual effective temperature of a given horizontal-branch star, and thus its position along the color axis in a cluster's color-magnitude diagram (CMD), depends primarily on its metallicity and its envelope-to-core mass ratio. Both of these parameters determine the amount of radiative opacity that lies between the interior energy generation sources and the photosphere. With a more massive and thus physically larger envelope, the luminosity generated in the stellar interior is distributed over a larger surface area, such that a smaller photospheric $T_{\rm eff}$ is required. Similarly, a more metal-rich envelope will present a larger opacity per unit mass, and will expand to a larger radius than otherwise, again increasing the surface area and decreasing surface temperature. The parallel influence of [Fe/H] and $M_{\rm env}$ upon $T_{\rm eff}$ is illustrated in Figure 2.1, which shows predicted zero-age horizontal branch (ZAHB) loci for a range of metallicities.

We can extend this picture of the behavior of individual stars in order to explain the

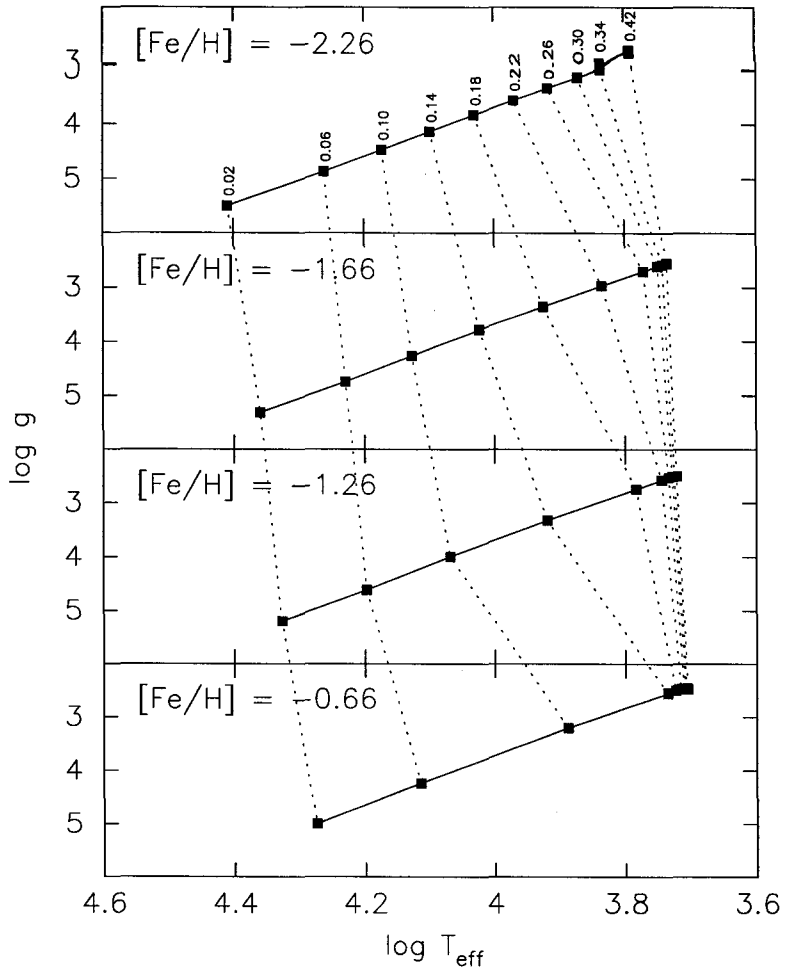

Figure 2.1: Models of ZAHB (zero-age horizontal branch) loci for a selection of cluster metallicities. The fiducial marks along each locus represent specific values for the envelope mass, as labelled in the uppermost panel. Based on data from Lee *et al.* (1994).

overall color distribution of HB stars in different globular clusters. Since GCs (with a very few exceptions) are taken to be chemically homogeneous systems, the *ab initio* metallicity of the HB stars in a single cluster is assumed to be the same, and the spread in color observed in most cluster HBs is due to different amounts of mass loss suffered by each star. Differences in HB morphology from cluster to cluster can thus be readily attributed to their differing metallicities, as first noted by Sandage & Wallerstein (1960). Metal-rich clusters tend to have short red HBs, while metal-poor clusters exhibit predominantly blue HBs. Cluster metallicity, then, is considered the "first parameter" influencing HB color morphology. Figure 2.2 contrasts the CMDs of three "typical" clusters — one metal-poor, one intermediate-metallicity, one metal-rich — and Figure 2.3 shows the overall trend linking metallicity to color morphology, as parameterized by the relative number of HB stars to

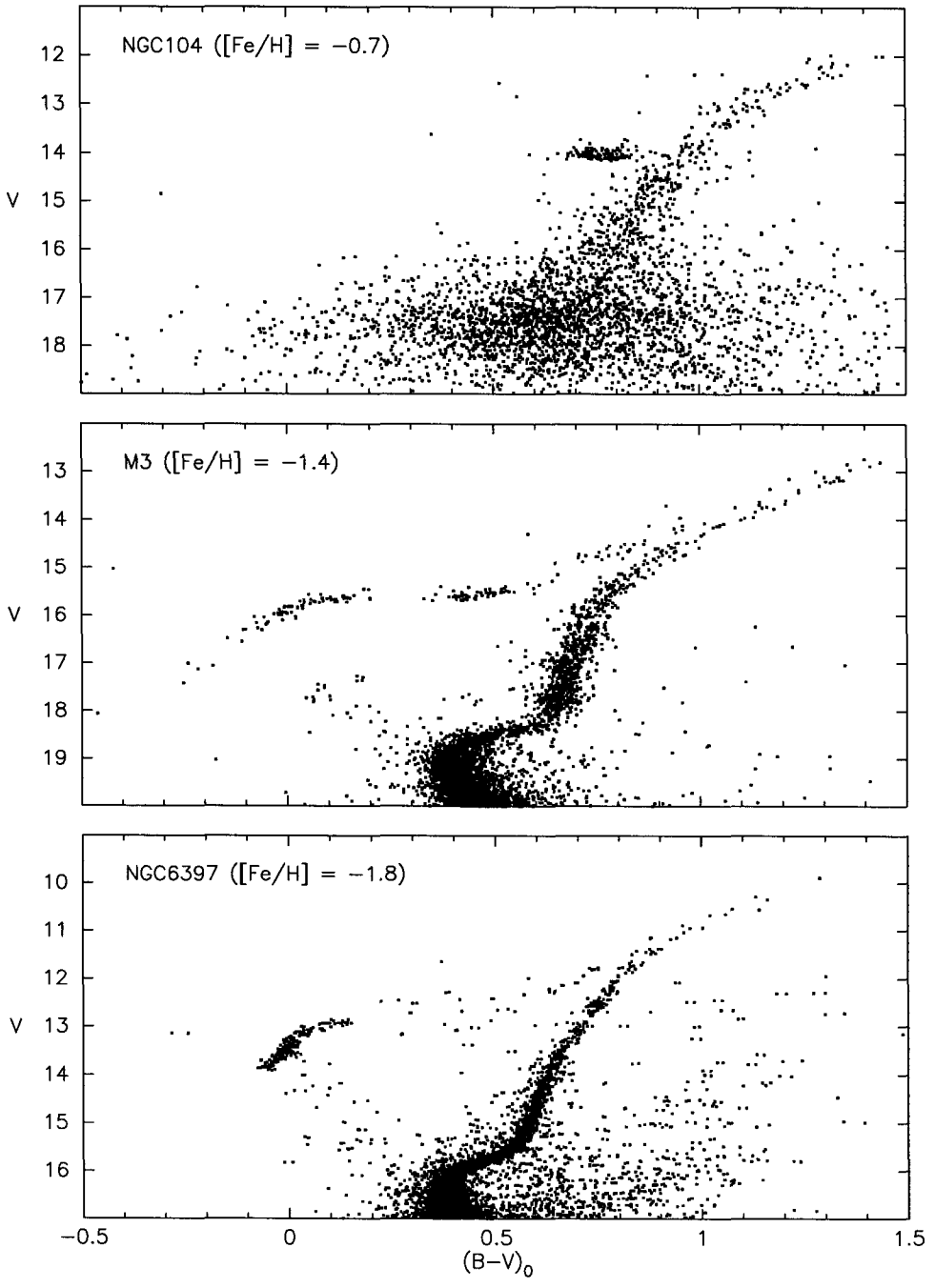

Figure 2.2: Color-magnitude diagrams of three globular clusters: metal-rich NGC104, intermediate-metallicity M3, and metal-poor NGC6397. The bluewards extent of the HB increases as metallicity decreases, according to the first-parameter effect.

either side of the instability strip.

However, some other global parameter in addition to metallicity must also be at work, as clusters with nearly identical [Fe/H] can show very different HB color distributions (van den Bergh, 1967; Sandage & Wildey, 1967; Rich *et al.*, 1997; Laget *et al.*, 1998). This "second parameter" was initially thought to be cluster age (Searle & Zinn, 1978; Lee *et al.*, 1994; Stetson *et al.*, 1996), which would determine the turnoff mass and thus alter the amount of available envelope mass. Age differences are not the only possible explanation, however, as several alternative or additional second-parameter candidates have since been suggested, including helium abundance and mixing (Sweigart, 1997), CNO abundance (Rood & Seitzer, 1981), central concentration of the cluster (Fusi Pecci *et al.*, 1993; Buonanno *et al.*, 1997), and distribution of stellar rotation rates (Peterson *et al.*, 1995). The potential influence of each of these factors is still very much an open question. For a more comprehensive review of the second-parameter problem, see Fusi Pecci & Bellazzini (1998).

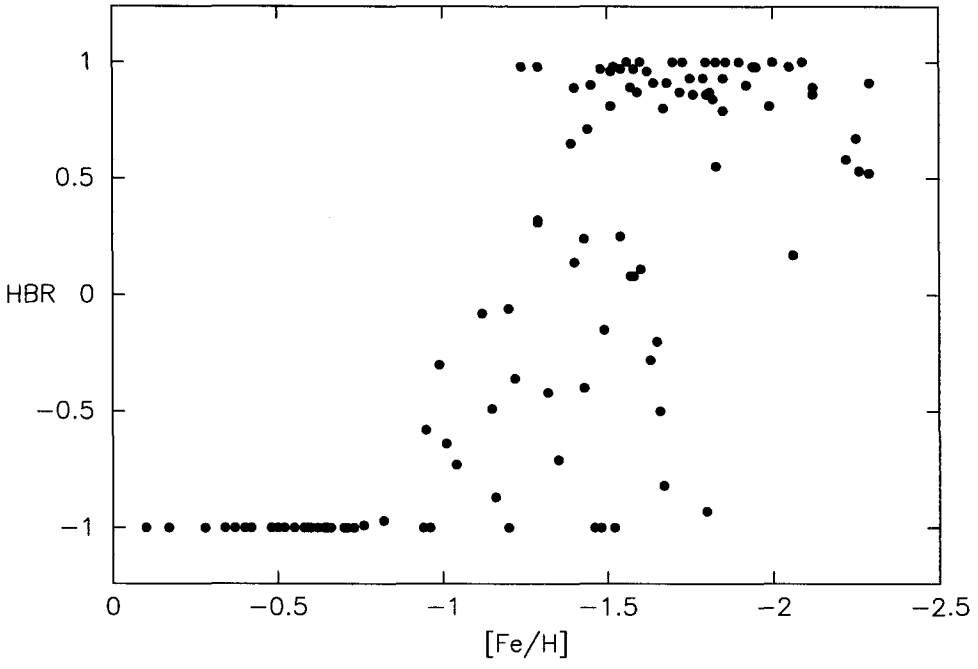

Figure 2.3: Horizontal-branch morphology as a function of metallicity for 115 Galactic globular clusters. The HB morphology is parameterized by the ratio HBR $= (B-R)/(B+V+R)$, where B, V, and R are the numbers of BHB, RR Lyrae, and RHB stars, respectively. Metal-poor clusters tend to have very blue HB distributions (HBR ~ 1), while metal-rich clusters generally contain only RHB stars (HBR ~ -1). Data are from the compilation of Harris (1996), including recent revisions.

2.3 Gaps and overluminosities along the HB

Further complicating this picture are the "gaps" which appear in the blue HB sequences of many globular clusters. Prominent gaps, such as the one at $(B-V)_0 \simeq 0.05$ in M15 (Buonanno *et al.*, 1983a), have been known for many years, but with the advent of higher-precision photometry, especially U-band measurements from the Hubble Space Telescope, analogous photometric features have appeared in many other clusters, including M13 and M80 (Ferraro *et al.*, 1997a, 1998), NGC2808 (Sosin *et al.*, 1997), NGC6229 (Catelan *et al.*, 1998), and NGC6273 (Piotto *et al.*, 1999). Although these gaps often appear quite "obvious" to the eye, their statistical significance is a topic of much debate, since standard tests, such as the Hawarden χ^2 algorithm (Hawarden *et al.*, 1971), assign them a much higher significance ($> 99\%$) than would be suggested by Monte Carlo simulations (Catelan *et al.*, 1998), where gaps appear in as many as 15% of the simulated HBs. A more compelling argument favoring significance rests on the observation that many of the observed gaps and underpopulated regions appear at very similar locations in different clusters (Ferraro *et al.*, 1998; Catelan *et al.*, 1998; Piotto *et al.*, 1999), as though they were due to some common physical mechanism.

If due to some universal aspect of mass-loss — a narrow range of "forbidden" envelope mass — then we would expect the photometric location of the gaps to vary with cluster metallicity, but such behavior is not observed. Another suggestion is that the gaps mark the boundaries between separate, discrete populations of HB stars, which differ in their origin or evolution, but again, the gaps are too clearly defined and consistently located for this to be a plausible explanation. Alternatively, Caloi (1999) suggests that the prominent $B-V \simeq 0$ gaps are not due to discontinuities in envelope mass or internal structure, but are instead a purely atmospheric effect. The disappearance of subsurface convection permits abundance variations (like those exhibited by chemically peculiar (CP) main-sequence stars) to appear in the hotter stars, altering the spectral energy distribution emerging from the photosphere.

Caloi's hypothesis is supported by photometric and spectrophotometric studies of the stars just bluewards of the $B-V \simeq 0$ gap. Moehler and her collaborators, in a series of papers (Moehler *et al.*, 1995, 1997a,b), have reported on measurements of BHB stars in several clusters, fitting observed Balmer line profiles and Balmer continuum slopes to atmospheric models, and deriving $T_{\rm eff}$ and $\log g$ for each star. For most of their BHB targets,

they find good agreement between the stars' positions in the theoretical HR diagram and the locus predicted by evolutionary models of BHB stars. However, for stars of intermediate temperature, $11000\,\mathrm{K} < T_{\mathrm{eff}} < 20000\,\mathrm{K}$, the observed $\log g$ are too small by several tenths of a dex. The magnitude of this "low-gravity jump" is small, but appears consistently in a number of different clusters, and has proven difficult to account for via luminosity evolution or higher helium content. A similar discontinuity in Strömgren u-band magnitude has been found by Grundahl *et al.* (1999) in M13, with the stars bluewards of $(u-y)_0 \simeq 0.8$ suddenly appearing at $\Delta u = -0.6\,\mathrm{mag}$ above the predicted locus. Since the locations of these "jumps" coincide with the photometric gap, it seems likely that the same mechanism is responsible for both, modifying the atmospheric opacities to produce unexpectedly high u-band fluxes (hence shifting the effected stars bluewards in the CMD) and anomalously low surface gravities.

2.4 Nomenclature

A wide variety of terminology has been used in the literature to describe the different color morphologies that appear among Galactic globular clusters, and the distinct regions along the HB locus. The HB is typically divided into the red horizontal branch (RHB) stars, the RR Lyrae variables, and the BHB stars. It is useful to subdivide the BHB further, although there does not yet appear to be a consensus regarding this partitioning. For the purposes of the current paper, we adopt the following nomenclature, illustrated in Figure 2.4:

- The **B′** stars are those that comprise the actual horizontal part of the BHB, as seen in a $B-V$ CMD. They lie between gap G1 and the instability strip, with effective temperatures ranging from 8000 to 11000 K, and $(B-V)_0$ colors of 0.00 to +0.20.

- Gap **G1** (following the notation of Ferraro *et al.* (1998)), appears at $(B-V) \simeq 0$, or $T_{\mathrm{eff}} \simeq 11000\,\mathrm{K}$. It is particularly prominent in the CMDs of M13, M15, and NGC288.

- The blue tail, or **BT** stars are found at higher T_{eff} than the B′ population, approximately $11000 - 20000\,\mathrm{K}$, between gaps G1 and G3. In a standard $(B-V, V)$ color-magnitude diagram, the blue tail assumes a vertical orientation, as the B and V bandpasses move on to the Raleigh-Jeans tail of the blackbody curve.

- Gap **G3** is at an effective temperature of approximately 20000 K. It is typically broader and less-sharply defined than G1, but common to nearly all clusters with extended blue HBs.

- The extended blue tail, or **EBT**, is the highest-temperature end of the BHB, reaching from gap G3 down to $T_{\rm eff} \simeq 30000$ K. These stars have lost nearly all of their original hydrogen envelopes, leaving only a thin $0.01 - 0.02 M_{\odot}$ layer over the helium core.

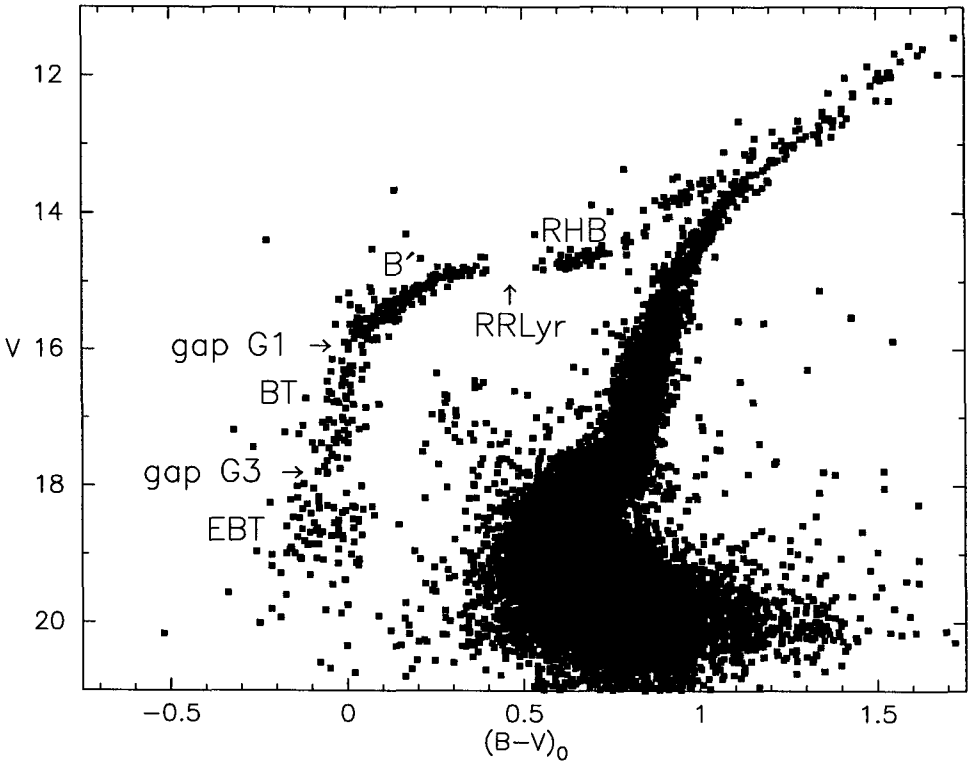

Figure 2.4: Labelled regions of the HB of a hypothetical globular cluster. The data are an amalgam of M3 and M13.

In discussing the chemical composition of our clusters and stars, we use the common abundance nomenclature of $\log \epsilon(\text{species}) = \log\left(N(\text{species})/N(\text{H})\right) + 12.0$, where N is the number density of atoms, and $[\text{species/H}] = \log \epsilon(\text{species}) - \log \epsilon(\text{species})_{\odot}$, *i.e.*, the logarithmic offset from the solar abundance of the given species or element.

Chapter 3 Prior work

Measurements of photospheric abundances and rotation rates of BHB stars have been made previously by several research teams. The prior observations have been limited to small sample sizes, or cover only a narrow spectral region, but the implications of these findings have provided the primary impetus for the current project. In this section, we review the relevant work reported in the literature.

3.1 Rotation

The vast majority of the existing work on rotation velocities of BHB stars has been done by Peterson and her collaborators, as described in a series of several papers (Peterson *et al.*, 1983, 1985a,b, 1995). Most of these observations were made using an echelle spectrograph in single-order mode, such that only a small region of spectrum, and hence a few metal absorption lines, were available to evaluate rotational broadening and photospheric abundances. For Peterson *et al.* (1995) (henceforth P95), this limited spectral coverage permitted them to use a multi-object fiber feed to observe many stars in parallel, and hence obtain a much larger sample size. Their observations were limited to the cool end of the BHB, mostly B′ stars, for which the V-band flux was high enough to provide sufficient signal, and where the absorption lines being used were strong enough to be seen. The rotation results for three of their clusters are included in Figure 6.11.

The most striking aspect of these results lies in the magnitude and distribution of the measured stellar rotation velocities. In one cluster, M13, some of the stars are found to be rotating as fast as $40\,\mathrm{km\,s^{-1}}$, while the peak $v \sin i$ in the other clusters are smaller, $20\,\mathrm{km\,s^{-1}}$, but still unexpectedly high. The progenitors of these BHB stars were of solar type and slightly later while on the main sequence, and are therefore expected to have had modest rotation rates, on the order of $2\,\mathrm{km\,s^{-1}}$, like the Sun. Even with the increase in radius and redistribution of moment of inertia as a star evolves from the main sequence to the HB, it is difficult to increase the surface velocity beyond 10 or $12\,\mathrm{km\,s^{-1}}$, so in order to explain the observed rotations, Peterson suggested several noncanonical scenarios,

including a rapidly-rotating stellar core, close encounters with a passing star, or absorption of close-orbit planets, in order to provide a source of additional angular momentum. These possibilities will be discussed in greater detail later.

More recently, Cohen & McCarthy (1997) observed five B′ stars in the cluster M92, using the Keck HIRES spectrograph to cover a much larger wavelength range and measure abundances of several chemical species in addition to rotation. These data have been subsumed into the current work and reanalyzed along with the rest of the sample, and the results are presented in §6.

3.2 Abundances

Detailed abundance analysis of BHB stars in globular clusters was attempted as early as 1981, but the first results considered to be accurate are those of Glaspey *et al.* (1989), who studied two stars in globular cluster NGC6752, one a B′ star at 10000 K, the other a BT star at 16000 K. They found a helium underabundance in the latter star, similar to those found for hot evolved stars in the nearby Galactic halo. Unexpectedly, analysis of the BT star also indicated an iron enhancement of 50 times above the cluster mean, while the B′ star had the same [Fe/H] as the cluster. The magnesium abundances were found to be near the cluster mean in both cases. These abundance patterns anticipate our results by a full decade, but strangely, were not followed up with further observations until recently.

A similar study was undertaken by Lambert *et al.* (1992), although their three target stars (two in M4, one in NGC6397) were all cooler B′-type, with $T_{\rm eff} \simeq 9000$ K. They found abundances fully in agreement with the canonical cluster metallicities, *i.e.*, no helium depletion or metal enhancement.

As part of their rotation analysis, Peterson *et al.* (1995) also include an estimate of the oxygen abundance, but because of the temperature uncertainties inherent in their photometry, they do not attempt to calculate an absolute [O/Fe] for these stars. They see hints of a decrease in [O/Fe] with increasing $T_{\rm eff}$, but this conclusion is not compelling.

High-precision abundance measurements of BHB stars spanning a range in $T_{\rm eff}$ have been performed recently by Moehler *et al.* (1999b), and confirm the Glaspey measurements in NGC6752. Their results closely parallel our own findings, and will therefore be discussed in §6.

Chapter 4 Target selection

In order to properly explore the connection between the characteristics of individual BHB stars and the photometric morphology of globular clusters, we must select targets from within a large multi-dimensional parameter space. Ideally, we would observe stars spanning the entire range of $T_{\rm eff}$, cluster metallicity, cluster HB morphology, cluster age, Galactocentric distance of the cluster, and central concentration of the cluster, so as to fully sample the possible second-parameter candidates. Realistically, though, with finite observing time and analysis resources, we can only measure a fraction of the stars in a fraction of the clusters. In this section, we present the rationale and specific target choices for our sample.

4.1 Previously-measured clusters

Four of the six clusters in our program set have been analyzed previously from the standpoint of stellar rotations and abundances. We reobserved a handful of the stars in these clusters in order to verify the previous determinations of $v \sin i$, and then observed many additional stars, both to improve the statistics of the $v \sin i$ sample, and to extend the rotation and abundance analysis to hotter stars.

- **M13** (NGC6205) is one of the closest and best-studied GCs in the Galactic system. Its HB lies entirely to the blue side of the instability strip, and reaches all the way down to the helium main sequence. Gaps G1 and G3 are prominent in its $(U-V, V)$ color-magnitude diagram. Five B′ and eight BT stars are included in our program, of which four are in common with Peterson *et al.* (1995). The other nine stars were selected from archival WFPC-2 UV photometry of the inner region of the cluster, reanalyzed by Zoccali (1998).

- **M3** (NGC5272) is frequently cited as the "second-parameter companion" of M13, as it has a nearly identical metallicity, but an even balance of BHB and RHB stars, with only a few stars in the blue tail. We have measured six members of the B′ population, all of them from P95.

- Five of the B′ stars in **M92** (NGC6341) were observed by Cohen & McCarthy (1997), as mentioned before, but a larger statistical sample was deemed necessary, so an additional 15 B′ stars, plus 2 BT stars, were added to the data set. M92's horizontal branch consists entirely of BHB stars, as one would expect for one of the most metal-poor clusters, but gap G1 is not well-defined, as the cluster's blue tail does not extend very far.

- **NGC288** has been sampled sparsely by our program — only four BT stars — as it was a last-minute substitute for M68, necessitated by telescope pointing limitations. However, it fits well into the data set, as it is of intermediate metallicity like M3 and M13, and exhibits a small but distinct gap G1 separating the B′ stars from a small BT. Its B′ population was well-observed by Peterson *et al.* (1995), so we can still make a rough comparison of rotation rates, even without having measured any B′ stars ourselves.

4.2 New clusters

The other two clusters in our sample have not been studied at high spectral resolution by any previous published work. They were chosen to probe the lowest-metallicity end of the nearby globular clusters.

- **M15** (NGC7078) has a similar metallicity as M92, and exhibits a similar CMD, albeit with a longer blue tail, extending from a large gap G1 down to gap G3. We have observed 18 stars in this cluster — 10 B′, and 8 BT.

- Although **M68** (NGC4590) is far to the south, it can be reached from Mauna Kea for a few hours every night in the spring months. Despite being extremely metal-poor like M15 and M92, it has a sizable RHB population like M3, and its blue tail is short like that of NGC288. We have measured 10 of its B′ members, but only a single BT representative to date.

Table 4.1 summarizes the characteristics of the program clusters. Data on metallicity, reddening, and distance modulus are taken from the compilation of Ferraro *et al.* (1999b).

Table 4.1: Parameters for program clusters.

cluster	[Fe/H]	$E(B-V)$	$(m-M)_0$	$V_{\rm HB}$	N(B′)	N(BT)
M3	−1.34	0.01	15.03	15.68	6	0
M13	−1.39	0.02	14.43	15.10	5	8
M15	−2.12	0.09	15.15	15.90	10	8
M68	−1.99	0.04	15.14	15.75	10	1
M92	−2.16	0.02	14.78	15.30	20	2
NGC288	−1.07	0.03	14.73	15.50	0	4

4.3 CMDs and finding charts

We show CMDs of the BHB region of each of these six clusters in Figure 4.1, with our target stars marked.

Finding charts for the target sample are available from a variety of sources, summarized in Table 4.2, and Figures 4.2 and 4.3 label the target stars in M68 and the core of M13.

Table 4.2: Finding charts for program stars.

cluster	stars	reference
M3	B	Sandage (1953), Figure 6
M13	IV-83	Arp (1955), Figure 2
	J11	Arp & Johnson (1955), Plate 13
	SA	Savedoff (1956), Figure 2
	WF	Figure 4.3 (this paper)
M15	B	Buonanno *et al.* (1983a), Figures 1–4
M68	W	Walker (1994), Plate 18 (unlabeled) also Figure 4.2 (this paper)
M92	IV, VI, X, XII	Sandage & Walker (1966), Figure 1
	B	Buonanno *et al.* (1983b), Figures 1–4
NGC288	B	Buonanno *et al.* (1984), Figures 1–4

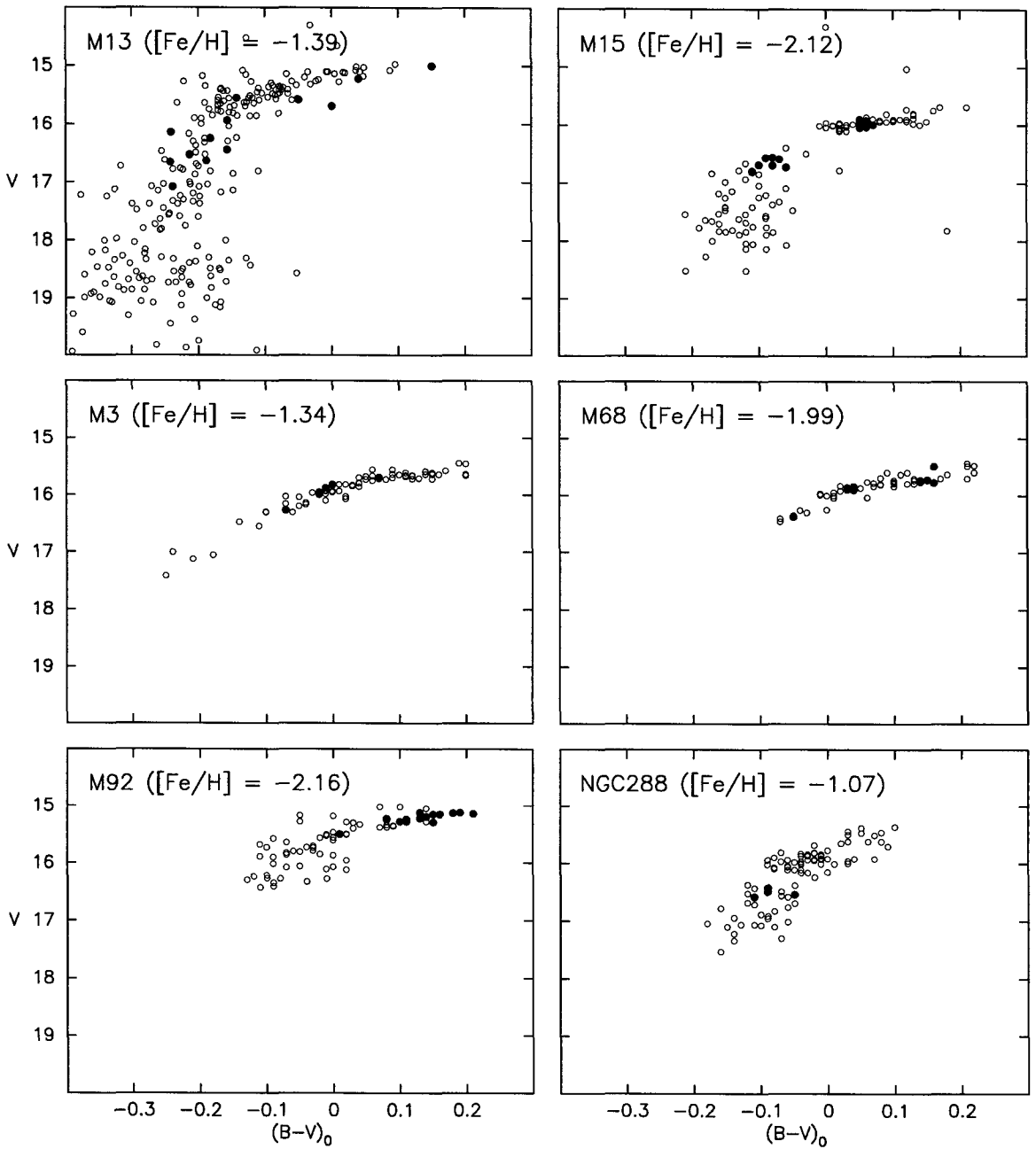

Figure 4.1: CMDs of the HBs of our six globular clusters. Solid symbols denote the target stars for this study.

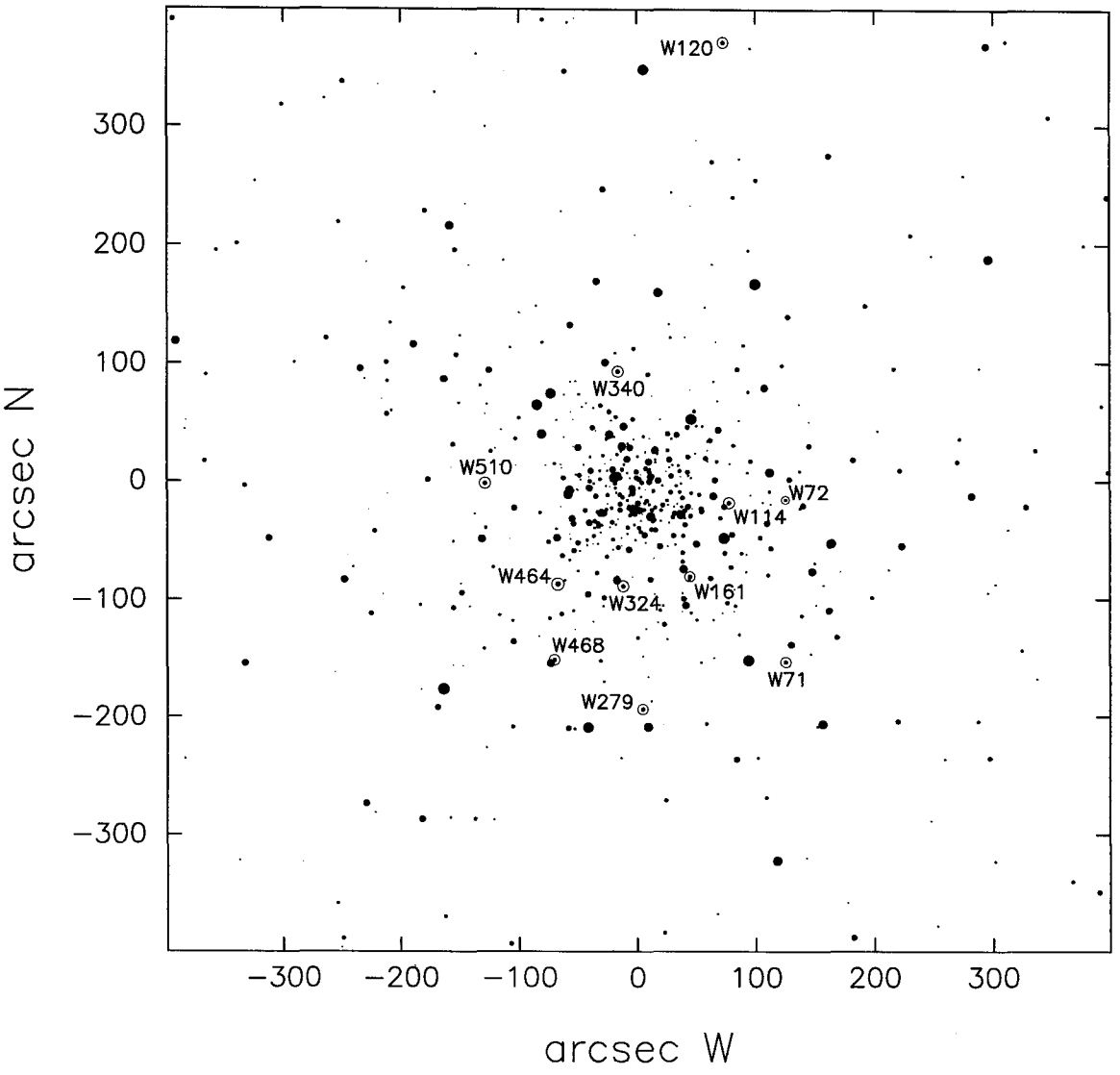

Figure 4.2: Finding chart for M68 targets. North is up, east is left.

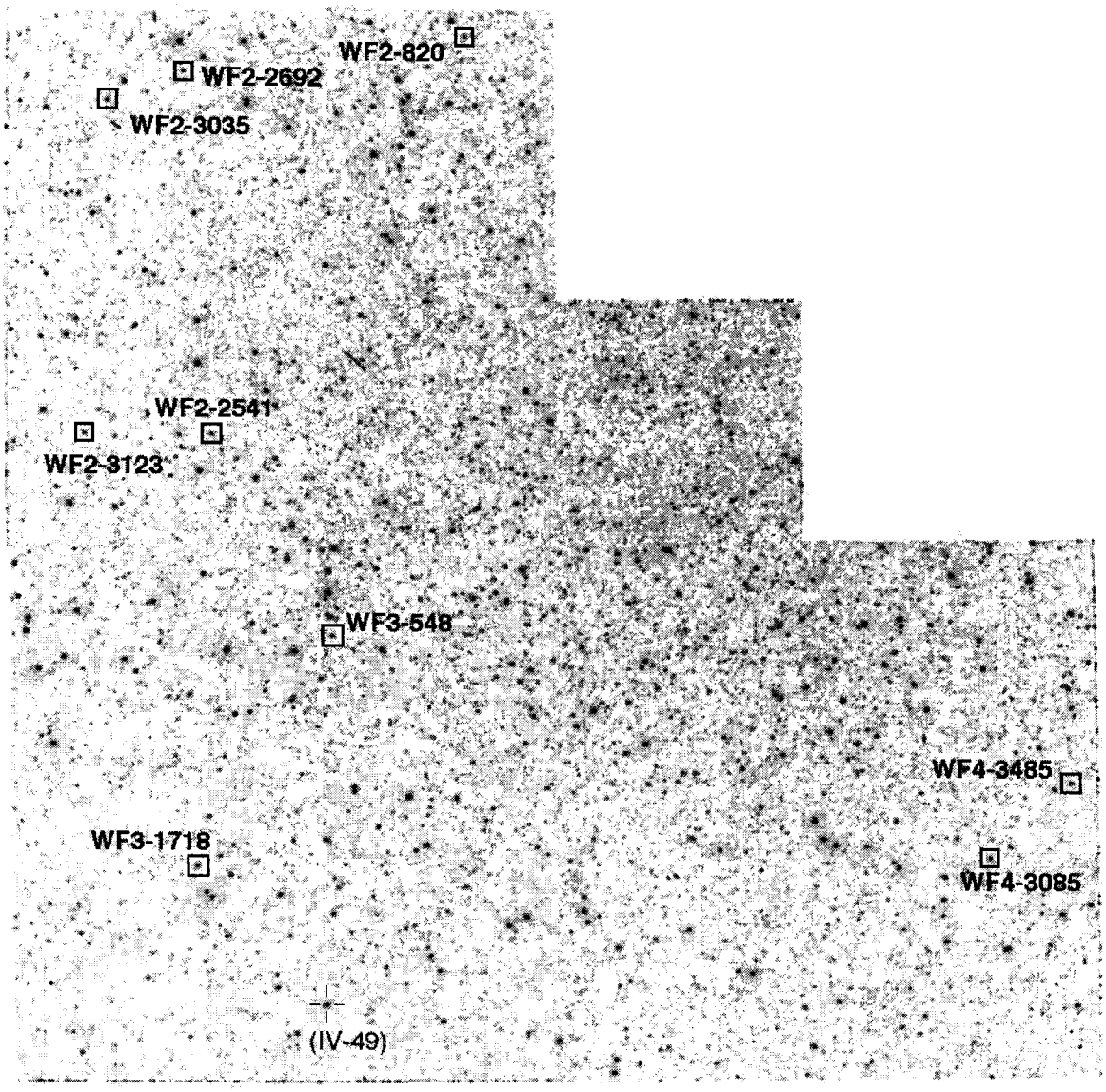

Figure 4.3: Finding chart for M13/WF targets. North is up, east is left. Star IV-49 (from Arp (1955)) is marked as a reference point.

Chapter 5 Observations, reduction, and analysis

In the following section, we review the spectroscopic observations of the selected BHB stars, and the reduction and analysis procedures for both the spectroscopy and the photometry.

5.1 HIRES spectroscopy

5.1.1 Instrument configuration and observing runs

All of the spectroscopic data for this project were acquired with the HIRES spectrograph (Vogt *et al.*, 1994) on the Keck I telescope. HIRES is a cross-dispersed echelle instrument, offering high spectral resolution ($R = \lambda/\Delta\lambda = 30000 - 60000$) over a large wavelength range. Most of the BHB observations used the C1 slit decker, which measures 0.86 arcsec in the dispersion direction, yielding a 3-pixel spectral resolution element with $R = 45000$, equivalent to a velocity resolution of $v = 6.7\,\mathrm{km\,s^{-1}}$. (A few of the early observing runs utilized the wider C5 decker, with $R = 34000, v = 8.9\,\mathrm{km\,s^{-1}}$.) Two different cross-disperser gratings ('RED' and 'UV') are available for HIRES, depending on the slit length and order spacing for the spectral region being observed. Since many of the BHB observations were piggybacked on other observing programs, different cross-disperser and echelle grating settings were used from run to run, and spectral coverage varies slightly as a result. Table 5.1 provides an overview of the seven different grating configurations used in this program.

In order to get the high signal-to-noise (S/N) ratios necessary for the abundance and

Table 5.1: HIRES grating configurations.

setting code	cross-disperser grating mode	cross-disperser angle (deg)	echelle angle (deg)	echelle orders	total λ coverage (Å)	continuous λ coverage (Å)
A	RED	−0.202	−0.400	54–82	4304–6631	4304–5190
B	RED	−0.492	−0.121	57–91	3885–6292	3885–5123
C	RED	−0.429	−0.037	56–87	4066–6408	4066–5126
D	UV	1.352	0.000	65–88	4020–5520	4020–5126
E	UV	1.354	0.172	66–90	3936–5442	3936–5059
F	UV	1.194	0.000	67–91	3888–5356	3888–5126
G	RED	−0.816	0.000	61–91	3888–5884	3888–5127

rotation measurements, we integrated on each star for a total of 1 to 1.5 hours. We generally limited individual exposure times to 1200 or 1500 seconds, to minimize cosmic ray accumulation, and then coadded three to four frames per star. The chip readout was binned by two pixels in the spatial direction, to decrease readout time and read noise. In Table 5.2, we summarize the observations on each target star, including the mean S/N, as estimated from the RMS dispersion of the continuum regions of the final reduced spectrum. At the beginning and end of each night, we also took multiple bias frames and flatfield and arc lamp exposures, for the echelle reduction procedure described below.

5.1.2 Echelle reduction pathway

We used a suite of routines (McCarthy, 1990) developed for the FIGARO data analysis package (Shortridge, 1993) to reduce the HIRES echellograms to arrays of one-dimensional spectra. These routines were designed as general tools for echelle reduction, applicable to a wide variety of different instruments, so we developed a series of scripts to customize the parameter settings for the HIRES format. The reduction pathway proceeds as follows:

Bias subtraction: An overscan region of several hundred pixels is included with each CCD frame read from the HIRES chip. The final 50 columns from this region of the image are collapsed horizontally and averaged to create a mean "erase column," which represents the row-dependent DC bias level inherent in the chip readout electronics. This one-dimensional erase column is then subtracted from each column on the image. This procedure is repeated for every frame in the data set.

The HIRES chip also suffers from a column-dependent DC level, which appears as a hump about 30 DN (data numbers) high, along the left edge of the chip. For each night of observations, we collect ten bias frames — zero-duration exposures with all instrument hatches closed and light sources off — and average them together, after removing cosmic ray hits from each frame. This average bias frame is subtracted from each data frame (flats, arcs, and stars), eliminating the hump.

Flatfields: To achieve the highest possible S/N, we must evaluate and compensate for several different sources of gain variation within the spectrograph. The echelle grating introduces a "blaze function," such that the continuum intensity of each order is at a maximum at the center of each order, but drops off by a factor of ~ 2 at each edge of

Table 5.2: HIRES observations of BHB stars.

civil dates cluster/star	exposures	slit & grating	mean S/N	*civil dates* cluster/star	exposures	slit & grating	mean S/N
1994 Oct 04–06				*1998 Apr 20–22 continued*			
M92/XII-9	3 × 1200 s	C5, A	62	M3/B831	3 × 1500 s	C1, D	40
M92/XII-1	3 × 1200 s	C5, A	72	M68/W114	3 × 1200 s	C1, D	32
M92/X-22	3 × 1200 s	C5, A	65	M68/W72	3 × 1800 s	C1, D	31
M92/IV-27	3 × 1200 s	C5, A	66	M68/W468	3 × 1500 s	C1, D	36
M92/IV-17	3 × 1500 s	C5, A	42	M92/B516	3 × 1200 s	C1, D	51
				M92/B176	3 × 1800 s	C1, D	56
1997 Jan 07							
M3/B518	3 × 1200 s	C5, B	38	*1998 Jun 27*			
M3/B1241	2 × 1200 s	C5, B	29	M68/W161	4 × 1200 s	C1, E	34
M3/B445	3 × 1200 s	C5, B	31	M13/IV-83	3 × 1200 s	C1, E	58
				M13/SA113	3 × 1200 s	C1, E	41
1997 Aug 01-03				M13/SA404	3 × 1200 s	C1, E	40
M92/B455	4 × 1200 s	C1, C	61	M13/J11	3 × 1200 s	C1, E	51
M92/B251	3 × 1500 s	C1, C	64	M15/B78	3 × 1600 s	C1, E	42
M92/B219	3 × 1500 s	C1, C	62	M15/B124	3 × 1500 s	C1, E	37
M15/B331	3 × 1500 s	C1, C	41				
M15/B177	3 × 1500 s	C1, C	39	*1998 Aug 20–21*			
M15/B153	4 × 1500 s	C1, C	41	M13/WF2-3035	3 × 1200 s	C1, B	65
M92/B103	3 × 1500 s	C1, C	56	M13/WF2-2541	3 × 1500 s	C1, B	44
M92/B148	3 × 1500 s	C1, C	59	M13/WF2-2692	3 × 1800 s	C1, B	34
M92/B233	3 × 1500 s	C1, C	58				
M15/B244	3 × 1500 s	C1, C	40	*1998 Aug 26–27*			
M15/B130	3 × 1500 s	C1, C	42	M13/WF4-3085	3 × 1200 s	C1, F	37
M92/B246	3 × 1500 s	C1, C	51	M13/WF2-820	3 × 1200 s	C1, F	34
M92/VI-10	4 × 1500 s	C1, C	66	M92/B527	3 × 1200 s	C1, F	59
M92/B29	2 × 1500 s	C1, C	42	M15/B334	4 × 1500 s	C1, F	39
M15/B558	3 × 1500 s	C1, C	27	M15/B348	4 × 1500 s	C1, F	35
M15/B424	3 × 1500 s	C1, C	44	M13/WF3-548	3 × 1200 s	C1, F	32
M15/B218	3 × 1500 s	C1, C	38	M13/WF4-3485	3 × 1200 s	C1, F	34
				M15/B279	4 × 1400 s	C1, F	34
1998 Apr 20–22				M15/B84	4 × 1400 s	C1, F	34
M68/W464	3 × 1200 s	C1, D	35	M15/B267	4 × 1400 s	C1, F	26
M68/W324	3 × 1200 s	C1, D	33				
M68/W510	3 × 1200 s	C1, D	33	*1999 Mar 09*			
M68/W340	3 × 1200 s	C1, D	28	M13/WF3-1718	3 × 1200 s	C1, G	48
M92/W30	3 × 1200 s	C1, D	45	M13/WF2-3123	3 × 1200 s	C1, G	35
M92/W145	3 × 1200 s	C1, D	67				
M92/W202	3 × 1200 s	C1, D	50	*1999 Aug 14–17*			
M3/B125	3 × 1500 s	C1, D	37	M15/B374	3 × 1200 s	C1, B	21
M3/B244	3 × 1500 s	C1, D	37	NGC288/B16	3 × 1200 s	C1, B	21
M68/W120	3 × 1200 s	C1, D	31	NGC288/B22	3 × 1200 s	C1, B	17
M68/W279	3 × 1200 s	C1, D	33	M15/B203	3 × 1200 s	C1, B	28
M68/W71	3 × 1200 s	C1, D	33	NGC288/B302	3 × 1200 s	C1, B	26
M92/B466	3 × 1200 s	C1, D	50	M15/B315	3 × 1200 s	C1, B	24
M92/B365	3 × 1800 s	C1, D	52	NGC288/B186	3 × 1200 s	C1, B	31

the chip. In addition, each pixel on the CCD has a slightly different wavelength-dependent quantum efficiency, and additional noise is introduced to the spectrum if this pixel-to-pixel variation is not accounted for in a wavelength-specific manner. To compensate for both of these effects, we take spectra of a white light source which is built into the spectrograph. The resulting flatfield image creates a map of the spectrograph efficiency as a function of chip position, both on large scales (the blaze function) and small scales (pixel-to-pixel).

Unfortunately, the incandescent lamp is not spectrally flat, as it is essentially a blackbody with $T_{\rm eff} \simeq 3000\,{\rm K}$, and the bluer orders in the spectra are much fainter than the red orders. To ensure adequate signal across the entire spectral range, we employ a series of red-blocking filters, so that we can take longer exposures to illuminate the blue orders without saturating the red orders. We take a sequence of three different filter settings, with four to eight exposures per setting, and then weight each order so as to maximize the total S/N in the final co-added flatfield image. As an additional refinement, the ECHXPROFIT routine traces each order of the spectrum image, constructing a median slit profile, and then normalizing each order to produce an accurate gain map for all pixels on the chip, even those near the edges of the slit which are poorly illuminated by the flatfield lamp.

We should note that the HIRES chip has one striking peculiarity — a large dark "splotch" at chip center, approximately 40 pixels wide and 20 (binned) pixels high. The grating configuration is chosen such that an uninteresting region of a single spectral order lies on this region, and the scientific impact is minimal, but this large, sudden dip in the flatfield illumination becomes problematic during the median profile normalization, as it greatly confuses the tracing and medianing algorithm. To get around this problem, we remove the splotch region entirely from the flatfield frames, and substitute a similar region of good spectrum from an adjacent order.

Once the final composite flatfield image has been created, all of the calibration arc and target star frames are divided by it, so that all the gain variations cancel out. As verification, we also divide individual flatfield images by the master image, and find that the pixel and blaze functions all but disappear, leaving only the overall spectral shape of the lamp plus the filter.

Cosmic ray removal: The automated FIGARO routine for cosmic ray (CR) identification and removal, BCLEAN, works well for uniformly-illuminated images like flatfields

and bias frames, but is less well-suited for actual stellar data. Regions of stellar continuum between strong absorption features can look like cosmic ray hits to the identification algorithm, and the CR removal procedure (interpolating across a 5×5 pixel box centered on the peak pixel) can obscure or destroy useful data. The spectra of the target stars, therefore, are cleaned by hand. Each image is examined at high magnification, and individual pixels (or small blocks of pixels) which appear to be spurious are erased and interpolated across. Although this is a very labor-intensive approach, the high quality of the final product validates the time spent.

Order tracing and extraction: Another FIGARO procedure, ECHDIST, traces each spectral order on an echellogram image, fitting a high-order polynomial to the (x, y) coordinates of the order on the chip. We trace orders on each target exposure separately, instead of coadding multiple exposures, because the exact shape and position of each order depends on the telescope pointing and amount of atmospheric dispersion. Each order is then extracted into a one-dimensional spectrum, by summing pixels within a box centered on the order trace, for each column on the chip. The box width is adjusted depending on the width of the star's spatial profile, which is a function of seeing and telescope focus. The sky background and scattered light background are negligible, so no background subtraction is necessary.

For λ-calibration of the spectra, HIRES has an internal thorium-argon arc lamp, which provides many thousands of emission lines of known wavelengths. The arc spectra cannot be traced with ECHDIST, however, since there is no spatially narrow continuum source. Instead, we coadd all of the target star exposures from a given night, and trace the orders of this "average stellar position." The polynomial traces are copied on to the arc frames, and one-dimensional arc spectra are extracted in the same fashion as for the stellar frames. The arc lines for a handful of the orders must be identified manually and entered into the ECHARC4 utility, which then uses the grating equation to interpolate a wavelength solution for all orders. The mapping between pixel coordinate and λ is closely fit by a parabola, although a third-order polynomial provides a slightly better fit, with an RMS dispersion of less than 5 mÅ in nearly all cases. The final wavelength solution is applied to the extracted stellar spectra, which are rebinned into a common wavelength scale, such that $m\lambda =$ constant for each column of the chip.

Continuum normalization: The flatfielding procedure removes much of the blaze function of the spectrograph, but the stellar continuum is still not perfectly flat in each order. The ECHXCONT function fits a high-order polynomial to the continuum of each successive order, iteratively discarding absorption and emission lines (specified manually, or identified automatically as protruding more than several σ from the fit curve) until the continuum solution converges. Each order is divided by its continuum polynomial, normalizing it to unity.

Several interesting orders from one of our stars are shown in Figure 5.1 to illustrate the appearance of the final spectra.

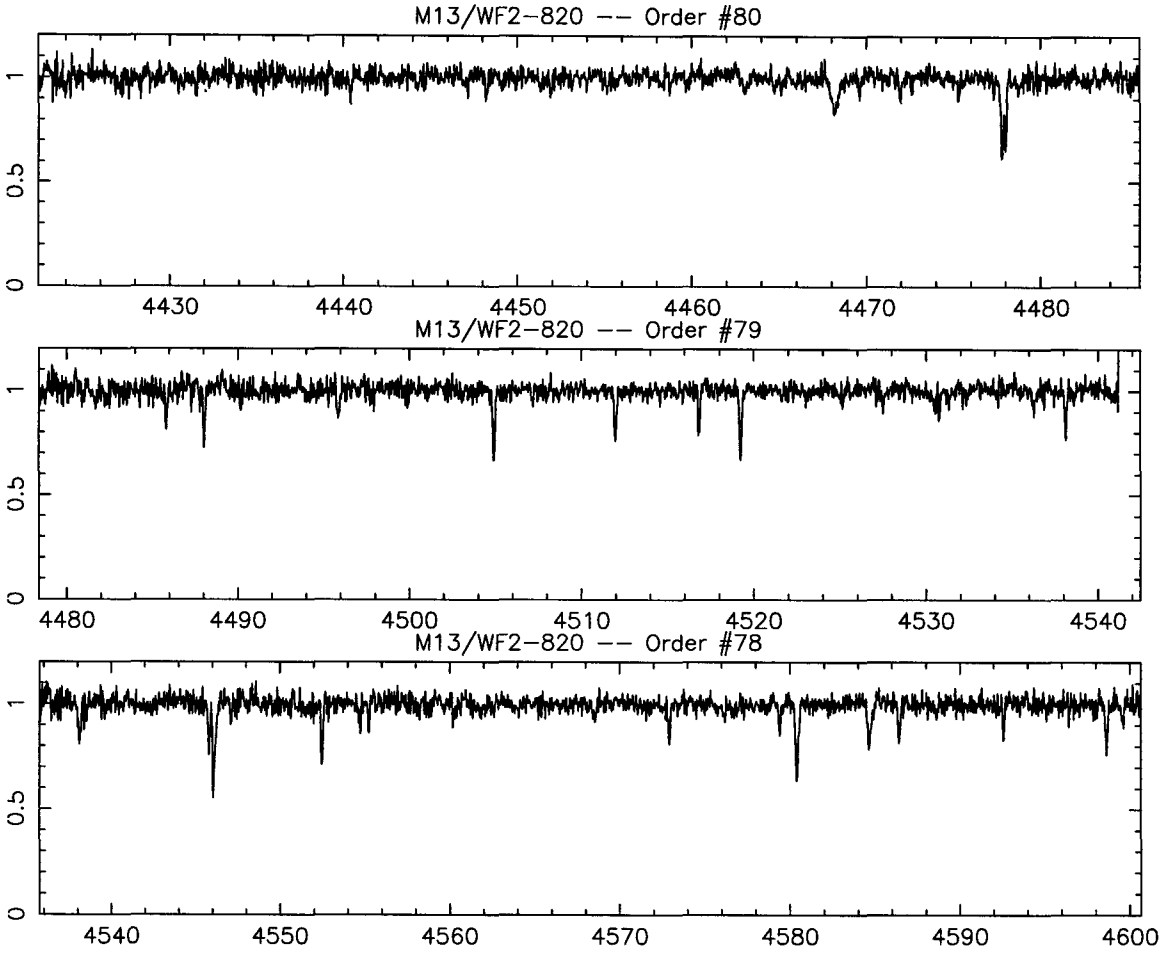

Figure 5.1: Selected orders from the spectrum of M13/WF2-820. The He I 4471 line (λ_{obs} = 4468 Å) and two components of the Mg II 4481 triplet (λ_{obs} = 4478 Å) are evident, as well as many Fe and Ti absorption lines.

5.2 Photometry

5.2.1 Broadband photometry from literature

Published cluster photometry was initially used for selecting BHB targets, and also plays a role in establishing the photospheric parameters $T_{\rm eff}$ and $\log g$ used for the abundance analysis. We drew photometric data from a variety of different sources, summarized in Table 5.3. The transformation from color and magnitude to temperature and gravity is detailed below.

5.2.2 Strömgren observations

In an effort to augment (and perhaps replace) the broadband photometry measurements from the literature, we undertook CCD imaging observations of our primary clusters, M13, M15, and M92, using Strömgren *uvbyβ* filters. The Strömgren system is particularly well-suited to studying stars, as the bandpasses were chosen to measure specific regions of the stellar spectrum, such as the Balmer jump, the Hβ core and wings, and the metal-line-rich zone around 4100 Å.

We used the Palomar 60-inch telescope and a 2048×2048 CCD to observe these clusters during four runs in summer 1997 and summer 1998. Several of these nights were photometric, but the seeing was not terribly good ($\sim$ 1.5 arcsec) for any of them. Even more problematic, however, was the challenge of deriving an accurate airmass correction for each of the bands. Although we observed standard stars over a range of $\sec z$, the slopes of the extinction curves varied by as much as 0.2 mag from night to night, and the number of standard star measurements in a single night were not enough to extrapolate to $\sec z = 0$ with an accuracy of better than ~ 0.1 mag. The final atmosphere-free Strömgren colors, therefore, have unacceptably large error bars, and do not constrain $T_{\rm eff}$ and $\log g$ to any useful degree.

5.3 Determining photospheric parameters

5.3.1 Photometric magnitudes and colors

The ATLAS9 atmosphere modeling codes (Kurucz, 1997), which we use for the spectral synthesis analysis (below), also provide synthesized photometric colors, which are calcu-

Table 5.3: Photometry for BHB stars.

star	V	$B-V$	$U-B$	$U-V$	$V-I$	ref.
M3/B125 (I-I-30)	15.82	0.01				1
M3/B244 (I-II-66)	15.96	−0.01				1
M3/B445 (I-I-56)	16.27	−0.06				1
M3/B518 (I-III-22)	15.70	0.08				1
M3/B831 (I-IV-78)	15.88	0.00				1
M3/B1241 (I-IV-18)	15.99	−0.01				1
M13/IV-83	15.22	0.06				2
M13/J11	15.00	0.17				2
M13/SA113	15.69		−0.14			3
M13/SA404	15.58		−0.13			3
M13/WF2-820	16.128			−0.577		4
M13/WF2-2541	16.643			−0.727		4
M13/WF2-2692	16.518			−0.193		4
M13/WF2-3035	15.532			0.135		4
M13/WF2-3123	17.071			−0.838		4
M13/WF3-548	16.623			−0.719		4
M13/WF3-1718	15.922			−0.346		4
M13/WF4-3085	16.231			−0.629		4
M13/WF4-3485	16.428			−0.521		4
M15/B78	15.99	0.15				5
M15/B84	16.56	0.00				5
M15/B124	15.91	0.15				5
M15/B130	15.96	0.15				5
M15/B153	15.95	0.14				5
M15/B177	16.03	0.15				5
M15/B203	16.68	−0.01				5
M15/B218	15.99	0.16				5
M15/B244	15.96	0.14				5
M15/B267	16.72	0.03				5
M15/B279	16.56	0.01				5
M15/B315	16.80, 16.889	−0.02, −0.013				5, 6
M15/B331	16.04	0.14				5
M15/B334	16.58, 16.642	0.02, 0.041				5, 6
M15/B348	16.69, 16.673	0.01, 0.052				5, 6
M15/B374	16.79	−0.02				5
M15/B424	15.89, 15.906	0.14, 0.144				5, 6
M15/B558	15.93	0.14				5
M68/W71	15.885	0.072			0.128	7
M68/W72	16.372	−0.013			0.021	7
M68/W114	15.734	0.177			0.261	7
M68/W120	15.861	0.075			0.101	7
M68/W161	15.896	0.082			0.144	7
M68/W279	15.862	0.072			0.124	7
M68/W324	15.772	0.204			0.287	7
M68/W340	15.748	0.177				7
M68/W464	15.491	0.205			0.351	7
M68/W468	15.839	0.082			0.122	7
M68/W510	15.718	0.185			0.335	7
M92/B29	15.24	0.13				5
M92/B30	15.17	0.20				5
M92/B103	15.24	0.20				5
M92/B145	14.72	0.18				5
M92/B148	15.33	0.11				5
M92/B176	15.87	−0.06				5
M92/B202	15.10	0.21				5
M92/B219	15.15	0.18				5
M92/B233	15.36	0.08				5
M92/B246	15.20	0.19				5
M92/B251	15.22	0.10				5
M92/B365	15.68	−0.06				5
M92/B455	15.24	0.08				5
M92/B466	15.30	0.09				5
M92/B516	15.40	0.09				5
M92/B527	15.33	0.00				5
M92/IV-17	15.50	0.02				5
M92/IV-27	15.19	0.17				5
M92/VI-10	15.24	0.13				5
M92/X-22	15.16	0.17				5
M92/XII-1	15.11	0.19				5
M92/XII-9	15.09	0.15				5
NGC288/B16	16.54	−0.02				8
NGC288/B22	16.49	−0.06				8
NGC288/B186	16.42	−0.06				8
NGC288/B302	16.58	−0.08				8

references: [1] Buonanno *et al.* (1994), [2] Peterson *et al.* (1995), [3] Sandage (1969), [4] Zoccali (1998), [5] Buonanno *et al.* (1985), [6] Durrell & Harris (1993), [7] Walker (1994), [8] Buonanno *et al.* (1994)

lated from the spectral energy distribution (SED) emerging from each model atmosphere. By comparing the observed colors of each star ($B-V$, $U-V$, $U-B$, or $V-I$, appropriately corrected for the reddening for each cluster) to the predicted color for a variety of atmospheres of different $T_{\rm eff}$ and $\log g$, we can constrain these parameters. These photometric colors are most sensitive to temperature, with only a modest dependence on gravity.

In order to pin down the surface gravity for a given star, we must assume a distance modulus and a stellar mass M_*, and then use the resulting absolute magnitude M_V to calculate the stellar radius. More specifically, we employ the AB_ν flux introduced by Oke & Gunn (1983), and relate $\log g$, stellar mass M_*, distance modulus $(M-m)_V$, and photospheric Eddington flux H_ν at 5480 Å. Since $AB_\nu(5480\,\text{Å}) = V$ magnitude, we can derive

$$\log g = 7.68 + \log(M_*/M_\odot) + \log H_\nu(5480\,\text{Å}) + 0.4M_V\ .$$

We assume $M_* = 0.6M_\odot$ as a representative BHB star mass, and draw the $H_\nu(5460\,\text{Å})$ values from the model atmospheres. Distance moduli taken from the compilation of Ferraro *et al.* (1999b), as cited in Table 4.1 above, are combined with de-extincted V magnitudes to derive the absolute magnitude for each star.

5.3.2 Spectral line indicators

In addition to the photometric inputs, there exist two spectral absorption-line indicators which can also help to determine the appropriate photospheric parameters for each star. One is the ionization balance approach, which assumes that the element abundances calculated from two different ionization stages of the same element — Fe I and Fe II, for instance — should be equal. If these values are not equal, then this suggests that the model atmosphere and spectral synthesis program are assuming an incorrect temperature and gravity, so that the predicted populations of each ionization stage are erroneous. If the abundances $\log\epsilon$(Fe I) $>$ $\log\epsilon$(Fe II), then either the model temperature is too high, or the model gravity is too low; if $\log\epsilon$(Fe I) $<$ $\log\epsilon$(Fe II), then the temperature is too low or the gravity is too high. One potential complication with this technique arises because the modeling assumes local thermodynamic equilibrium (LTE) — that the ionization energy originates solely from the thermal content of the gas in the atmosphere. In the real stellar atmosphere, the radiation field can also play a role, photoionizing an additional fraction of the atoms

into a higher stage. Simulations of these non-LTE mechanisms have been performed by Gigas (1986) and Thevenin *et al.* (1999), which show that the [Fe I/H] abundance derived under LTE can be as much as 0.3 dex higher than the true abundance, while the [Fe II/H] abundance deviates by only 0.02 dex or less. Indeed, in our hotter BT stars, we do ultimately find that $\log(\epsilon(\text{Fe I})/\epsilon(\text{Fe II})) \simeq 0.2 - 0.3$ dex, but for the cooler B′ population, the $T_{\rm eff}$ values based on photometry agree more closely with a non-LTE offset $\Delta \log \epsilon = 0$, so we adopt $\log \epsilon(\text{Fe I}) = \log \epsilon(\text{Fe II})$ as the appropriate diagnostic for this regime.

An alternative spectral measurement is based on the excitation potentials χ of different transitions of the same spectral species. If the temperature is correct, then the abundances derived from several different lines should show no trend as a function of χ, *i.e.*, $d \log \epsilon / d\chi = 0$. If the temperature is too high, then the models will overpopulate the levels with large χ, and the $\log \epsilon$ derived from these levels will be too low, such that $d \log \epsilon / d\chi < 0$. If the temperature is too low, then the converse will be true.

The ionization-balance and excitation-balance measurements both require an appropriate value for the microturbulent velocity ξ, which regulates the line formation mechanism for a given transition, and thus can influence the derived $\log \epsilon$. The value of ξ for each star is determined in a similar manner as the $d \log \epsilon / d\chi$ technique: if the wrong microturbulence parameter is used for the abundance analysis, then the abundances derived for stronger lines will be systematically offset from those from weaker lines. If we plot $\log \epsilon$ for each line of a given species as a function of equivalent width W_λ, and find a strong linear trend, *i.e.*, $d \log \epsilon / dW_\lambda \neq 0$, then this suggests that the adopted ξ is in error. Similarly, it is important that the model atmospheres for the spectroscopic and photometric analyses be computed with an appropriate metallicity, since the atmospheric structure is strongly dependent upon the opacity. We perform an initial abundance on lines of Fe IIin order to derive [Fe/H] for each star. In practice, we iterate between a $(T_{\rm eff}, \log g)$ solution (as described in the next section), and recalculations of ξ and [Fe/H], until all the parameters stabilize.

5.3.3 Convergence of $T_{\rm eff}/\log g$ loci

All of these various diagnostics — photometric color, absolute magnitude, ionization offset, and χ-slope — can be used to delineate different regions or loci in the $(T_{\rm eff}, \log g)$ plane, which then overlap at the most likely solution point. The algorithm we use to derive this solution is as follows. Over a range of values of $T_{\rm eff}$ and $\log g$ (assuming fixed metallicity and

microturbulence), we calculate the expected value of a given parameter — synthetic colors or magnitudes from model atmospheres, or ionization offsets or χ-slopes from abundance analysis of given species. By interpolating between these grid points, we define a surface $z(T, g)$, the predicted parameter value as a function of temperature and gravity. We also have a measured or expected value z_0 of that parameter, which can be envisioned as a flat plane, perpendicular to the z-axis. The locus of points (T, g) where the surface and the plane intersect, $z(T, g) = z_0$, represent possible solutions for the surface temperature and gravity of the star. Furthermore, we can incorporate a measurement error σ_z into the solution locus, by defining a "probability" function

$$P(T, g) = \exp\left(-\frac{(z(T, g) - z_0)^2}{2\sigma_z^2}\right)$$

which indicates how "close" a given $z(T, g)$ is to the measured value $z_0 \pm \sigma_z$. A $(T_{\rm eff}, \log g)$ point with a predicted parameter value close to the measured value will have a high "probability" of being a valid solution, whereas a point with $|z - z_0| \gg \sigma_z$ does not agree well with the measurement, and is therefore unlikely to be a correct solution. Note that the value P is not a probability or probability density in any formal sense, since $\int_{T,g} P \neq 1$, but it does serve as a measure of relative likelihood for each choice of $T_{\rm eff}$ and $\log g$. This procedure is illustrated in Figure 5.2, which shows the P functions for a given $(B - V)_0$ color and a given absolute magnitude M_V.

Each parameter, then, defines a different track through the $(T_{\rm eff}, \log g)$ plane. For the photometric colors, the synthetic colors from ATLAS9 model atmospheres of appropriate metallicity are compared to the measured, dereddened colors as described above. The resulting P surfaces most strongly constrain $T_{\rm eff}$, although they are weakly $\log g$-dependent as well. In a similar vein, the models' absolute magnitudes computed via the AB_ν flux method are compared to the V magnitude of each star, de-extincted and scaled to the appropriate distance modulus, to yield P surfaces which determine $\log g$. The error in absolute magnitude is dominated by the uncertainty in the distance modulus, which is estimated by Ferraro *et al.* (1999b) to be 0.20 dex, so we use this value as σ_z for these calculations. For the ionization balance technique, we calculate abundances for Fe I and Fe II over a grid of $T_{\rm eff}$ and $\log g$ values, and calculate the offset $\Delta_{\rm Fe} = \log \epsilon(\text{Fe I}) - \log \epsilon(\text{Fe II})$ for each grid point. We set $z_0 = 0.0$ to compute the locus for ionization balance, as we

do not expect non-LTE deviations to be significant for the cooler stars, and use a σ_z equal to the quadrature sum of the RMS errors in the means of the Fe I and Fe II abundance calculations. Lastly, for the excitation-balance, we again raster-scan a grid of $(T_{\rm eff}, \log g)$, calculating abundances for species like Fe II, Ti II, and P II, which are largely immune to non-LTE effects and which provide a large number of lines of different χ. For each such species, we plot $\log \epsilon$ for each line as a function of its χ, and perform a linear fit to the points. The slope of the line gives $d \log \epsilon / d\chi = z(T_{\rm eff}, \log g)$, and the error in the slope computed from the linear regression is used as σ_z when the P surface is calculated.

In order to arrive at a common solution for all the different diagnostics, we multiply their probability surfaces together, as illustrated in the last panel of Figure 5.2. The locations in the plane where they intersect will remain at high probability, and therefore indicate possible solutions that satisfy all the constraints. Ideally, all the tracks would converge on a single point, surrounded by a small error oval. In practice, though, this is not the case, because each diagnostic is valid only under certain conditions. The ionization balance approach, for instance, only works at lower $T_{\rm eff}$ (below $\sim 10000\,{\rm K}$), as there are few Fe I lines at higher temperatures. As another example, $U-V$ color is an excellent temperature diagnostic in general, but it overestimates $T_{\rm eff}$ for hotter stars with strongly enhanced metal abundances, for reasons which will be discussed in a later section. Therefore, we only use a subset of the diagnostics on any given star, following these general rules:

- For stars with $T_{\rm eff} < 10000\,{\rm K}$, we use $B-V$ colors primarily, with $U-V$, $U-B$, and $V-I$ when available, and ionization balance when there are enough lines of both Fe I and Fe II to derive a reliable $\log \epsilon$ for each.

- For metal-enhanced stars with $T_{\rm eff} > 10000\,{\rm K}$, we use excitation balance ($d \log \epsilon / d\chi = 0$) from multiple lines of Fe II, sometimes supplemented by Ti II or P II.

- For hot stars without metal enhancements, and the hottest of the M13 BT stars, there are too few iron lines for either ionization or excitation balance, so we resort to photometric colors, employing a $\Delta T_{\rm eff}$ offset derived from other stars in the same cluster with both photometric and spectroscopic temperatures.

Using these rules, we construct a total P-function for each star, and then calculate the

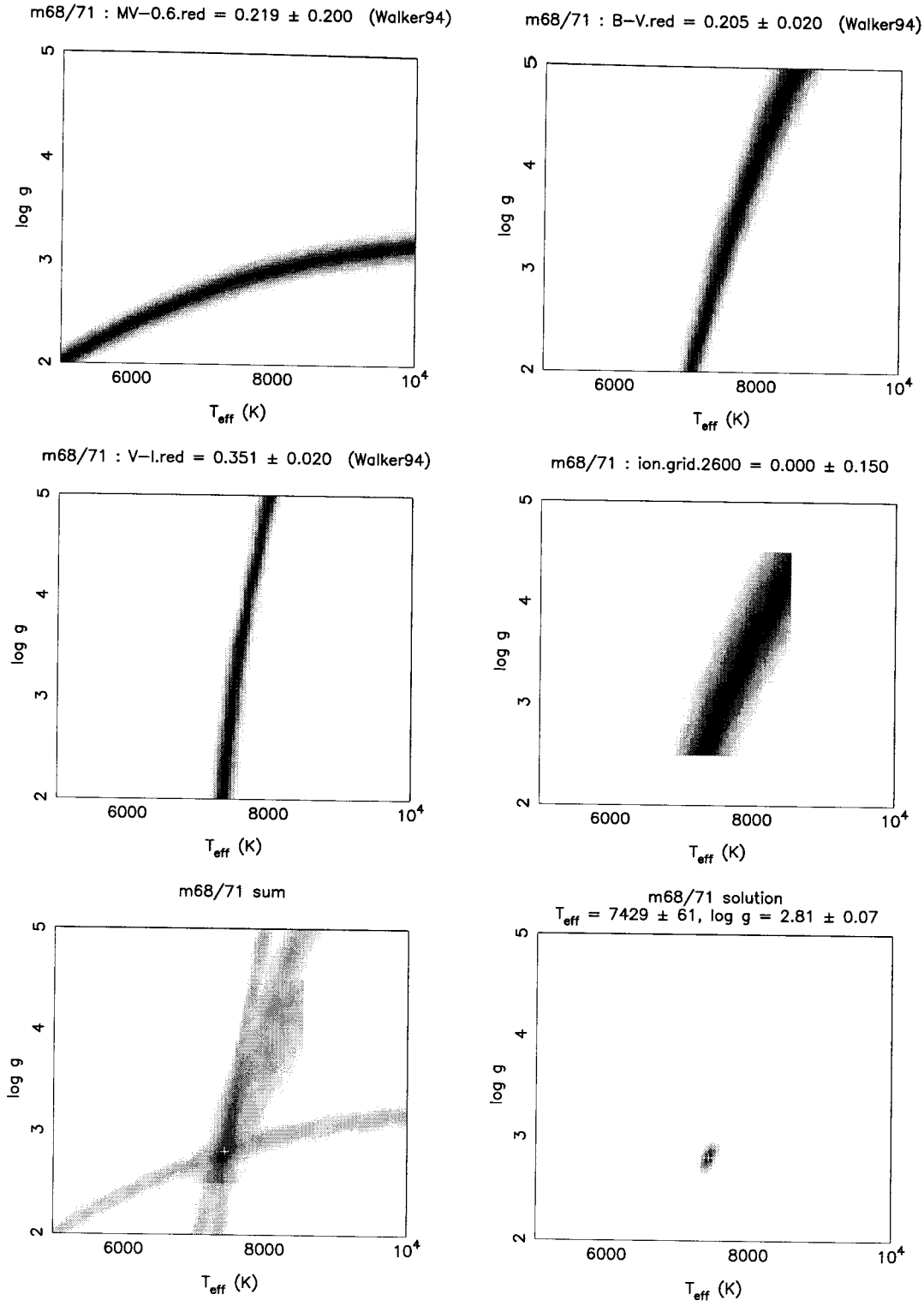

Figure 5.2: Plotted as a greyscale image, with darker regions corresponding to higher probability, the P-functions for each parameter define different swaths through the $(T_{\rm eff}, \log g)$ plane. Diagnostics for this star include M_V, $B-V$, $V-I$, and Fe I vs. Fe II. The sum of the four functions (bottom left) shows where all constraints intersect, and their product (bottom right) provides an error oval for a solution.

mean and dispersion for T and g like so:

$$\begin{aligned}
\text{normalizing factor} \quad \alpha &= \int_{T,g} P(T,g)\, dT \\
\mu_T &= \alpha^{-1} \int_{T,g} T\, P(T,g)\, dT\, dg \\
\mu_g &= \alpha^{-1} \int_{T,g} g\, P(T,g)\, dT\, dg \\
\sigma_T &= \alpha^{-1} \int_{T,g} (T-\mu_T)^2\, P(T,g)\, dT\, dg \\
\sigma_g &= \alpha^{-1} \int_{T,g} (g-\mu_g)^2\, P(T,g)\, dT\, dg
\end{aligned}$$

In other words, we calculate the centroid and width of the error oval along both the $T_{\rm eff}$ and the $\log g$ axes. Table 5.4 lists the diagnostics used to determine $(T_{\rm eff}, \log g)$, as well as microturbulence ξ, for each of the program stars, and the resulting parameter values.

We should note that the microturbulence values are not zero for all the hot stars, as was assumed by Moehler *et al.* (1999b). These stars surely have stable radiative atmospheres (as discussed later), so large-scale convection and macroturbulence may be absent, but microturbulence is still evident in many stars. We do, however, find lower average ξ velocities than the stars with $T_{\rm eff} < 8000$ K, which are thought to have fully convective envelopes.

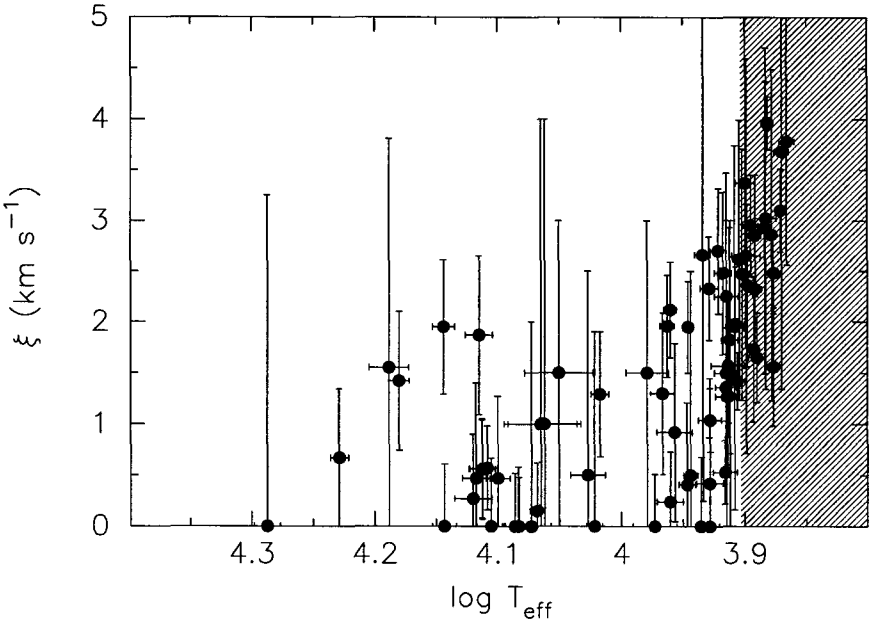

Figure 5.3: The microturbulent velocity ξ for the sample, as a function of $T_{\rm eff}$. The models of Sweigart (2000) predict fully convective atmospheres for stars in the hatched region. The measured ξ is higher for these stars, but ξ is still nonzero for the hotter radiative atmospheres.

Table 5.4: Derived photospheric parameters for target stars.

cluster/star	diagnostics	$T_{\rm eff}$ (K)	$\log g$ (cgs)	ξ diagnostics	ξ (km s^{-1})
M3/B518	M_V, B–V, $\Delta\epsilon$(Fe I–II)	8341 ± 123	3.19 ± 0.08	Ti II, Fe I & II	2.7 ± 0.6
M3/B125	M_V, B–V, $\Delta\epsilon$(Fe I–II)	9129 ± 106	3.35 ± 0.07	Fe II	2.1 ± 0.5
M3/B831	M_V, B–V, $\Delta\epsilon$(Fe I–II)	9178 ± 119	3.38 ± 0.08	Fe II	2.0 ± 0.5
M3/B1241	M_V, B–V, $\Delta\epsilon$(Fe I–II)	9258 ± 205	3.44 ± 0.08	Fe II	1.3 ± 0.8
M3/B244	M_V, B–V	9527 ± 382	3.45 ± 0.07		1.5 ± 1.5
M3/B445	M_V, B–V	11230 ± 740	3.71 ± 0.09		1.5 ± 1.5
M13/J11	M_V, B–V, $\Delta\epsilon$(Fe I–II)	7616 ± 82	2.98 ± 0.08	Ti II, Fe I & II	4.0 ± 0.3
M13/IV-83	M_V, B–V, $\Delta\epsilon$(Fe I–II)	8487 ± 146	3.24 ± 0.08	Ti II, Fe I & II	2.3 ± 0.5
M13/WF2-3035	M_V, U–V, $\Delta\epsilon$(Fe I–II)	8829 ± 99	3.39 ± 0.07	Fe II	2.0 ± 0.5
M13/SA404	M_V, U–B	10398 ± 173	3.59 ± 0.09	Fe II	1.3 ± 0.6
M13/SA113	M_V, U–B	10512 ± 306	3.64 ± 0.07	Fe II	0.0 ± 1.9
M13/WF3-1718	M_V, χ(Fe II)	11699 ± 161	3.82 ± 0.07	Ti II, Mn II, Fe II	0.2 ± 0.5
M13/WF4-3485	M_V, χ(Fe II)	12752 ± 344	4.09 ± 0.07	Fe II	0.0 ± 0.7
M13/WF2-820	M_V, χ(Fe II)	13036 ± 335	3.99 ± 0.07	Fe II	1.9 ± 0.8
M13/WF4-3085	M_V, χ(Fe II)	13912 ± 315	4.08 ± 0.07	Fe II	0.0 ± 0.6
M13/WF2-2541	M_V, χ(Fe II)	15150 ± 295	4.34 ± 0.07	Fe II	1.4 ± 0.7
M13/WF2-2692	M_V, χ(Fe II)	15434 ± 585	4.30 ± 0.07	Fe II	1.6 ± 2.3
M13/WF3-548	M_V, U–V offset	16129 ± 287	4.35 ± 0.07	Fe II	0.7 ± 0.7
M13/WF2-3123	M_V, U–V offset	19109 ± 480	4.62 ± 0.07	Fe II	0.0 ± 3.3
M15/B177	M_V, B–V, $\Delta\epsilon$(Fe I–II)	7982 ± 106	3.00 ± 0.08	Ti II, Fe II	2.5 ± 1.2
M15/B78	M_V, B–V, $\Delta\epsilon$(Fe I–II)	8024 ± 99	2.99 ± 0.08	Fe II	2.6 ± 1.4
M15/B130	M_V, B–V, $\Delta\epsilon$(Fe I–II)	8051 ± 118	2.98 ± 0.08	Mg I, Fe II	1.4 ± 0.3
M15/B218	M_V, B–V, $\Delta\epsilon$(Fe I–II)	8087 ± 139	3.00 ± 0.08	Mg I	2.0 ± 0.6
M15/B424	M_V, B–V	8163 ± 125	2.98 ± 0.06	Fe II	1.5 ± 1.5
M15/B124	M_V, B–V, $\Delta\epsilon$(Fe I–II)	8182 ± 102	2.98 ± 0.08	Fe I & II	1.3 ± 0.3
M15/B153	M_V, B–V	8220 ± 183	3.01 ± 0.08		1.5 ± 1.5
M15/B244	M_V, B–V	8220 ± 184	3.01 ± 0.08	Fe II	2.3 ± 1.2
M15/B558	M_V, B–V, $\Delta\epsilon$(Fe I–II)	8225 ± 163	3.00 ± 0.08	Ti II, Fe II	1.4 ± 0.9
M15/B331	M_V, B–V	8241 ± 186	3.05 ± 0.08	Fe II	0.5 ± 0.3
M15/B334	M_V, B–V offset	11825 ± 446	3.64 ± 0.06		0.0 ± 2.0
M15/B348	M_V, B–V offset	11831 ± 445	3.66 ± 0.06		0.0 ± 2.0
M15/B279	M_V, χ(Fe II)	12102 ± 202	3.67 ± 0.07	Ti II, Fe I & II	0.0 ± 0.5
M15/B84	M_V, χ(Fe II)	12118 ± 370	3.67 ± 0.07	Fe II	0.0 ± 0.6
M15/B374	M_V, χ(Fe II)	12844 ± 261	3.80 ± 0.07	Fe II	0.6 ± 0.4
M15/B267	M_V, χ(Fe II)	12957 ± 309	3.74 ± 0.07	Ti II, Fe II	0.6 ± 0.5
M15/B315	M_V, χ(Fe II)	12965 ± 328	3.81 ± 0.07	Fe II	0.6 ± 0.5
M15/B203	M_V, χ(Fe II)	13186 ± 469	3.78 ± 0.07	Fe II	0.3 ± 0.6
M92/XII-1	M_V, B–V, $\Delta\epsilon$(Fe I–II)	7347 ± 103	2.83 ± 0.08	Ti II, Fe I & II	3.8 ± 1.2
M92/B246	M_V, B–V, $\Delta\epsilon$(Fe I–II)	7418 ± 101	2.86 ± 0.08	Fe I & II	3.7 ± 2.3
M92/X-22	M_V, B–V, $\Delta\epsilon$(Fe I–II)	7529 ± 85	2.88 ± 0.08	Fe I & II	1.6 ± 0.6
M92/IV-27	M_V, B–V, $\Delta\epsilon$(Fe I–II)	7531 ± 102	2.89 ± 0.08	Fe I & II	2.5 ± 0.4
M92/B103	M_V, $\Delta\epsilon$(Fe I–II)	7638 ± 155	2.94 ± 0.08	Ti II, Fe II	3.0 ± 1.7
M92/B29	M_V, B–V	7765 ± 122	2.97 ± 0.08	Fe II	1.7 ± 0.4
M92/XII-9	M_V, B–V, $\Delta\epsilon$(Fe I–II)	7791 ± 91	2.90 ± 0.08	Fe I & II	2.9 ± 0.6
M92/B202	M_V, $\Delta\epsilon$(Fe I–II)	7854 ± 110	2.93 ± 0.08	Ti II, Fe I & II	3.0 ± 0.5
M92/VI-10	M_V, B–V, $\Delta\epsilon$(Fe I–II)	7905 ± 113	2.98 ± 0.08	Fe II	2.4 ± 0.8
M92/B148	M_V, B–V	7935 ± 141	3.04 ± 0.08	Mg I	3.4 ± 1.6
M92/B251	M_V, B–V, $\Delta\epsilon$(Fe I–II)	8094 ± 136	3.03 ± 0.08	Fe II	2.0 ± 1.8
M92/B466	M_V, B–V, $\Delta\epsilon$(Fe I–II)	8169 ± 127	3.07 ± 0.08	Fe II	1.8 ± 1.1
M92/B219	M_V, $\Delta\epsilon$(Fe I–II)	8197 ± 260	3.02 ± 0.09	Fe II	1.6 ± 0.7
M92/B233	M_V, B–V	8210 ± 177	3.10 ± 0.08	Fe II	1.3 ± 0.7
M92/B30	M_V, $\Delta\epsilon$(Fe I–II)	8274 ± 122	3.04 ± 0.08	Ti II, Fe I & II	2.5 ± 0.8
M92/B145	M_V, $\Delta\epsilon$(Fe I–II)	8479 ± 150	2.89 ± 0.08	Fe I	0.0 ± 1.5
M92/B455	M_V, B–V, $\Delta\epsilon$(Fe I–II)	8584 ± 125	3.06 ± 0.08	Fe II	2.7 ± 2.4
M92/IV-17	M_V, B–V	9048 ± 303	3.28 ± 0.08	Fe II	0.9 ± 0.9
M92/B516	M_V, $\Delta\epsilon$(Fe I–II)	9129 ± 225	3.25 ± 0.08	Fe II	0.3 ± 0.5
M92/B527	M_V, B–V	9394 ± 391	3.25 ± 0.08	Fe II	0.0 ± 0.5
M92/B365	M_V, B–V	11534 ± 813	3.57 ± 0.09		1.0 ± 3.0
M92/B176	M_V, B–V	11616 ± 818	3.65 ± 0.09		1.0 ± 3.0
M68/W464	M_V, B–V, V–I, $\Delta\epsilon$(Fe I–II)	7429 ± 61	2.81 ± 0.07	Fe II	3.1 ± 0.4
M68/W510	M_V, B–V, V–I, $\Delta\epsilon$(Fe I–II)	7554 ± 63	2.90 ± 0.07	Fe II	2.9 ± 1.6
M68/W324	M_V, B–V, V–I	7648 ± 99	2.97 ± 0.07	Ti II, Fe I	2.9 ± 1.4
M68/W114	M_V, B–V, V–I, $\Delta\epsilon$(Fe I–II)	7793 ± 96	2.99 ± 0.07	Fe I & II	2.3 ± 0.6
M68/W340	M_V, B–V, V–I, $\Delta\epsilon$(Fe I–II)	7812 ± 70	2.99 ± 0.07	Fe I & II	1.7 ± 0.7
M68/W468	M_V, B–V, $\Delta\epsilon$(Fe I–II)	8472 ± 184	3.14 ± 0.08	Fe II	1.0 ± 0.3
M68/W120	M_V, B–V	8481 ± 214	3.15 ± 0.08	Fe II	0.4 ± 0.5
M68/W161	M_V, B–V, V–I, $\Delta\epsilon$(Fe I–II)	8620 ± 90	3.20 ± 0.07	Fe II	0.0 ± 0.7
M68/W71	M_V, B–V, V–I, $\Delta\epsilon$(Fe I–II)	8787 ± 115	3.22 ± 0.07		0.5 ± 2.0
M68/W279	M_V, B–V, V–I, $\Delta\epsilon$(Fe I–II)	8843 ± 137	3.21 ± 0.07	Fe II	0.4 ± 0.8
M68/W72	M_V, B–V, V–I	10644 ± 351	3.59 ± 0.07		0.5 ± 2.0
NGC288/B16	M_V, χ(Fe II)	12585 ± 285	3.99 ± 0.07	Fe II	0.5 ± 0.8
NGC288/B186	M_V, χ(Fe II)	12197 ± 252	3.91 ± 0.07	Fe II	0.0 ± 0.5
NGC288/B22	M_V, χ(Fe II)	13115 ± 339	4.00 ± 0.07	Fe II	0.5 ± 0.9
NGC288/B302	M_V, χ(Fe II)	13931 ± 293	4.08 ± 0.07	Fe II	2.0 ± 0.7

5.3.4 Comparison to model tracks

To test the $T_{\rm eff}$ and $\log g$ derived for each of our target stars, we can plot them on a theoretical HR diagram, and compare the points to each other and to the HB locus predicted by stellar models. Figure 5.4 shows points for our 74 stars, along with ZAHB and TAHB (terminal-age horizontal branch) curves from Dorman *et al.* (1993). The measurements are in good agreement with the models, even for the BT stars, which appear too blue or too luminous when Balmer profiles and photometric colors are used to determine $(T_{\rm eff}, \log g)$, but which are much closer to the model tracks with $T_{\rm eff}$ constrained by the spectroscopic excitation balance indicator.

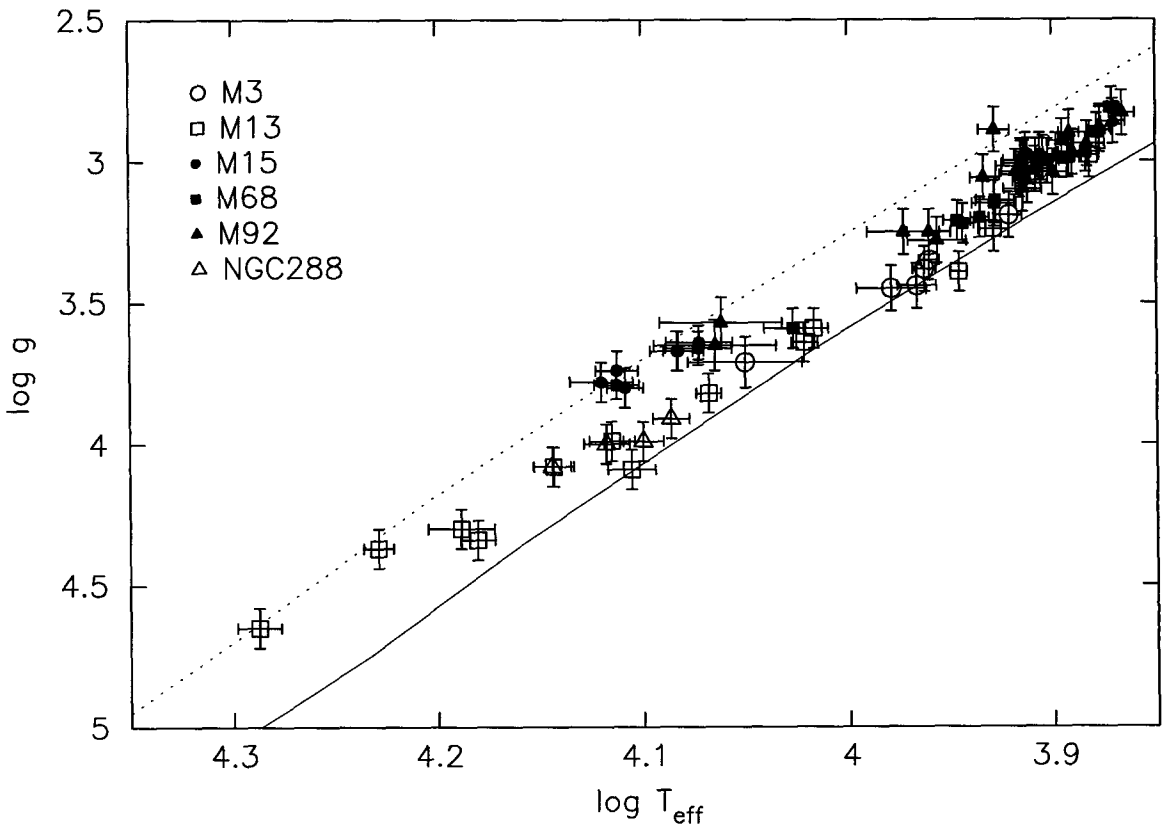

Figure 5.4: The derived $(T_{\rm eff}, \log g)$ for each of our target stars, compared to the model tracks of Dorman *et al.* (1993) for [Fe/H] = −1.48. All the stars should lie between the ZAHB (zero-age HB, solid line) and TAHB (terminal-age HB, dotted line) loci, except for those that have left the HB and are evolving redwards to the AGB or bluewards in an AGB-manqué phase.

5.4 Abundance calculations

5.4.1 Measuring and identifying lines

Because our stellar spectra are uncrowded, consisting of individual metal lines separated by well-defined regions of continuum, we can perform the abundance analysis by reproducing the measured equivalent width of each line, instead of going through a full spectral synthesis for comparison to the observed spectrum. Even for the faster-rotating stars in our sample, the metal lines are close to Gaussian in shape, so we measure equivalent widths W_λ by fitting a Gaussian profile to each line, permitting the depth, width, centroid, and continuum level to vary. In a few cases, lines are sufficiently close together that their wings overlap, so we simultaneously fit the sum of two or three Gaussians. Errors σ_W in equivalent width are determined from the covariance matrix of the errors in the fit parameters. Lines as small as 10 mÅ are reliably measured, and errors are on the order of 5 mÅ for typical spectra.

The list of observed line wavelengths for each star are then matched to the atomic line lists of Kurucz & Bell (1995). For each star, we assume a temperature, gravity, and composition, and use the LINFOR program (below) to construct a catalog of the spectral lines which we expect to appear in the spectrum. (This line catalog is subsequently recalculated as we refine the photospheric parameters of the star.) We reach an initial solution for the radial velocity of the star via a cross-correlation technique, pairing every measured λ with every catalog λ, and making a histogram of the resulting v_r values. A suitable v_r appears as a peak in this histogram. With this provisional velocity shift, we associate each observed line with one or more catalog entries which are within 2σ of the observed rest-frame λ. For that subset of lines which are attributed to a single transition (*i.e.*, unblended), we calculate the mean v_r, and re-identify lines until the star's radial velocity converges. On the basis of v_r, all of our target stars appear to be members of their associated clusters.

We can also consider spectral lines which are too weak to be detected in our spectrum, and thus place stringent upper bounds on the $\log \epsilon$ for important chemical species. First, we identify regions of the spectrum which lie more than 1 Å away from any observed lines. Within each 1 Å bin of these continuum regions, we calculate the RMS scatter $\sigma_{\rm cont}$ of the continuum data, which determines the maximum W_λ of a line that could be hiding in the noise. We define a "maximum unobserved equivalent width" $W_{\lambda,{\rm cont}} = 3\sigma_{\rm cont} \times$ FWHM, using the mean linewidth of the observed lines as a representative FWHM. For each star,

we assemble a separate list of lines from the catalog which do not appear in the spectrum, and assign to each of them an equivalent width equal to $W_{\lambda,\mathrm{cont}}$ for their location in the spectrum. In this way, we account for the changing S/N ratio across each order (due to the blaze function) and from order to order (due to the stellar SED and instrument quantum efficiency).

For many of the hotter stars in our sample, there are significant numbers of unidentified lines. The observed "mystery lines" show similar profiles as the others, and appear at the same rest wavelengths in many different stars, so we can be confident that they are not interstellar lines or chip artifacts. Often, an observed line appears to be clearly associated with a strong transition in the line catalog, but the strength of the observed line is in gross disagreement with abundances or upper bounds derived from other lines of the same species, perhaps due to incorrect $\log gf$ values or unanticipated blends, so these identifications are discarded. Other mystery lines could be associated with highly-ionized species, which are not expected to appear according to our LTE spectral synthesis algorithms, but which may be present in the actual spectra due to the contribution of non-LTE photoionization. The most prevalent of these mystery lines are found at mean rest wavelengths of 4260.48 Å, 4409.53 Å, 4549.56 Å, 4702.95 Å, 4957.55 Å, and 5234.28 Å; although each of these wavelengths is well matched by an entry in the line catalog, the line strengths are discrepant.

The list of line equivalent widths for all our stars numbers many thousands of entries, so it is impractical to reproduce it in its entirety here. A digital version of this data will be made available on CD-ROM, to accompany this document, and will also be uploaded to public archives such as CDS (`http://cdsweb.u-strasbg.fr/`) and ADC (`http://adc.gsfc.nasa.gov/`), so that other researchers may verify our results using their own spectral synthesis techniques. As an example, Table 5.5 lists the measurements for one of our stars, M13/IV-83.

5.4.2 Computing abundances

For the chemical abundance analyses, we use the LINFOR/LINFIT line formation analysis package, based on codes by Baschek, Traving, and Holweger (1966), and subsequently modified by M. Lemke. As inputs, LINFOR accepts an ATLAS9 model atmosphere of a given T_{eff} and $\log g$, a value for microturbulence velocity ξ, and a list of line measurements. We

Table 5.5: Equivalent width measurements for program star M13/IV-83.

λ_{obs} (Å)	W_λ (mÅ)	ID	λ_{rest} (Å)	v_r (km/s)	λ_{obs} (Å)	W_λ (mÅ)	ID	λ_{rest} (Å)	v_r (km/s)
4042.511	84.0 ± 4.0	Fe I	4045.812	−244.8	4464.869	80.9 ± 3.7	Ti II	4468.507	−244.2
4060.298	63.2 ± 4.5	Fe I	4063.594	−243.3	4477.572	184.6 ± 5.0	Mg II	4481.126	−237.9
							Mg II	4481.150	−239.5
4068.430	62.7 ± 5.0	Fe I	4071.738	−243.7			Mg II	4481.325	−251.3
4074.387	37.5 ± 4.7	Cr II	4077.511	−226.6	4497.627	77.9 ± 5.4	Ti II	4501.273	−243.0
		Sr II	4077.709	−229.8	4504.593	45.0 ± 5.7	Fe II	4508.288	−245.9
4074.430	64.7 ± 7.8	Cr II	4077.511	−223.5					
		Sr II	4077.709	−226.7	4518.975	47.4 ± 4.4	Fe II	4522.634	−242.7
4160.275	37.1 ± 3.7	Ti II	4163.648	−243.0	4520.988	21.2 ± 2.9	Fe II	4524.493	−232.4
							Ti II	4524.687	−245.3
4170.109	34.2 ± 4.8	Fe II	4173.461	−241.0					
		Ti II	4173.537	−246.4	4530.258	91.7 ± 5.1	Ti II	4533.969	−245.6
							Fe II	4534.168	−258.7
4212.165	40.2 ± 8.2	Fe I	4215.423	−231.9					
		Sr II	4215.519	−238.7	4545.858	156.5 ± 7.2	Fe II	4549.474	−238.5
		Cr II	4215.738	−254.2			Ti II	4549.617	−247.9
							Ti II	4549.814	−260.9
4223.326	72.1 ± 4.8	Ca I	4226.728	−241.5					
					4545.875	146.9 ± 5.1	Fe II	4549.474	−237.3
4223.343	64.6 ± 5.7	Ca I	4226.728	−240.3			Ti II	4549.617	−246.8
							Ti II	4549.814	−259.7
4229.757	96.2 ± 4.2	Fe II	4233.172	−242.0					
		Cr II	4233.243	−247.1	4560.025	70.7 ± 5.2	Ti II	4563.761	−245.6
4243.426	64.5 ± 4.8	Sc II	4246.822	−239.9	4568.276	86.1 ± 3.8	Ti II	4571.968	−242.3
4268.231	66.4 ± 6.4	Fe I	4271.760	−247.8	4580.103	69.7 ± 4.4	Fe II	4583.837	−244.4
							Fe II	4583.999	−255.0
4286.680	58.9 ± 4.2	Ti II	4290.219	−247.5					
		Ti II	4290.353	−256.8	4699.170	33.3 ± 3.7	Mn II	4702.734	−227.4
							Fe I	4702.913	−238.8
4290.618	63.4 ± 4.4	Ti II	4294.099	−243.2			La II	4703.258	−260.7
		Fe I	4294.125	−245.0					
					4919.969	99.1 ± 5.9	Fe II	4923.927	−241.1
4304.393	82.9 ± 3.5	Ti II	4307.863	−241.6					
		Fe I	4307.902	−244.3	4953.551	31.7 ± 4.0	Fe I	4957.682	−250.0
							Cr II	4957.684	−250.1
4322.264	57.5 ± 6.2	Fe II	4325.540	−227.2			Cr II	4957.800	−257.1
		Fe I	4325.762	−242.6					
					5014.358	130.1 ± 4.4	C I	5018.101	−223.8
4380.009	88.7 ± 6.0	Fe I	4383.545	−242.0			Fe II	5018.440	−244.0
4391.430	83.2 ± 4.9	Ti II	4395.033	−245.9	5163.165	88.3 ± 4.4	Mg I	5167.321	−241.3
							Fe I	5167.488	−251.0
4396.258	44.3 ± 5.5	Ti II	4399.772	−239.6					
					5164.845	142.0 ± 4.5	Fe II	5169.033	−243.1
4401.193	69.1 ± 4.1	Fe I	4404.750	−242.3			Fe I	5169.299	−258.5
4411.639	36.7 ± 3.9	Fe I	4415.122	−236.7	5168.508	102.4 ± 4.2	Mg I	5172.684	−242.2
4414.089	76.4 ± 10.1	Ti II	4417.719	−246.5	5312.324	93.2 ± 9.8	Fe II	5316.615	−242.1
							Fe II	5316.784	−251.6
4440.191	78.3 ± 5.9	Ti II	4443.794	−243.2					

instruct LINFOR to vary the quantity $\log(gf\epsilon)$ for each line until the synthesized equivalent width $W_{\lambda\mathrm{calc}}$ matches the measured $W_{\lambda\mathrm{obs}}$, and then subtract the catalog value for $\log gf$ to get $\log\epsilon$.

A sizable fraction of lines are associated with more than one transition. If both (or all) of the transitions are due to a single species, then LINFOR can do a simultaneous solution and derive $\log\epsilon$ for that species. If two or more different species are blended together, however, the solution is slightly more complicated. In this case, we determine which transition is expected to have the largest contribution to the line, assuming a suitable initial composition for the star. The $\log(gf\epsilon)$ for that primary component is allowed to vary, while the other, weaker components are held fixed. When the abundance analysis is finished, we adjust the parameters for the weaker blend components based on $\log\epsilon$ from the other, unblended lines of those species, and repeat the process until the abundances converge.

Often, the $\log\epsilon$ calculated for many lines of the same species agree to within a few tenths of a dex, except for a few points which are anomalously high or low. These outliers may be due to any one of a number of factors: an unanticipated blend with another line, an erroneous $\log gf$ from the catalog, or a bad W_λ measurement. We identify and remove these outliers manually, prior to calculating $d\log\epsilon/d\chi$ or $d\log\epsilon/dW_\lambda$ for the spectral diagnostic analysis, or the mean μ and dispersion σ for each species in the final abundance analysis.

Once T_{eff}, $\log g$, ξ, and atmospheric [Fe/H] (which we abbreviate as T, g, ξ, and z below) have been determined, we calculate the mean abundance μ and dispersion σ for each chemical species. We determine the error in the mean in the standard statistical fashion, $\sigma_\mu = \sigma(N-1)^{-1/2}$ where N is the number of lines, but also include several other terms in the error analysis. Since the $\log\epsilon$ for each species is dependent upon the adopted photospheric parameters, we recalculate the abundances while varying each of these parameters in turn, and seeing how much the abundances change as a result. More specifically, we compute

$$\begin{aligned}
\sigma_{\log\epsilon}(\Delta T) &= \log\epsilon(T+\sigma_T, g, \xi, z) - \log\epsilon(T, g, \xi, z) \\
\sigma_{\log\epsilon}(\Delta g) &= \log\epsilon(T, g+\sigma_g, \xi, z) - \log\epsilon(T, g, \xi, z) \\
\sigma_{\log\epsilon}(\Delta \xi) &= \log\epsilon(T, g, \xi+\sigma_\xi, z) - \log\epsilon(T, g, \xi, z) \\
\sigma_{\log\epsilon}(\Delta z) &= \log\epsilon(T, g, \xi, z+\sigma_z) - \log\epsilon(T, g, \xi, z)
\end{aligned}$$

for each species, where σ_z is set equal to 0.1 dex. We also evaluate the potential influence

of errors in the equivalent width measurements by recomputing $\log \epsilon$ with $W_\lambda = W_{\lambda,0} + \sigma_W$ for each line, and then set

$$\sigma_{\log \epsilon}(\Delta W_\lambda) = \frac{\log \epsilon(W_{\lambda,0}) - \log \epsilon(W_{\lambda,0} + \sigma_W)}{(N-1)^{1/2}}$$

since the measurement errors are assumed to have a Gaussian distribution.

Upper bounds on $\log \epsilon$ are computed for all catalog lines which do not appear in the observed spectrum, as described previously. No error budget is computed, nor do we attempt to assess blending effects between unobserved lines — each transition is treated as an independent entity. The smallest $\log \epsilon$ for each species is taken as the upper bound for that species' abundance.

5.5 Rotational broadening measurements

Even to a cursory visual inspection, it is clear that the absorption line profiles in our spectra span a range of different linewidths. Some stars have very sharp, narrow lines, while other stars exhibit absorption profiles with velocity widths of several tens of $\mathrm{km\,s^{-1}}$, higher than can be accounted for by thermal or instrumental effects, and with the particular hemicircular shape which implies stellar rotation. We can determine the *projected* equatorial rotation velocity, $v \sin i$, via this line broadening.

Measurement of $v \sin i$ from high-resolution spectra traditionally entails cross-correlation of the target spectrum with a rotation reference star of similar spectral type. The additional broadening in the target star manifests itself in the width of the cross-correlation peak. This approach offers various advantages for moderate S/N data, but it assumes that the template star is truly at $v \sin i \simeq 0\,\mathrm{km\,s^{-1}}$, which is rare. Furthermore, given the abundance peculiarities that many of our stars exhibit, it is difficult to find appropriate spectral analogs. Since we are able to resolve the line profiles of our stars, we instead chose to measure $v \sin i$ by fitting the profiles directly, taking into account other non-rotational broadening mechanisms.

5.5.1 Additional line-broadening sources

Several other mechanisms also contribute to line broadening, and must be properly accounted for in order to deduce $v \sin i$ accurately.

First, an infinitely narrow spectral line will be broadened by the finite width of the spectrograph slit and small aberrations in the instrument's optical system. For each night of observations, we construct an instrumental broadening profile from bright but unsaturated thorium-argon arc lines. We accumulate several hundred lines, and then successively discard those line profiles which deviate most from the mean, until the RMS deviation reaches 1% of peak intensity or less. This technique is very effective at eliminating blended arc lines, residual cosmic ray hits, and otherwise non-representative line profiles from the composite profile. The variation in instrumental broadening over the detector area proves negligible, as the 100 to 200 lines which make up each final composite profile are distributed evenly around the chip. The resulting instrumental profiles are almost perfectly Gaussian, with a FWHM of $6.3\,\mathrm{km\,s^{-1}}$, slightly narrower than that expected for the nominal resolving power of $R = 45000$.

Thermal and microturbulent Doppler broadening is also introduced by the stellar photosphere. We compute a Gaussian with FWHM $= 1.67(2kT_{\mathrm{eff}}/m+\xi^2)^{1/2}$, with $m = 56\,\mathrm{amu} = 9.3 \times 10^{-23}\,\mathrm{g}$ as a typical atomic mass, and ξ from the abundance analysis as described previously. This photospheric broadening profile, typically with a FWHM of 3–4 $\mathrm{km\,s^{-1}}$, is convolved with the instrumental function to get the final broadening profile for each spectrum, which is then convolved with hemicircular rotation profiles of various $v \sin i$ to form the theoretical profiles. Limb darkening is not incorporated into the profile modeling, as it is expected to have only minimal influence on the final result.

5.5.2 Fitting observed profiles

Each observed line in a spectrum, except for helium lines and those that are attributed to a blend of components by the line identification routines, is fit to the theoretical profile using an iterative least-squares algorithm. Four free parameters are used for fitting: $v \sin i$, line center λ_{ctr}, line depth, and continuum level. Data and best-fit profiles for six representative lines in each of three stars are depicted in Figure 5.5. With the exception of a few outliers, the $v \sin i$ values from individual lines appear to follow a Gaussian distribution.

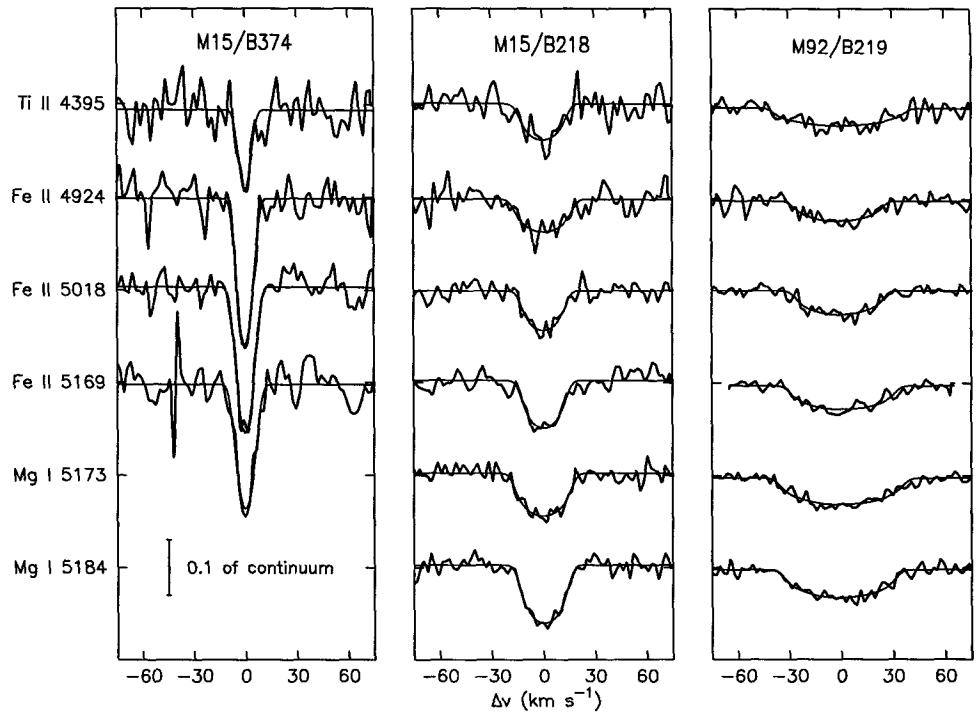

Figure 5.5: Best-fit rotational broadening profiles for six metal absorption lines in M15/B374, M15/B218, and M92/B219.

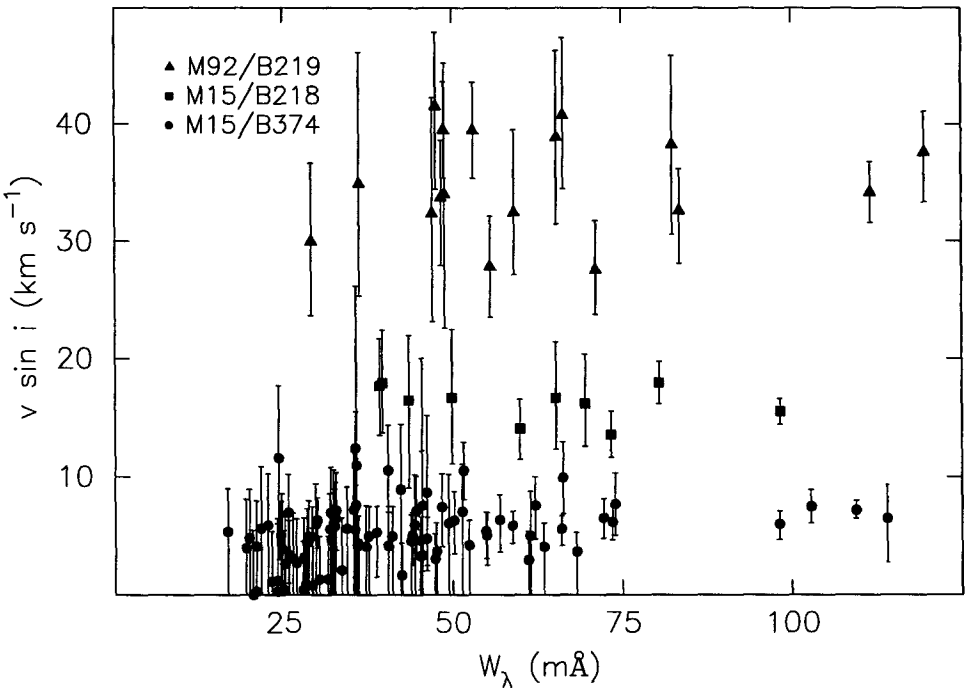

Figure 5.6: The rotation velocity derived from each line, for stars M15/B374, M15/B218, and M92/B219. No statistically significant trend of $v \sin i$ with W_λ is evident.

5.5.3 Evaluating the $v \sin i$ solutions

We can test the accuracy of the $v \sin i$ value derived from each line by comparison to the other values from the same star. As with the abundance calculations, we identify points which clearly lie beyond several σ from the sample mean, and discard them. We also look for secular trends in $v \sin i$ as a function of line strength, which would indicate that saturation of the stronger lines is distorting the underlying Gaussian shape and resulting in anomalously high $v \sin i$ results. In Figure 5.6 we plot $v \sin i$ versus W_λ for several of the narrow-lined stars. Least-squares linear fits to these data show no significant trend, so our profile fitting technique appears to be reliable.

5.5.4 Using the magnesium triplet to estimate $v \sin i$

For some of the hotter, metal-poor stars in our sample, there are very few appropriate metal lines available for the line broadening measurements. This problem particularly affects the spectra of stars M15/B348 and M68/W72, which show one and zero unblended metal lines, respectively. In this case, we turn to the prominent Mg II 4481 triplet, which appears as a single (but anomalously broad) absorption line in both cases. By fitting the 4481 line profile in several other stars with accurately-derived $v \sin i$, we can determine the additional broadening effect introduced by the multiple components of the 4481 line, and then use the width of the line in these two stars to deduce a value for $v \sin i$.

Chapter 6 Results

In this section, we present the results of the abundance and rotation analyses for each of the 74 stars in our sample. We also indicate notable trends and patterns in these data, both as a function of $T_{\rm eff}$ along the BHB locus, and from cluster to cluster.

6.1 Photospheric abundances

Because of their large size, we have placed the chemical abundance results in Appendix A. Table A.1 contains the abundance values derived for each of our target stars, both on an absolute scale, and relative to the solar abundances of Grevesse & Sauval (1998). The full error budget accounting is included. The quantity σ_N represents the RMS scatter of the $N_{\rm lines}$ transitions observed for each species. The error contributions σ_T, σ_g, σ_ξ, and σ_W are as described previously. (The values for σ_z have been omitted, since they are negligible throughout.) The composite error σ_Σ is the quadrature sum of these separate items, with σ_N divided by $(N_{\rm lines}-1)^{1/2}$.

The abundance values for key chemical species are plotted in Figures 6.1–6.10, as a function of $T_{\rm eff}$, subdivided into separate panels for each globular cluster. As far as possible, we use the values for the dominant ionization stage (usually singly-ionized metals) as the best indicator of the actual chemical abundance, since these stages are least susceptible to non-LTE effects. The effective temperature serves to parameterize each star's position along the HB locus, without the bolometric correction issues that would be inherent in a color diagnostic like $B-V$. Admittedly, since the derived temperatures are still subject to errors in the locus-fitting technique and the model-derived photometry, $T_{\rm eff}$ is not the ideal abscissa, but it will suffice for the current purpose. Filled circles are measured abundances as logarithmic offsets from the solar proportion of each element, the horizontal error bars *sans* symbol indicate upper limits, and the horizontal dashed lines mark the canonical metallicity [Fe/H] of each cluster (not incorporating element-to-element variations expected from α-enhancement or CNO dredge-up).

6.1.1 Metal enhancements

We find remarkable enhancements of iron and other metal species among the BT stars. The iron abundances among the B′ stars are close to their respective cluster metallicities, albeit a few tenths of a dex below the [Fe/H] derived from analysis of red giant stars in each of these clusters, as seen in Figure 6.1. The majority of the BT stars, however, show iron content greater than that of the sun, [Fe/H] $\simeq$ 0.0 to +1.0. Depending on the intrinsic metallicity of the cluster, these values represent enhancements of factors of 30 to 300. Titanium, similarly, is found a few tenths of a dex above the cluster baseline in the B′ stars (such α-enhancement is common in metal-poor stars), but then rises by factors of 100 or more in the hotter population (Figure 6.2), although the "step-function" in $\log \epsilon$ is not as pronounced as with iron. A more modest enhancement of approximately a factor of ten is found for calcium (Figure 6.3).

Some metals, such as phosphorus (Figure 6.4), display significantly larger enhancements than iron. We do not observe any P II lines among the cooler stars, but if we assume an appropriately-scaled solar composition for these stars, then the [P/H] $\simeq$ +1.5 that we find for the BT stars implies, in some cases, an enhancement of 3.5 orders of magnitude. These values are each based on several separate spectral lines, in close agreement with each other, so we are confident that they are not due to random errors or line misidentification. We note that a plethora of P II lines was found in the field HB stars Feige 86 and 3 Cen A by Sargent & Searle (1967) and Bidelman (1960), respectively, so phosphorus overabundance may be a common phenomenon on the HB. Similarly large proportions of chromium, manganese, and vanadium (Figures 6.5, 6.6, and 6.7, respectively) appear in a few of the BT stars, but these values often rely on a single spectral line, and are therefore not certain. There are also hints of enormous enhancements for nickel and yttrium in a couple of the program BT stars.

Other light metals, such as magnesium (Figure 6.8) and silicon (Figure 6.9) show little (if any) enhancement. The [Mg/H] abundances that we derive are in close agreement with the canonical metallicities of each cluster, even for the BT stars. There are hints of a slight rise in the magnesium abundance at the highest $T_{\rm eff}$ in M13 and M15, but any such enhancement is small compared to the other metal species. The [Si/H] values show much greater scatter, but again, there is no evidence for a sudden $\Delta \log \epsilon$ between the B′ and

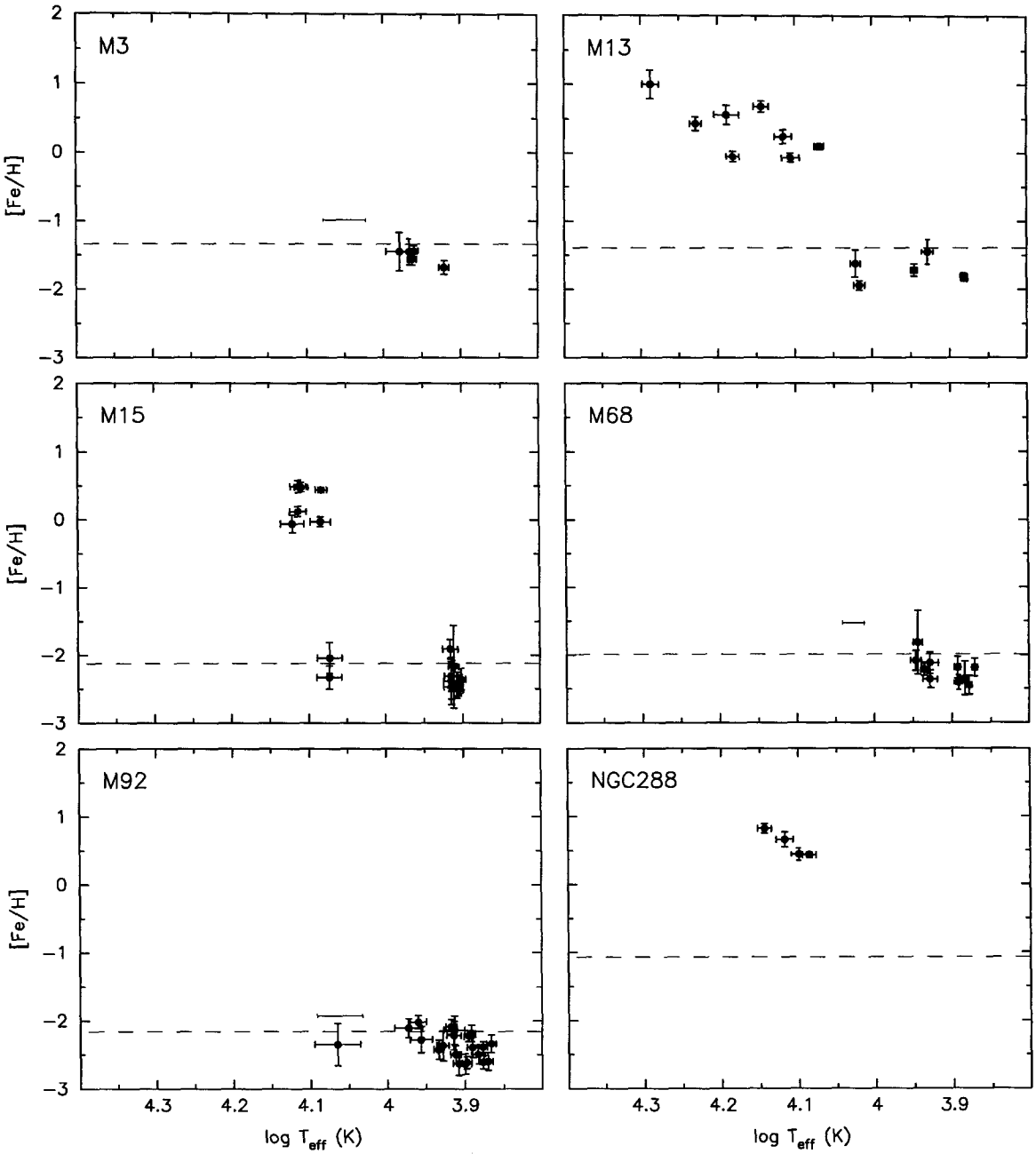

Figure 6.1: Iron abundances [Fe/H] for program stars, plotted as a function of $T_{\rm eff}$, for each cluster. Filled circles are abundances derived from one or more absorption lines, horizontal error bars with no symbol indicate upper bounds based on strong transitions not observed in the spectra, and the dashed lines denote the canonical cluster metallicities.

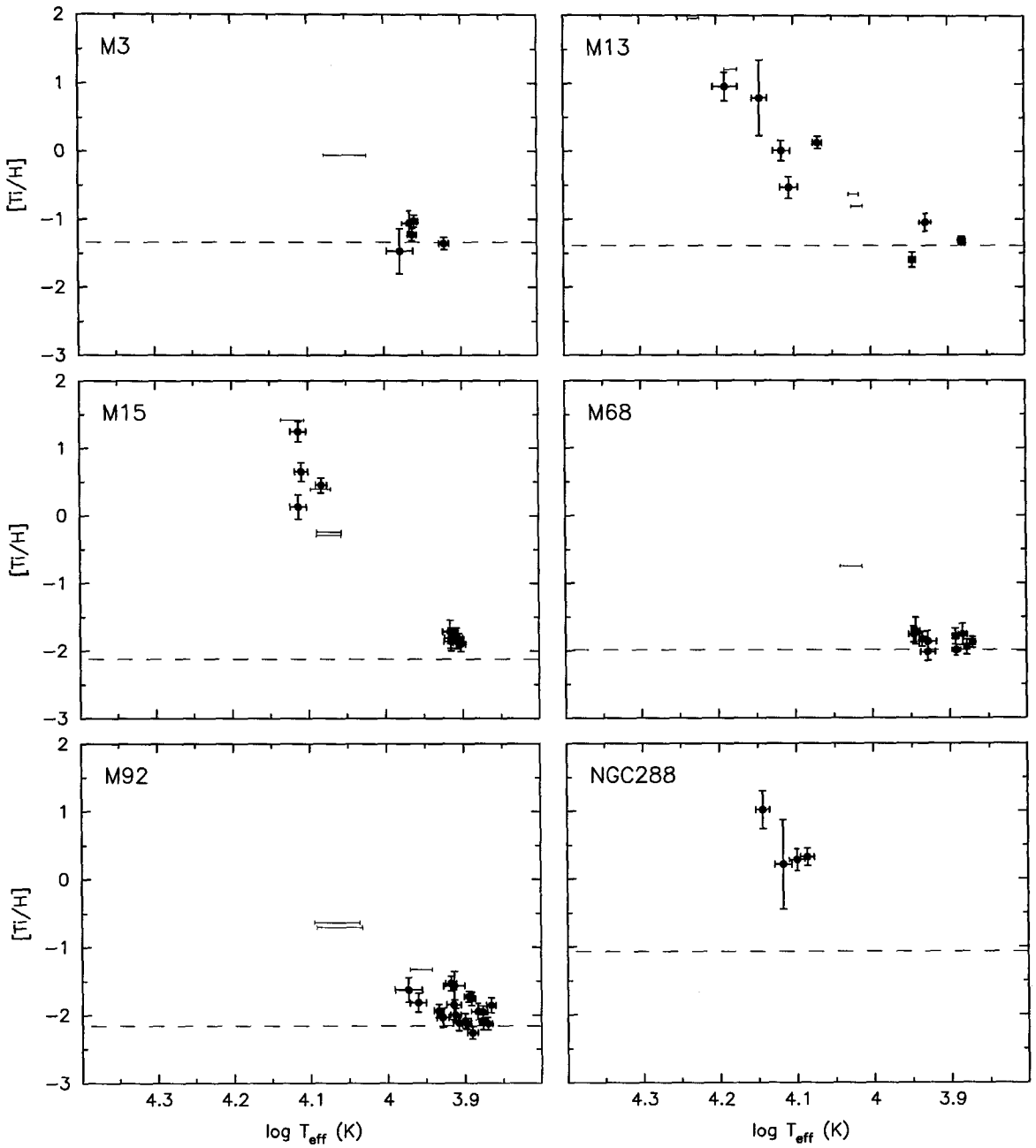

Figure 6.2: Titanium abundances [Ti/H] for program stars.

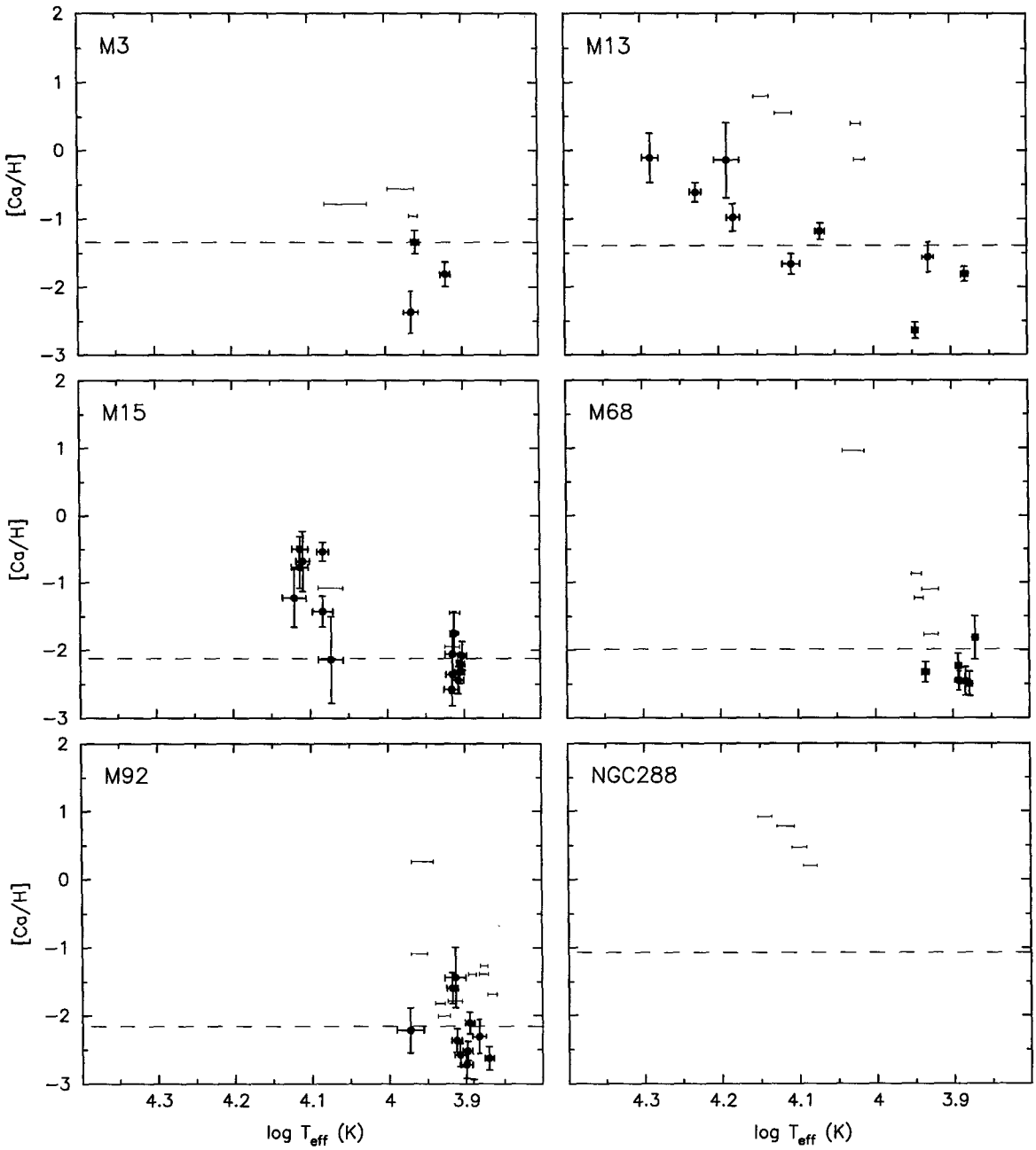

Figure 6.3: Calcium abundances [Ca/H] for program stars.

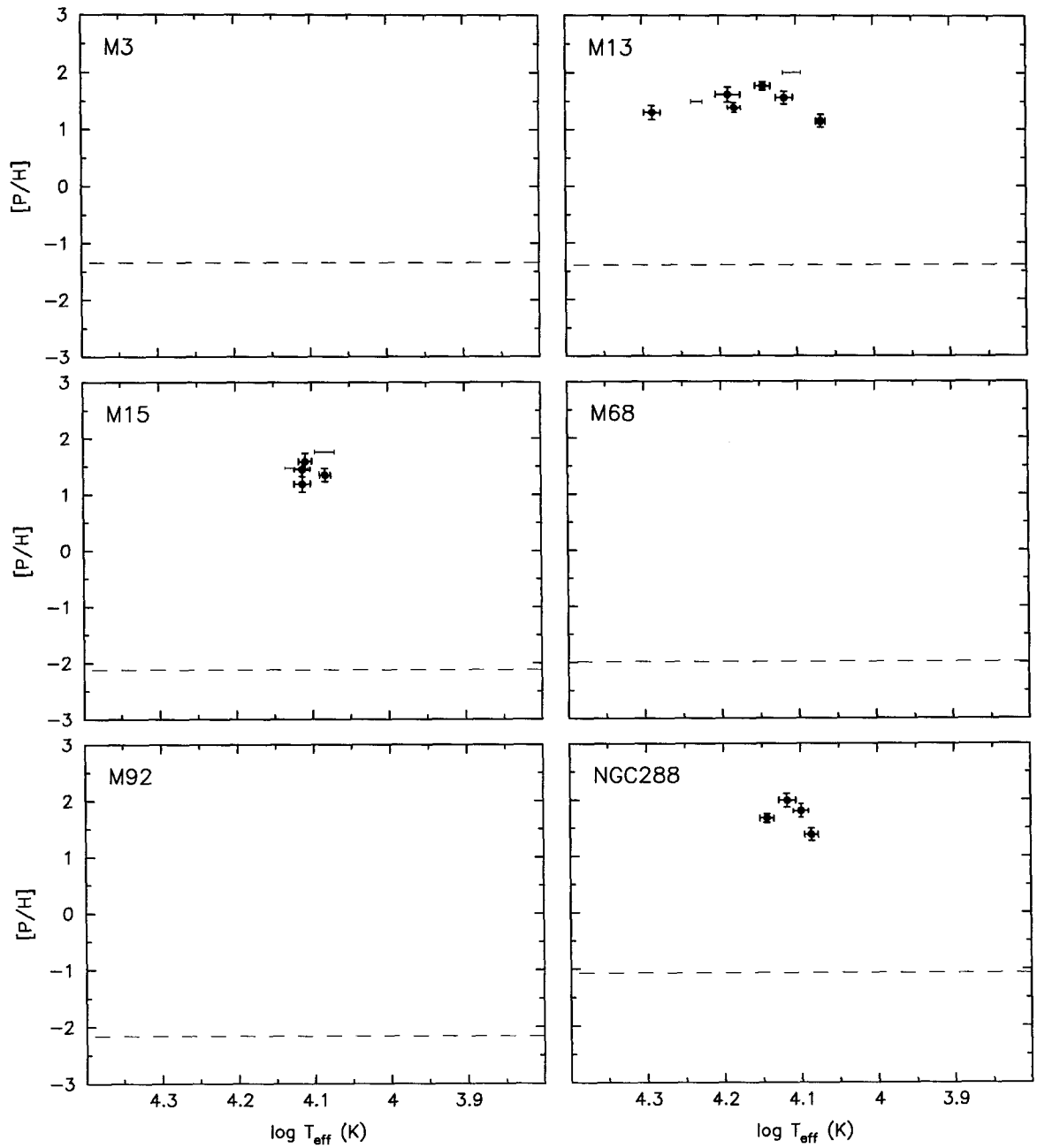

Figure 6.4: Phosphorus abundances [P/H] for program stars.

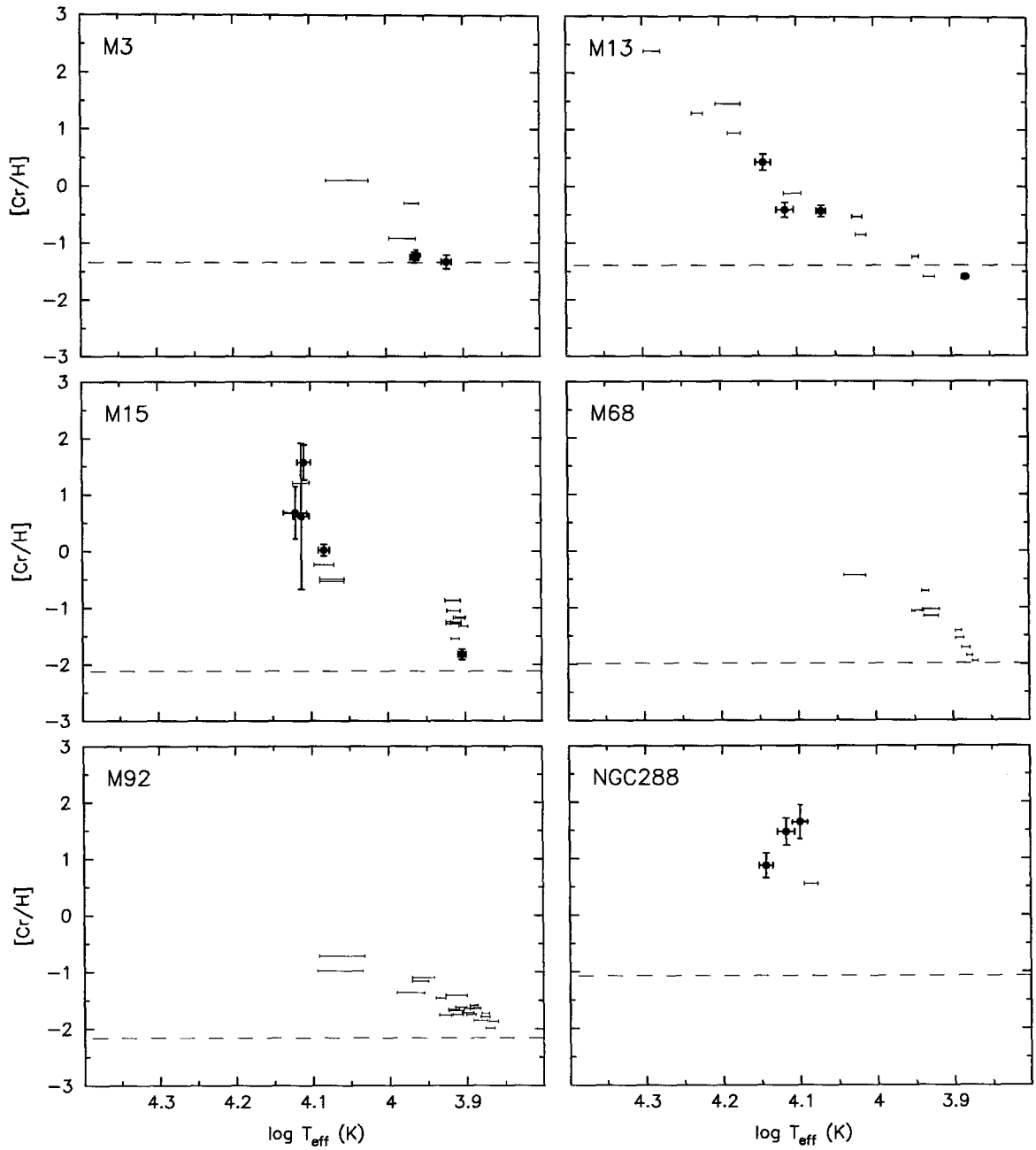

Figure 6.5: Chromium abundances [Cr/H] for program stars.

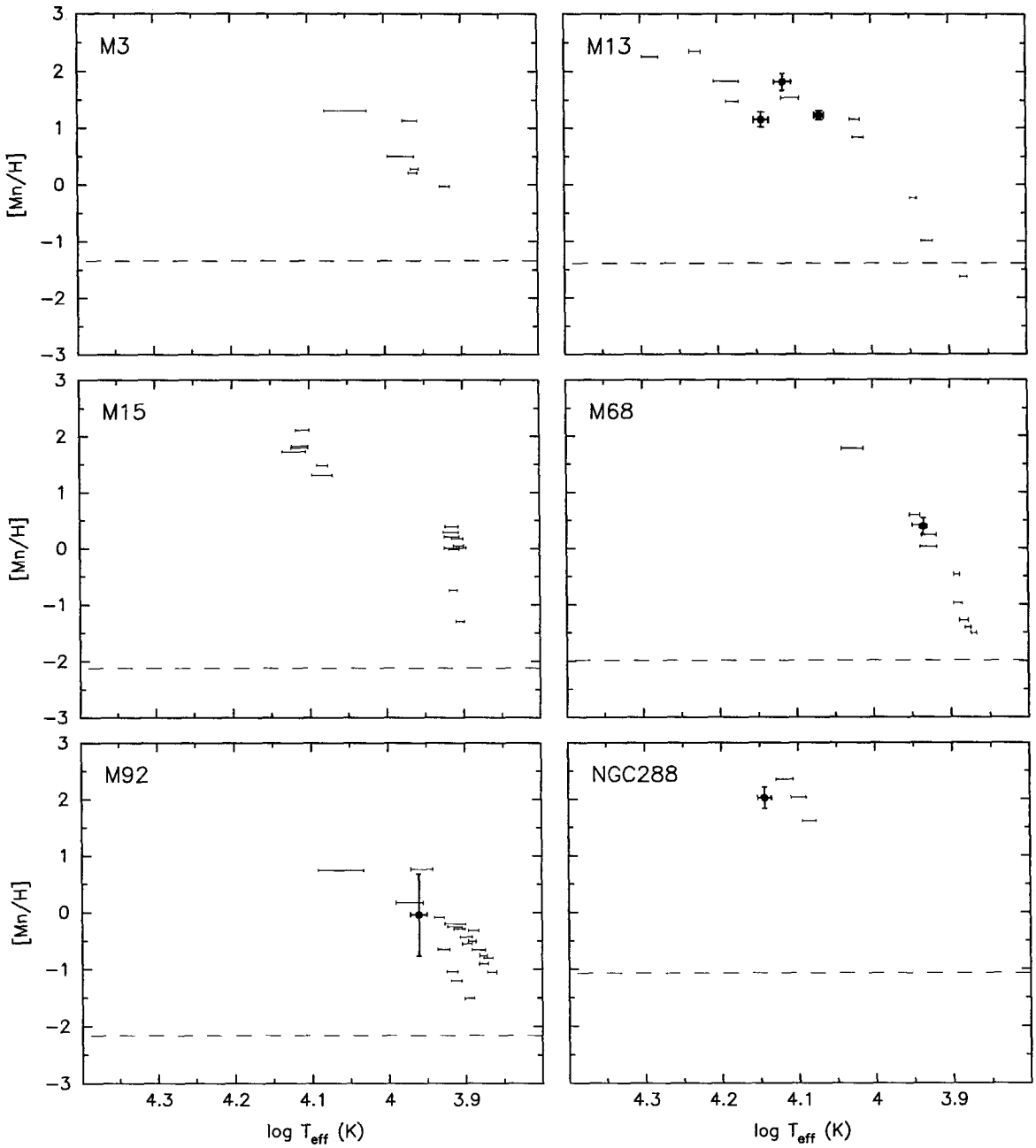

Figure 6.6: Manganese abundances [Mn/H] for program stars.

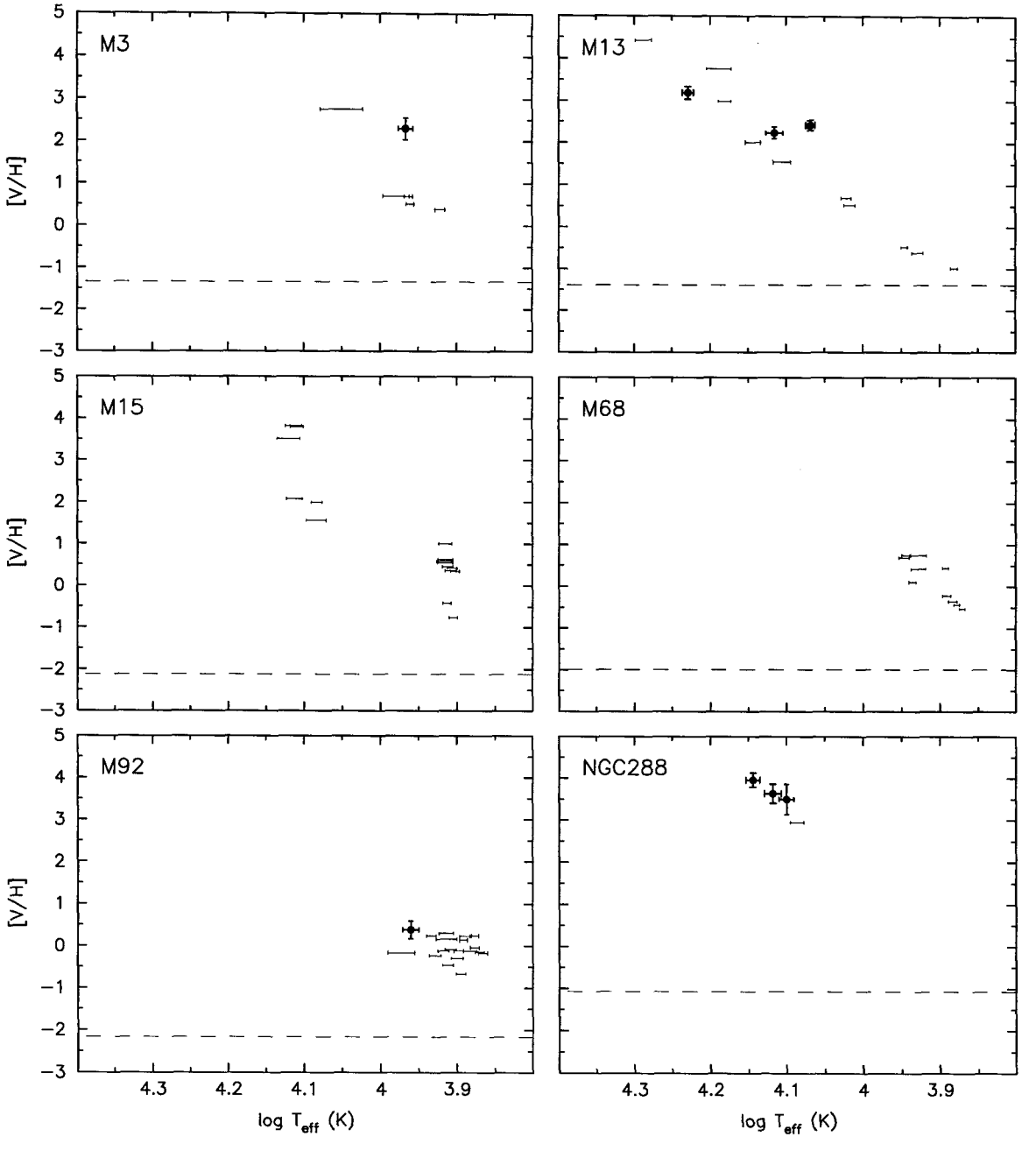

Figure 6.7: Vanadium abundances [V/H] for program stars.

BT regions of the HB. Magnesium and silicon, therefore, appear to be immune to whatever mechanism is producing the enhancements of other metals.

Other metal species — sodium, aluminum, scandium, and strontium — are found in the cooler B′ stars at or near the anticipated cluster metallicities. They do not appear at enhanced levels in the hot stars, although the upper bounds on those species do not rule out this possibility.

This pattern of overabundant iron and normal magnesium that we observe in our stars matches the prior results of Glaspey *et al.* (1989) (§3.2), and the recent work by Moehler *et al.* (1999b) on the southern metal-poor globular NGC6752. Moehler *et al.* observe 42 BHB stars at medium spectral resolution, and derive [Fe/H] and [Mg/H] from the strongest lines of each species. They find a very similar jump in the iron composition for 19 stars above $T_{\rm eff} \simeq 11500\,{\rm K}$, but no appreciable change in the magnesium abundance. Their spectra are not of sufficient resolution or S/N to assess the behavior of other chemical species, but the iron and magnesium results provide an exciting parallel to our findings.

A small fraction of our BT stars do not exhibit these metal enhancements, however. Two of the eight BT stars observed in M15, for instance, have "normal" [Fe/H], *i.e.*, metal-poor, as expected for this cluster, and in agreement with the abundances for the B′ population. Both of the stars are clearly bluewards of gap G1, and have $T_{\rm eff}$ similar to metal-enhanced BT stars. The few stars that we have measured in the very short BTs of clusters M68 and M92 are also unenhanced. We discuss the implications of these anomalously non-anomalous stars in §7.

6.1.2 Helium depletion

The helium composition of our stars also varies strongly as a function of position along the horizontal branch, as can be seen in Figure 6.10. Helium lines are not visible in the coolest of our stars, but at $T_{\rm eff} \simeq 9000\,{\rm K}$, the photospheres become hot enough to excite the He I transitions at 4471, 5016, and 5876 Å, and we find $\log \epsilon({\rm He}) \simeq 11$, as expected for the primordial helium fraction. As we move to hotter and higher-gravity stars, however, the abundance of helium drops in a fairly monotonic fashion, reaching a depletion of 2.5 dex, or a factor of 300, in the hottest BT stars sampled. This behavior is most clearly illustrated by the stars in M13, and corroborated by the subsolar helium abundances in M15 and NGC288.

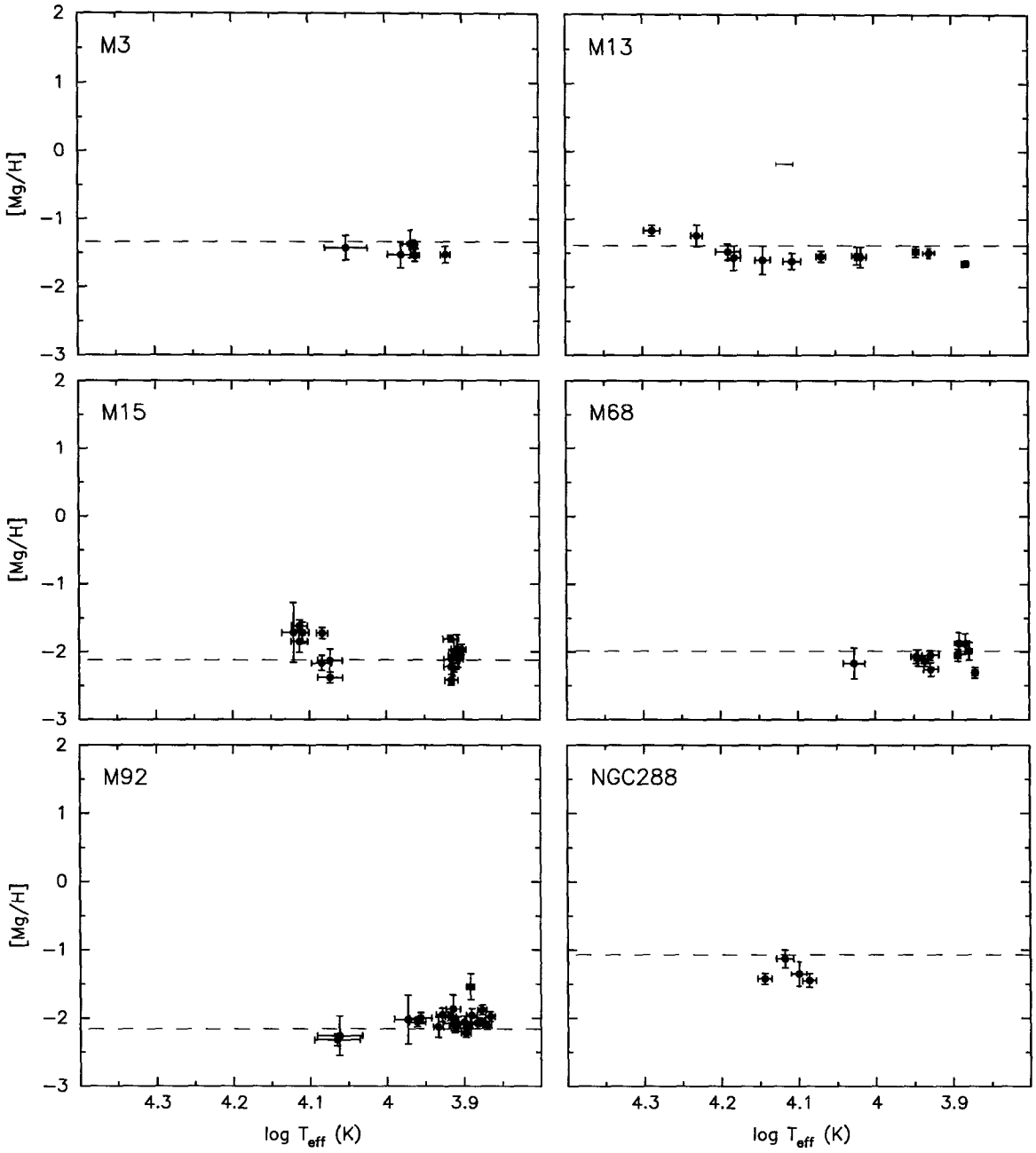

Figure 6.8: Magnesium abundances [Mg/H] for program stars.

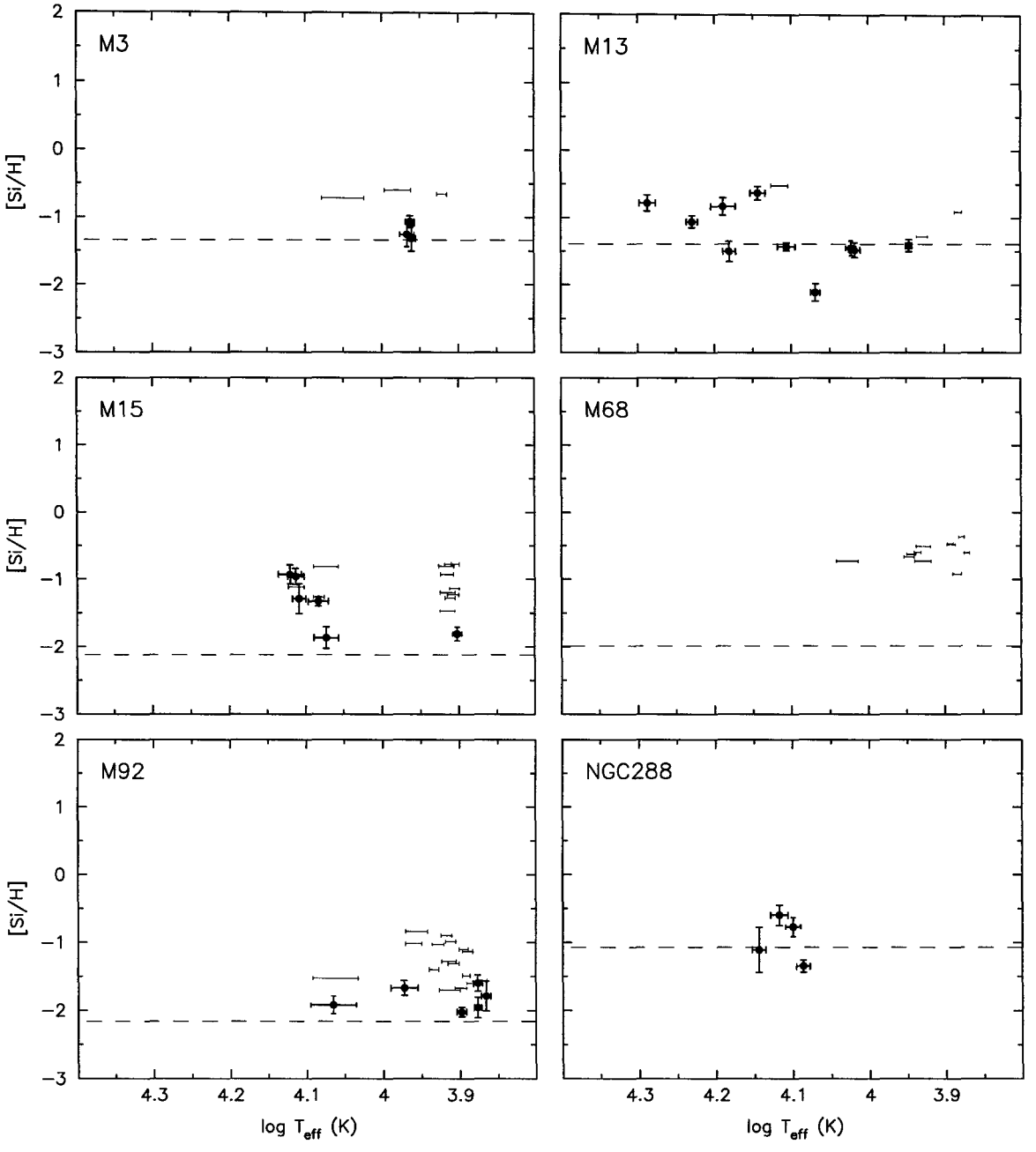

Figure 6.9: Silicon abundances [Si/H] for program stars.

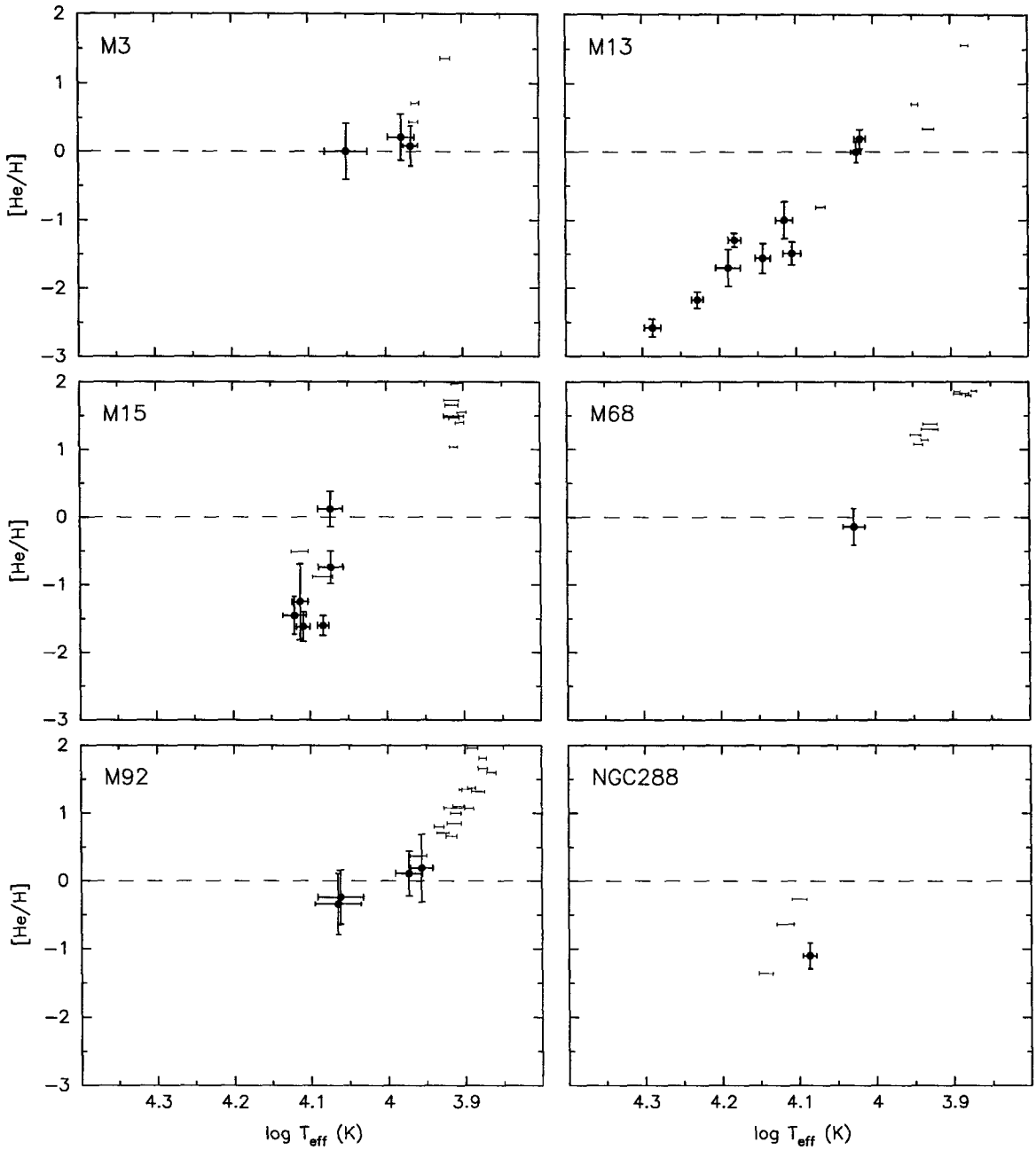

Figure 6.10: Helium abundances [He/H] for program stars.

6.2 Projected rotation velocities

Table 6.1 lists the projected rotation velocities that we measure for our target stars. The asterisks next to M15/B348, M68/W72, and M92/B365 indicate the use of the Mg II 4481 triplet in the linewidth measurement, as previously described. Figure 6.11 displays these results in a fashion similar to the abundance plots. All of the points in the figure have both horizontal and vertical error bars, but in many cases the error σ_v is so small (when $N_{\rm lines}$ is large) that the error bars are obscured by the plot symbol itself. Also included are the $v \sin i$ results of Peterson *et al.* (1995) (open symbols), which provide a useful statistical overview of other B′ stars in M3, M13, and NGC288.

6.2.1 Comparison to previous measurements

A handful of our stars — four in M13, and two in M3 — are in common with Peterson's target list, and the independent assessments of $v \sin i$ appear to agree well within the quoted errors. In order to check for any systematic difference between these two different determinations, we plot $(v \sin i)_{\rm Peterson}$ versus $(v \sin i)_{\rm Behr}$ in Figure 6.12. The best-fit line does not deviate significantly from a unity relation, so it appears that their technique for solving $v \sin i$ and $\log \epsilon$(O II) simultaneously is reliable. There is, perhaps, a slight vertical offset, with their values consistently $\sim 2.5\,{\rm km\,s^{-1}}$ higher than ours, but any such discrepancy will have little effect on the overall patterns.

Line-broadening analysis of five of our B′ stars in M92 was reported previously by Cohen & McCarthy (1997). Our $v \sin i$ values for these stars are nearly a factor of two smaller than theirs, because of a bug in their profile convolution routines. The values in Table 6.1, therefore, supersede the prior results.

6.2.2 Deprojecting the $\sin i$ term

The measurement of rotation velocity via Doppler line broadening is inherently statistical, since the polar axis of each star is oriented randomly in space, and introduces an unknown $\sin i$ term to the measured quantity. Techniques do exist to deduce the inclination angle or rotation period of a star directly, using Doppler imaging or timing of the transit of surface features, but most of our stars would not be expected to show starspots or other spatial surface variability, and the combined dispersion and S/N requirements would be prohibitive

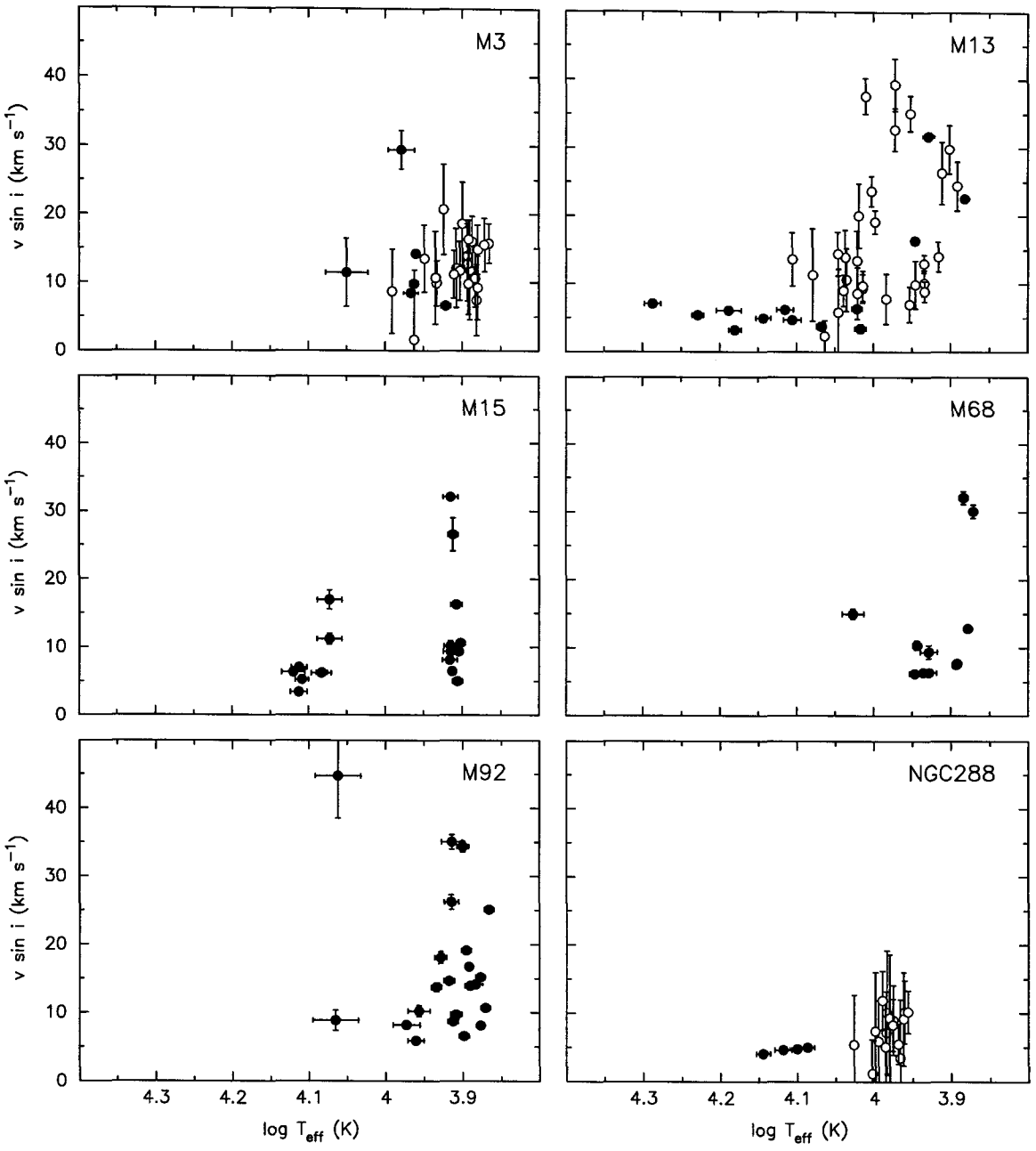

Figure 6.11: Rotation velocities $v \sin i$ as a function of $T_{\rm eff}$ for stars in each of the six clusters. Solid symbols are from this work, while the open symbols are the measurements of Peterson *et al.* (1995).

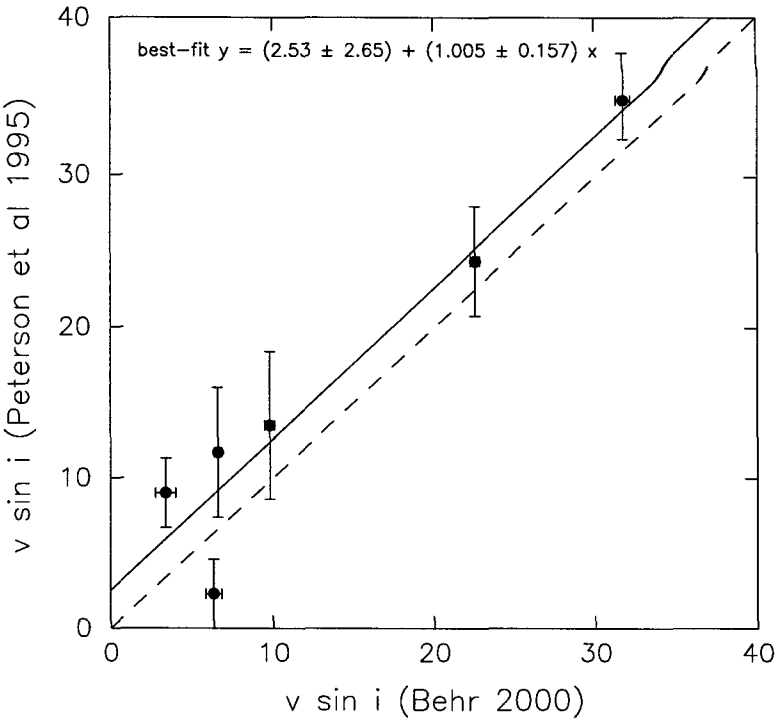

Figure 6.12: A comparison of $v \sin i$ values for stars observed both by us and by Peterson *et al.* (1995). A least-squares fit to the points (solid line) differs from the unity relationship (dashed line) only by a slight constant offset.

in any event.

The only way around the unknown $\sin i$ for each star, then, is via a large statistical sample, such that we can assume an isotropic distribution of polar axis orientation, and a resulting probability function $P(s)ds = s\left(1 - s^2\right)^{-1/2} ds$, where $s = \sin i$. With several stars at the same position along the HB axis, we can then assess, with reasonable confidence, how a set of measured $v \sin i$ translates into a value or range of $v_{\rm rot}$.

Qualitatively, the distribution of $\sin i$ is such that large values are more likely than small values. This is convenient, as it means that a single $v \sin i$ measurement is not a terribly bad estimate of the true $v_{\rm rot}$ of the star. The probability that $\sin i < 0.5$, for instance, is only 0.13, and $\sin i < 0.25$ happens only 0.03 of the time. A small $v \sin i$ value generally implies a small $v_{\rm rot}$, therefore, and several small $v \sin i$ strongly constrain the likelihood of a large underlying $v_{\rm rot}$.

Quantitatively, we can use the Kolmogorov-Smirnov (KS) test to compare a set of observed $v \sin i$ values to an assumed underlying distribution of $v_{\rm rot}$. We cycle through a range of $v_{\rm rot}$ values, and test the analytic cumulative probability distribution for a unimodal or

multimodal rotation population against a cumulative distribution derived from the empirical measurements, using the KS parameter P (see Press *et al.* (1992) for details of the algorithm) to indicate the likelihood that the observed values were drawn from the given distribution. We evaluate the B′ and BT populations of each cluster separately, and assess each of three cases:

- The underlying population consists of a single rotation velocity v_1.
- A fraction f_1 of the underlying population rotates at v_1, and the remainder $f_2 = 1 - f_1$ rotates at v_2.
- A fraction f_1 rotates at v_1, a fraction f_2 rotates at v_2, and the remainder $f_3 = 1 - f_1 - f_2$ is at v_3.

We step through this parameter space $(v_1, f_1, v_2, f_2, v_3, f_3)$, coarsely at first, and then with successively finer increments, to find the maximum values of P for each of the unimodal, bimodal, and trimodal hypotheses above. The results are compiled in Table 6.2. Values of P approaching unity indicate a very good agreement between the modal model and the observed range of $v \sin i$. For the B′ populations, bimodal or trimodal distributions are required to fit the data, as surmised from qualitative assessments. (In many cases, for a trimodal fit, two of the v_i values are very similar, suggesting a spread in intrinsic velocities rather than a true bifurcation in the distribution.) For the BT stars, a single $v_{\rm rot}$ is all that is required to reproduce the observed broadenings, except for the two anomalous fast rotators in M15. The poor P-value for the BT of NGC288 is due to the small sample size.

6.2.3 Rotation rate along the BHB

The most significant aspect of our rotation measurements is that B′ stars and BT stars have very different distributions of $v \sin i$ values, implying a large difference in the actual rotation rates. Some B′ stars reach $v \sin i$ as high as 20–40 $\mathrm{km\,s^{-1}}$, depending on the cluster, while the BT stars are limited to 8 $\mathrm{km\,s^{-1}}$ in nearly all cases. Based on the statistical expectations for $\sin i$ discussed above, this disparity is clearly due to a real difference in rotation rate between B′ and BT, rather than chance polar orientation. Almost all of the BT stars, therefore, are inherently slow rotators.

There are exceptions to this claim. Two BT stars in M15, B334 and B348, are clearly to the blue side of gap G1, but they are rotating somewhat faster than the other BT stars,

12 and 14 $\mathrm{km\,s^{-1}}$ respectively. These are the same two stars which, as described above, also show non-metal-enhanced photospheric abundances. Similarly, the two BT stars observed in M92 and one in M68 show $v \sin i > 8\,\mathrm{km\,s^{-1}}$, and [Fe/H] detections or upper bounds commensurate with a metal-poor population. We discuss the potential implications of this relation in §7.

Although the sample size for B′ stars in each of our clusters is not terribly large, we can still say with certainty that the cool stars are not all rotating at the same intrinsic v_{rot}. If they were, then we should see most of the $v \sin i$ values at or slightly below a single threshold level, with only a very few measurements much smaller than the threshold. Instead, in M15, M68, and M92, we see a majority of the stars clustering at 10–15 $\mathrm{km\,s^{-1}}$, but then a sizable fraction at significantly *higher* $v \sin i$. Such a distribution cannot be explained by a single fast v_{rot} of 30–40 $\mathrm{km\,s^{-1}}$, with projection effects producing the low-$v \sin i$ stars, for the reasons cited above. Instead, as the KS modeling shows, there is a bimodal distribution of v_{rot} for the B′ stars, with approximately a third of the stars belonging to the fast population ($v_{\mathrm{rot}} \simeq 35\,\mathrm{km\,s^{-1}}$), and the other two-thirds being slow rotators ($v_{\mathrm{rot}} \simeq 15\,\mathrm{km\,s^{-1}}$). We will refer to these two subsets as $\mathrm{B}'_{\mathrm{fast}}$ and $\mathrm{B}'_{\mathrm{slow}}$, respectively. This claim of bimodality was made by Peterson regarding their large sample of B′ stars in M13. Within the limitations of our smaller sample size, we can make the same claim for M15, M68, and M92.

6.2.4 Rotation rate from cluster to cluster

The series of papers by Peterson (1983a, 1983b, 1985, 1995) measure BHB $v \sin i$ values in six globular clusters, and find very different maximum $v \sin i$ for each. In the 1985 paper, she notes an interesting correlation between the HB morphology and the maximum observed $v \sin i$ in each cluster, wherein the clusters with faster peak $v \sin i$ are also those with longer blue tails. In addition to confirming her measurement techniques, we can now add three more clusters which were not observed in these prior studies. The B′ stars in M15, M68, and M92 all appear to be very similar to those in M13, with a bimodal distribution peaking at $\sim 35\,\mathrm{km\,s^{-1}}$ and a slower component at $\sim 15\,\mathrm{km\,s^{-1}}$. Unfortunately, these new data do not support the prior correlation, as M92 and M68 have rather short BTs.

Table 6.1: Rotation velocities $v \sin i$ for target stars.

cluster/star	$v \sin i$ (km s^{-1})	$N_{\rm lines}$	cluster/star	$v \sin i$ (km s^{-1})	$N_{\rm lines}$
M3/B125	14.22 ± 0.38	33	M68/W71	10.41 ± 0.65	10
M3/B244	29.39 ± 2.83	9	M68/W72	14.97 ± 0.74	2 *
M3/B445	11.44 ± 5.00	1	M68/W114	7.69 ± 0.26	31
M3/B518	6.60 ± 0.21	47	M68/W120	9.39 ± 0.99	6
M3/B831	9.81 ± 0.32	31	M68/W161	6.39 ± 0.35	20
M3/B1241	8.45 ± 0.54	18	M68/W279	6.25 ± 0.38	15
			M68/W324	32.10 ± 0.95	17
M13/IV-83	31.72 ± 0.44	25	M68/W340	7.54 ± 0.26	24
M13/J11	22.54 ± 0.28	53	M68/W464	30.08 ± 0.98	21
M13/SA113	6.35 ± 0.49	6	M68/W468	6.36 ± 0.48	9
M13/SA404	3.39 ± 0.63	8	M68/W510	12.85 ± 0.33	30
M13/WF2-2541	3.20 ± 0.27	40			
M13/WF2-2692	6.06 ± 0.22	33	M92/B29	13.92 ± 0.55	11
M13/WF2-3035	16.37 ± 0.43	17	M92/B30	14.63 ± 0.34	34
M13/WF2-3123	7.07 ± 0.24	15	M92/B103	14.13 ± 0.31	23
M13/WF2-820	6.17 ± 0.38	27	M92/B145	18.08 ± 0.84	13
M13/WF3-1718	3.72 ± 0.10	151	M92/B148	34.37 ± 0.80	7
M13/WF3-548	5.38 ± 0.27	18	M92/B176	8.85 ± 1.50	4
M13/WF4-3085	4.93 ± 0.13	111	M92/B202	19.10 ± 0.20	27
M13/WF4-3485	4.67 ± 0.23	50	M92/B219	35.03 ± 1.06	17
			M92/B233	26.21 ± 1.08	9
M15/B78	9.33 ± 0.26	27	M92/B246	10.70 ± 0.35	24
M15/B84	6.17 ± 0.19	45	M92/B251	9.72 ± 0.27	16
M15/B124	6.46 ± 0.27	39	M92/B365	44.71 ± 6.23	2 *
M15/B130	4.99 ± 0.24	18	M92/B455	13.73 ± 0.62	12
M15/B153	32.07 ± 0.44	4	M92/B466	8.71 ± 0.30	26
M15/B177	10.60 ± 0.48	23	M92/B516	5.89 ± 0.55	21
M15/B203	6.35 ± 0.24	32	M92/B527	8.19 ± 0.22	8
M15/B218	16.25 ± 0.48	10	M92/IV-17	10.22 ± 0.82	6
M15/B244	9.36 ± 0.42	20	M92/IV-27	15.18 ± 0.34	21
M15/B267	7.00 ± 0.16	81	M92/VI-10	6.56 ± 0.22	26
M15/B279	6.24 ± 0.16	115	M92/X-22	8.11 ± 0.32	19
M15/B315	3.39 ± 0.27	54	M92/XII-1	25.10 ± 0.34	19
M15/B331	8.11 ± 0.48	15	M92/XII-9	16.70 ± 0.34	15
M15/B334	11.19 ± 0.77	3			
M15/B348	16.92 ± 1.40	2 *	NGC288/B16	4.77 ± 0.22	87
M15/B374	5.23 ± 0.27	92	NGC288/B186	4.98 ± 0.14	126
M15/B424	26.53 ± 2.43	2	NGC288/B22	4.60 ± 0.19	93
M15/B558	10.19 ± 0.71	12	NGC288/B302	4.08 ± 0.15	177

Table 6.2: Kolmogorov-Smirnov tests of multimodal $v_{\rm rot}$ distributions.

population	v_1 (f_1)	v_2 (f_2)	v_3 (f_3)	$P_{\rm KS}$
M3 B′	15.7 (1.00)			0.16058
M3 B′	12.0 (0.25)	16.4 (0.75)		0.85802
M3 B′	11.8 (0.39)	16.4 (0.45)	30.3 (0.15)	0.99796
M13 B′	19.3 (1.00)			0.00683
M13 B′	11.3 (0.51)	31.7 (0.49)		0.71511
M13 B′	10.4 (0.21)	14.7 (0.39)	32.8 (0.40)	0.99464
M13 BT	6.2 (1.00)			0.96019
M13 BT	5.3 (0.26)	6.6 (0.74)		0.98443
M13 BT	5.2 (0.25)	6.3 (0.54)	10.0 (0.20)	0.98811
M15 B′	13.0 (1.00)			0.27527
M15 B′	10.6 (0.74)	33.9 (0.26)		0.99984
M15 B′	9.4 (0.09)	10.7 (0.60)	33.6 (0.31)	0.99997
M15 BT	8.0 (1.00)			0.63251
M15 BT	6.7 (0.61)	13.6 (0.39)		0.96930
M15 BT	6.5 (0.55)	12.8 (0.28)	23.1 (0.17)	0.97558
M68 B′	10.6 (1.00)			0.27527
M68 B′	8.2 (0.25)	13.0 (0.75)		0.77095
M68 B′	8.2 (0.42)	13.0 (0.21)	36.3 (0.37)	0.87288
M92 B′	18.3 (1.00)			0.13925
M92 B′	14.1 (0.61)	25.3 (0.39)		0.70656
M92 B′	8.3 (0.13)	15.6 (0.55)	30.7 (0.32)	0.98337
NGC288 B′	10.2 (1.00)			0.95367
NGC288 B′	9.2 (0.36)	10.6 (0.64)		0.99829
NGC288 B′	7.4 (0.19)	10.2 (0.57)	11.3 (0.24)	0.99987
NGC288 BT	5.3 (1.00)			0.58382

Chapter 7 Explanations and implications

Having presented our observational results and described some of the evident trends and correlations in the data, we will now detail our current best understanding of why these stars appear the way they do. Some characteristics, such as the helium depletion and metal enhancements, are well understood, although details remain to be worked out. Other issues, like the range of rotation velocities, are somewhat more difficult to understand.

7.1 Abundance variations via element diffusion

7.1.1 Basic mechanism

Underabundances of helium have been observed previously in many hot, evolved stars, including subdwarf B (sdB) stars in the field and BHB stars in globular clusters (Baschek, 1975; Heber, 1987; Glaspey *et al.*, 1989). Michaud, Vauclair, and Vauclair (1983, henceforth MVV), building on the original suggestion by Greenstein *et al.* (1967), explain these underabundances as a result of gravitational settling of helium. If the outer atmosphere of the star is radiative, without convection or other large-scale flows to keep it well-mixed, then the helium atoms, with a larger mean molecular weight than the hydrogen, will diffuse downwards into the stellar interior. The actual helium content of the star remains unchanged, but the line-forming layers of the photosphere become depleted, and the He absorption lines will appear weaker than otherwise.

The MVV calculations indicate that helium depletion should be accompanied by photospheric enhancement of heavier elements, as the same stable atmosphere which permits gravitational settling also permits radiative levitation of metals. Elements which present sufficiently large cross-sections to the outgoing radiation field will experience radiative accelerations greater than gravity, and will diffuse upwards, enriching the photosphere at the expense of the interior. The models suggest that overabundances of factors of $10^3 - 10^4$ from a star's initial composition could be supported by radiation pressure, in the absence of any competing mixing mechanisms or selective mass-loss.

We can understand the gross behavior of the diffusion models by considering the very

basic equations of motion governing the migration of chemical species in a stellar atmosphere. We adopt the formalism of Gonzalez *et al.* (1995), although similar derivations are followed by MVV and Seaton (1997). The radiative acceleration on a species A is given by the product of the total photon momentum, the fraction of the Rosseland mean opacity due to the given species, and the integrated opacity, weighted by the blackbody profile:

$$g_R(A) = \frac{L_r^{\rm rad}}{4\pi r^2 c}\,\frac{\kappa_R}{X_A}\int_0^\infty \frac{\kappa_\nu(A)}{\kappa_\nu({\rm total})}\,P(u)du$$

where $u = h\nu/kT$ is the dimensionless frequency parameter and the normalized blackbody flux is determined by

$$P = \frac{15}{4\pi^4}\,\frac{u^4 e^u}{(e^u-1)^2}\,.$$

This upward radiative force is opposed by the local gravity g, and under these competing forces, atoms of that species will diffuse at a rate

$$N_i v_i = D_i\left(-\frac{dN_i}{dr} + N_i\,\frac{m_A(g_R - g)}{kT}\right)\,.$$

The sign of the motion, obviously, is determined by whether g_R or g is larger, as the concentration gradient dN_r/dr is ordinarily quite small. The $L_r^{\rm rad}$ term in the expression of g_R follows the surface gravity g quite closely as one moves along the ZAHB locus, so most of the change in the direction and magnitude of the diffusion term will be due to the opacity parameters κ_R and $\kappa_\nu(A)$, which vary with the photometric parameters and from element to element.

We can estimate the relative amount of levitation experienced by each element by summing the predicted equivalent widths for every catalog line over the visible and near UV spectral range. For a $T_{\rm eff} = 11000\,$K, [Fe/H] $= -1.5$ BHB star, for instance, we find $\Sigma W_\lambda({\rm He}) \simeq 120\,$mA, $\Sigma W_\lambda({\rm Mg}) \simeq 670\,$mA, and $\Sigma W_\lambda({\rm Fe}) \simeq 2460\,$mA, for lines between 3500 and 6000 Å. The magnitudes of these net equivalent widths suggest that helium will experience only a weak levitation force, insufficient to oppose gravity, magnesium will be levitated by an intermediate amount, perhaps balanced by gravity, and iron will be strongly levitated. This is admittedly a crude approach, and more sophisticated models of diffusion are clearly called for.

7.1.2 Refining the quantitative models

Any comprehensive model of atmospheric diffusion will have to explain several aspects of our observational results. Theoretical modeling of diffusion mechanisms has progressed since MVV, although none of the recent work in the literature deals with BHB stars in particular. A variety of other stellar contexts have been modelled, however, and these diffusion calculations offer some insights into our observations. Conversely, our quantitative measurements provide stringent tests on several parameters pertaining to the diffusion mechanisms, so we hope this project stimulates further theoretical work on the specific case of BHB stars.

A good model should quantitatively reproduce the magnitude of enhancement or depletion experienced by each element. Different metals show very different degrees of enhancement, due in large part to their differing radiative cross-sections, as discussed in the previous section. To properly reproduce the observed patterns, sophisticated opacity functions for each species must be incorporated into atmosphere simulations, taking into account the opacity contributions and line blocking due to the other species present. Although modern opacity tables and algorithms have not yet been applied to BHB atmosphere models, Turcotte *et al.* (1999) and Richer *et al.* (2000) have studied the atmospheres of main-sequence A and F types in an attempt to explain, in detail, the abundance patterns observed in chemically peculiar (CP) stars. Their predictions for the relative amounts of enhancement/depletion are illustrated by Figure 11 of Richer *et al.*, which we reproduce here as Figure 7.1. For a slowly-rotating main sequence star with temperature and gravity roughly analogous to our cooler BT stars, their predicted abundance patterns imitate our empirical findings surprisingly well, albeit with much smaller magnitudes of $\Delta \log \epsilon$. Iron is enhanced by 0.7 dex in their models, titanium by 0.3 dex, and phosphorus, chromium, and manganese by 0.8 dex. The radiative levitation forces on magnesium and silicon appear to be closely balanced with gravity, as [Mg/H] and [Si/H] in the models is largely unchanged, just as in our BHB stars. Finally, helium is depleted in the simulations, by 0.2 to 0.3 dex.

We must also explain why the metal enhancements, especially for iron, appear so abruptly, so that the transition from metal-poor to metal-rich photospheres takes place over a span of less than 1000 K in $T_{\rm eff}$. Caloi (1999) suggests that this bifurcation is due to the disappearance of subsurface convection layers at a critical $T_{\rm eff}$ threshold, and this qualitative assessment has received some important support from work done by Sweigart (2000).

His model atmospheres for cooler BHB stars are fully convective, but at $T_{\rm eff} \simeq 8000\,{\rm K}$, the atmospheres become radiative. However, there still exist thin layers of convection, just below the surface, at isotherms corresponding to hydrogen and helium ionization. As the photospheric temperature increases, these isotherms move closer to the surface, until $T_{\rm eff} \simeq 11500\,{\rm K}$, at which point the last of these convection layers disappears, and the atmosphere is fully radiative. Since convection is highly efficient at preventing diffusion from operating, the presence or absence of even modest amounts of subsurface convection may be the "switch" that regulates the appearance of the metal enhancements. The helium depletion, presumably, also requires the disappearance of the convective mixing, and becomes more pronounced under higher-gravity conditions, such that we see a monotonic decrease in [He/H] as we move bluewards along the BT.

The degree of enhancement $\Delta \log \epsilon$ displayed by a particular star also appears to depend strongly on its initial (unenhanced) composition, as BT stars in metal-poor clusters exhibit much larger $\Delta \log \epsilon$ for some elements than equivalent BT stars in intermediate-metallicity clusters. In fact, for iron and phosphorus, it appears that metal-enhanced stars achieve the same maximum abundance for each of these elements, independent of the baseline abundance of the cluster. This behavior is demonstrated by the BT stars in M15, M13, and NGC288. The mean [Fe/H] for BT stars with $4.05 < \log T_{\rm eff} < 4.25$ is +0.27, +0.24, and +0.55, respectively, while the cluster metallicities span a much larger range: −2.12, −1.39, and −1.07. Phosphorus, similarly, reaches very similar [P/H] of +1.48, +1.48, and +1.69 in these three clusters. The most likely explanation for this commonality is that the radiative levitation mechanism achieves equilibrium with gravity when each element reaches some threshold $\log \epsilon$. As the strongest lines of each element become saturated, they are unable to support further enhancements, and the abundance of that element stabilizes. The most metal-rich of these three clusters, NGC288, does show slightly higher [Fe/H] and [P/H] among its BT stars, so this levitation ceiling may not be an absolute limit, but peak abundance appears to be only weakly coupled to the initial metallicity.

One additional factor which can influence the diffusion mechanisms is the rotation rate of the star. This issue was approached from a theoretical standpoint by MVV. In their models, rotation velocities of a few tens of $\rm km\,s^{-1}$ induced meridional circulation currents of sufficient magnitude to prevent the appearance of element diffusion. Our general results support this conclusion, as metal enhancements and helium depletion only appear among

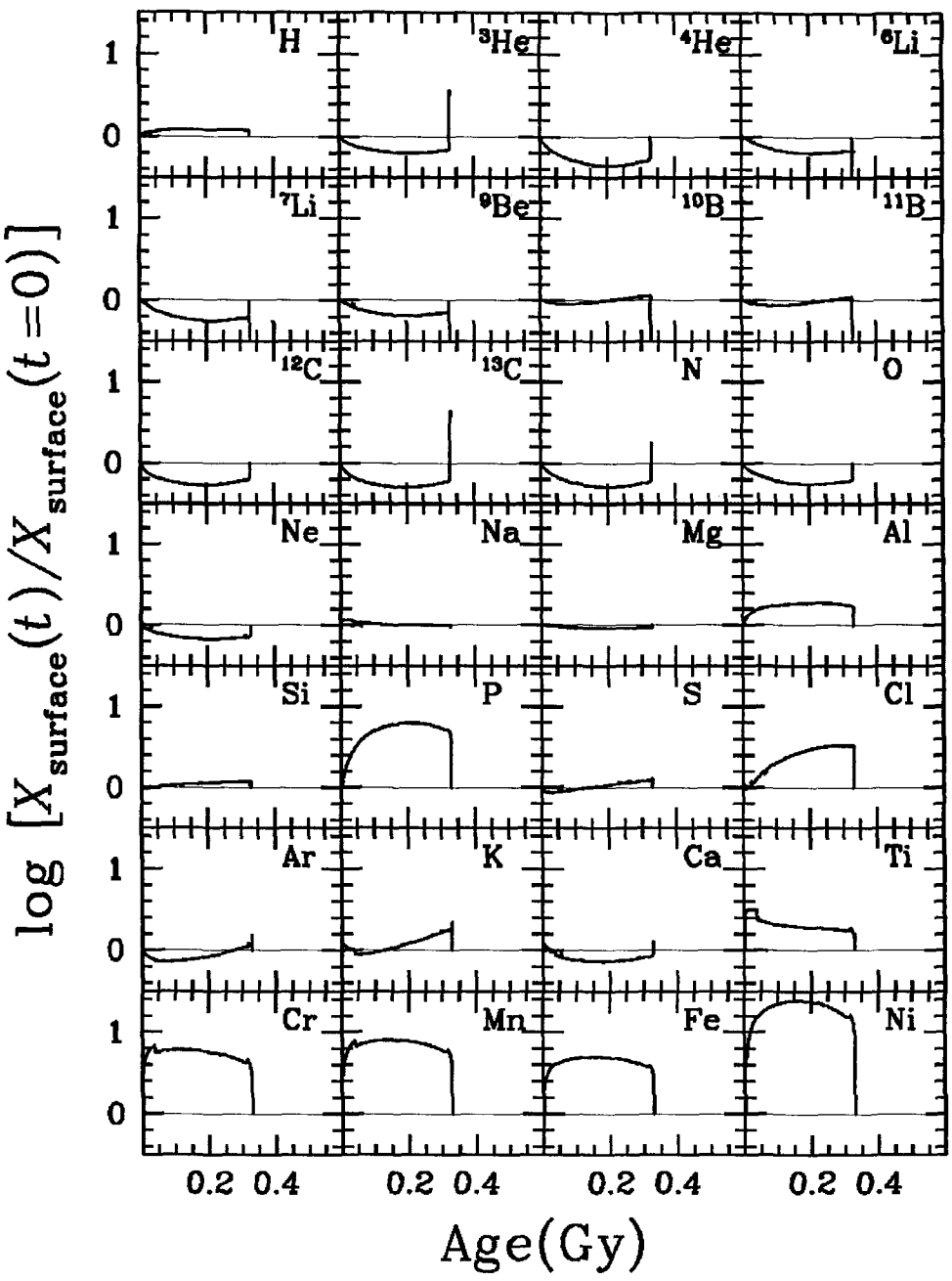

Figure 7.1: Abundance enhancements for different elements, from the atmospheric diffusion models of Richer *et al.* (2000).

the most slowly-rotating stars. Additional evidence is provided by the anomalous BT stars in M15, M68, and M92, which were previously mentioned in §6.1.1 and 6.2.3. Their positions in the clusters' CMDs associate them with the BT population, but they both show [Fe/H] and $v \sin i$ which are more in keeping with the B′ stars. One possible explanation for this disparity is that their rotation velocities are indeed faster than some threshold $v_{\rm rot}$ (for as-yet-undetermined reasons), and the resulting circulation currents keep their atmospheres well-mixed at the baseline composition expected for the cluster.

We should note that despite this apparent link between rotation and diffusion, we *cannot* make the argument that the abrupt onset of diffusion-driven abundance anomalies is directly caused by the change in rotational signature. If $v_{\rm rot}$ was the sole parameter determining the activation of the diffusion mechanisms, then we would expect to see high-metallicity and low-metallicity stars coexisting among the B′ population. Instead, all the B′ stars are metal-poor as expected, with no evident correlation between $v \sin i$ and [Fe/H]. It appears most likely that both conditions — slow rotation and the absence of subsurface convection — must be met in order for the abundance peculiarities to appear.

7.1.3 Impact on stellar broadband colors

Since the spectral energy distribution emerging from a stellar photosphere is strongly dependent on the opacity distribution, and hence the metallicity, of the atmosphere, it is well worth investigating whether the large metal enhancements that we find in the BT stars might be responsible for the photometric peculiarities — gap G1 and the U-band overluminosities — described in §2.3. Normally, increased metal content produces redder photometric colors, as the atmosphere expands and the larger surface area prompts a smaller $T_{\rm eff}$. However, given the somewhat nontraditional nature of these high metallicities, which may only exist in the stellar photosphere and affect different elements to very different degrees, detailed modeling will be required to determine their true impact on the spectral flux distribution.

Some initial quantitative work in this regard has been performed by Grundahl *et al.* (1999). Based on the presence of u-band jumps along the BHB, as measured by Strömgren uy photometry of a large sample of globular clusters, they suggested that radiatively-levitated metal enhancements might be common among BT stars, and could be the agency responsible for the G1 gaps and the anomalously low BT gravities. They propose a mech-

anism whereby an abrupt increase in metal-line opacity, particularly in the ultraviolet, reduces the relative contribution of hydrogen opacity. Since the U and Strömgren u bands are located just bluewards of the Balmer jump, where hydrogen is the dominant opacity source, the increased metal opacity will actually result in *higher* flux in this region of spectrum, and the near-UV magnitude will be brighter. Using ATLAS9 flux models, they estimate that a metallicity increase from [Fe/H] $= -1.5$ to $+0.5$ can raise the u brightness by 0.3 mag. This amplitude is commensurate with the u-jumps that they observe, and may also be adequate to shift the $U - V$ color bluewards to create a gap in the CMD.

Moehler *et al.* (1999b) explore the possibility that such metal-enhancements and the resulting changes in the atmospheric structure might also account for the anomalous gravities. For BHB stars in the metal-poor globular cluster NGC6752, they derive $T_{\rm eff}$ and $\log g$ from model fits to observed Balmer line profiles, adopting several different metallicities and helium abundances. They find a modest improvement in the agreement between the observational HR diagram and the theoretical ZAHB locus for a solar metallicity scaled by $+0.5$ dex and helium at -2.0 dex, but the convergence is even better when the models include mixing of helium into the hydrogen-burning shell. (This sort of deep mixing might be expected as a result of core rotation, which will be discussed in §7.2.1.) The levitation of metals, then, appears to provide a partial explanation of the BT overluminosities.

A great deal of further modeling, as well as additional photometry in far-UV, near-UV, and visible bands, will be required before the full influence of these metal enhancements can be known. From the initial assessments, however, it appears that the abundance anomalies do play a significant role in altering the photometric characteristics of the BT stars.

7.1.4 Impact on population characteristics and stellar evolution

If the photometric properties of HB stars are being significantly altered by the presence of these metal enhancements, might this affect derivations of cluster parameters such as age and distance, which are based on comparisons of observed photometric sequences with model isochrones? In practice, this is not a great concern, because techniques based on the absolute magnitude of the HB, or the magnitude difference between the HB and the main-sequence turnoff, generally use only the cooler RHB stars, whose atmospheres are fully convective and hence remain well-mixed. Derivations of cluster age and distance scales, then, remain intact.

These metal enhancements might, however, strongly influence the far-UV characteristics of old stellar populations like globular clusters and elliptical galaxies. In the absence of hot young high-mass stars, evolved BHB and EHB stars (and the less-numerous but more-luminous AGB-manqué and post-AGB stars) are the primary sources of ultraviolet flux, so that even a small EHB population can greatly influence the overall integrated SED of such a system. EHB populations are now thought to be the leading explanation of the "UV-upturn effect" in globular clusters, so it is crucial to know whether these EHB stars might be metal-enhanced like their BHB cousins, and if so, to what extent. Increased surface abundances of the heavy elements in hot HB stars have been invoked by Vink *et al.* (1999) in order to improve the agreement between their synthetic spectra and far-UV observations of globular cluster M79. Further work will be necessary to determine whether such effects might also be relevant for the elliptical galaxy population syntheses of Yi *et al.* (1999) and others.

Our measurements of diffusion in stellar atmospheres, particularly the gravitational settling of helium, also pertain to the diffusion that takes place in stellar interiors. From several different lines of argument, including helioseismological p-mode splittings (Brun *et al.*, 1998) and isochrone fitting to Hipparcos HR diagrams of nearby dwarfs (Lebreton *et al.*, 1999), it appears that settling of helium (and possibly metals as well) does take place deep within solar-type stars, and must be incorporated into the models in order to make them properly fit the observational data. The surface effects which we observe in the BHB stars occupy an entirely different regime of temperature and density, but do provide an excellent opportunity to test our understanding of the diffusion mechanisms. Any refinements made to the models of atmospheric element migration from comparison to our results will reflect on the analogous case of stellar interiors and lead to more accurate predictions of the structure and main sequence lifetimes for these stars.

7.2 Rotation

7.2.1 Anomalously fast B′ rotation

Our line broadening measurements of B′ stars in M13 and M3 verify the large $v \sin i$ values derived by Peterson *et al.* (1995), and we extend the sample to M15, M68, and M92, where $\mathrm{B}'_{\mathrm{fast}}$ stars are also found, with speeds of 20–40 $\mathrm{km\,s^{-1}}$.

The existence of such fast rotation is difficult to explain. The progenitors of these BHB stars were solar type or later, and are expected to have shed most of their angular momentum via magnetically-coupled winds early in their main-sequence lifetimes, reaching the $v_{\rm rot} < 2\,{\rm km\,s^{-1}}$ observed in the Sun and other similar Population I dwarfs. Assuming solid-body rotation and a homogeneous distribution of angular momentum per unit mass, Cohen & McCarthy (1997) estimate that the BHB stars should be rotating no faster than $10\,{\rm km\,s^{-1}}$. More sophisticated modeling, such as that of Sills & Pinsonneault (1999), find similarly modest BHB rotation rates given $v_{\rm rot} < 4\,{\rm km\,s^{-1}}$ on the main sequence and reasonable assumptions about angular momentum evolution during the RGB ascent. These predictions do not conflict seriously with the measured $v \sin i$ for the $\mathrm{B}'_{\rm slow}$ or BT stars, but they clearly pose a challenge for the $\mathrm{B}'_{\rm fast}$ population.

7.2.2 A quickly-rotating core?

The most popular explanation for the presence of $\mathrm{B}'_{\rm fast}$ stars in these clusters is that magnetic braking on the main sequence only affects a star's envelope, and leaves a rapidly-rotating core containing much of its original angular momentum. This reservoir of angular momentum persists throughout the star's main sequence lifetime, and is then revealed only after a large fraction of the envelope is lost on the RGB. This core-envelope decoupling was first proposed by Pinsonneault *et al.* (1991), and is cited by Peterson *et al.* (1995) as the most likely cause for the fastest rotators in their sample.

Such core behavior could explain the fast rotators, although it is not immediately obvious why only a third of the HB stars would show such an effect. Moreover, this model does not agree with the slow core rotations inferred for young stars (Bouvier *et al.*, 1997; Queloz *et al.*, 1998) and the solar interior (Corbard *et al.*, 1997; Charbonneau *et al.*, 1998). Admittedly, these measurements of Population I stars cover a very different metallicity regime from the HB progenitors in metal-poor globulars, so we can envision means by which such core rotation is still plausible for the GC stars — a weaker magnetic dynamo due to lower metal opacity and hence slower convection, for instance. Core rotation is also still frequently invoked to promote helium mixing in the interior (Sweigart & Catelan, 1998).

We can, however, dismiss core rotation as a direct second-parameter candidate. This possibility had been forwarded by Peterson *et al.* (1995), based in large part on the apparent correlation between the maximum $v \sin i$ of the B' stars in a cluster and the presence of

a BT. They noted that M13, with its long EBT, also had the largest $v \sin i$ values, while M3 and NGC288 were found to have significantly lower maximum rotation, and shorter (or nonexistent) BTs. We find similarly high $v \sin i$ for M15, which also has a long extended blue tail, but M68 and M92 also appear to have very fast B'_{fast} stars, despite possessing much shorter BTs.

Our results also undermine the mechanism which had been proposed to explain this correlation. Mengel & Gross (1976) first suggested that fast core rotation in pre-HB stars nearing the tip of the red giant branch would forestall the helium flash, such that more envelope mass would be lost to stellar winds, causing the star to end up further to the blue when it reached the HB. Additionally, Sweigart & Catelan (1998) point out that the helium mixing induced by core rotation can elevate the luminosity of the hydrogen-burning shell, such that the mass-loss rate on the RGB increases, and even more envelope mass is lost. Both of these mechanisms would function on a star-by-star basis, so one would thus expect to see higher rotation in the hotter stars, as faster core rotation yields a smaller M_{env}/M_{core} ratio, and the quickly-rotating core is revealed by progressively greater amounts of RGB mass loss. Instead, the hotter stars, which have suffered greater mass loss, are observed to have slower rotation velocities.

A somewhat different approach to core rotation has been recently suggested by Sills & Pinsonneault (1999). They point out that the transfer of angular momentum from a rapidly-rotating core to spin up the envelope may happen on timescales comparable to the HB lifetime of a star. If this is true, then stars will still have slowly-rotating envelopes when they first arrive on the HB, and appear as part of B'_{slow} subset. Over time, however, the angular momentum hidden in the core is coupled to the envelope, and the star spins up to become a B'_{fast} object. The transfer of angular momentum in a stellar interior can be prevented, however, if large gradients in the mean molecular weight exist within the star. Such gradients could be created by the gravitational settling of helium exhibited by BT stars, such that the core rotation takes much longer to reach the surface. This would explain why nearly all of the BT stars are slow rotators. Qualitatively, this model appears plausible, but a great deal of further work will be required to determine if it is quantitatively viable. S&P also suggest that since the fast rotators have been on the HB for a longer period of time, they will also have evolved towards slightly higher luminosity, so we should find the B'_{fast} stars to be brighter than the B'_{slow} stars. We find no such correlation for our

target list, or for the Peterson *et al.* (1995) data set, although the photometric data are not terribly precise for most of the stars. More accurate photometry and a larger set of $v \sin i$ measurements of B′ stars could conclusively address this intriguing hypothesis.

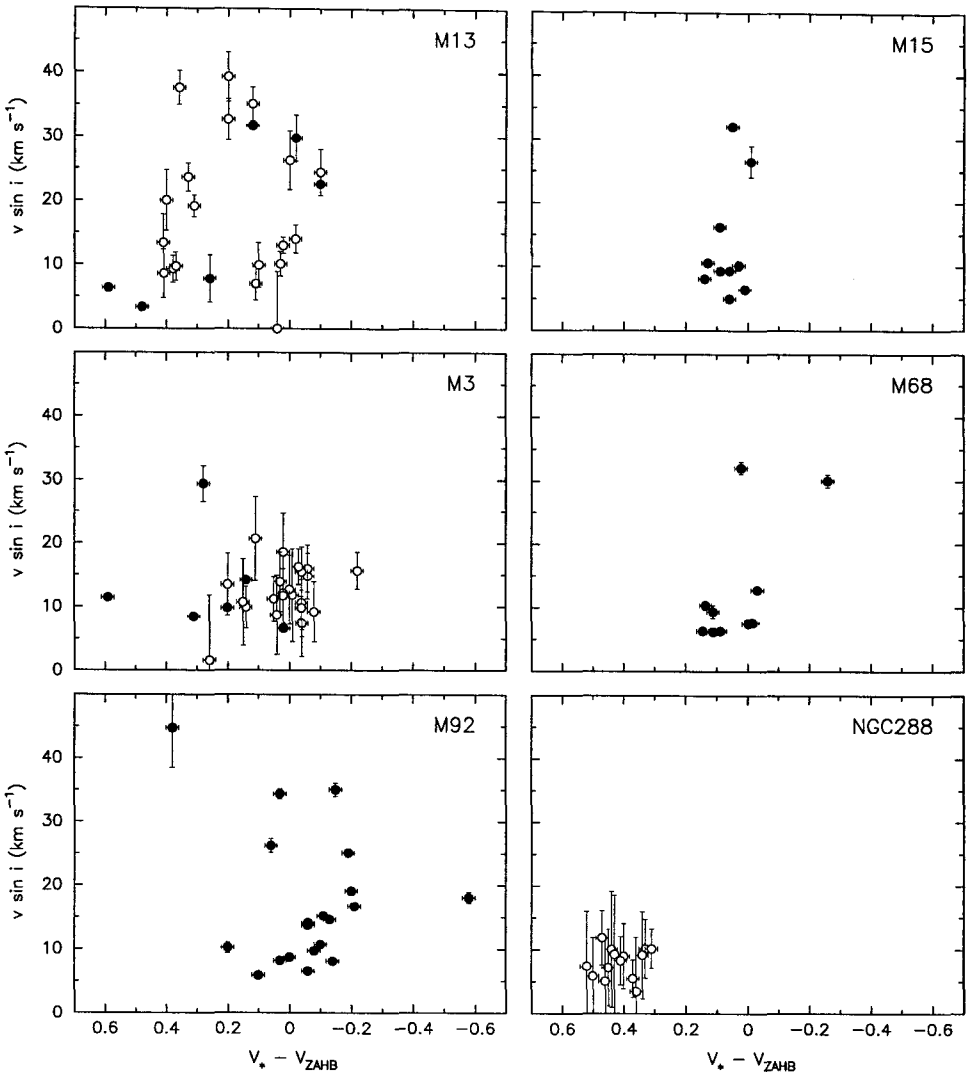

Figure 7.2: Rotation velocity $v \sin i$ plotted against ZAHB overluminosity $\Delta V = V_{\rm HB} - V_*$, with $V_{\rm HB}$ from Table 4.1. If the Sills & Pinsonneault model is correct, then the faster-rotating stars should be brighter as well. No such relationship is evident.

7.2.3 Other possibilities

A remote alternative hypothesis is that the slow rotators are the 'normal' HB stars, and that the rapid rotators redwards of the gap represent the progeny of merged stars, perhaps a subpopulation of blue stragglers (BS), similar to the suggestion by Fusi Pecci *et al.* (1992)

that BS progeny populate the red HB. Such stellar merger products would likely retain excess angular momentum even through the HB stage, although the issue is complicated by other possible effects of mergers, including mass loss. It also seems unlikely that a merger product would evolve in such a similar fashion as a normal single star, to appear on the same HB locus. It might still be potentially worthwhile to undertake a numerical comparison of the B'_{fast} and blue straggler populations of these clusters, but such a study is beyond the scope of this project.

In a similar vein, some recent papers (Soker, 1998; Soker & Harpaz, 1999; Siess & Livio, 1999) propose that B'_{fast} stars spin up when they swallow close planetary companions during the red giant phase. Although a mechanism of this sort would certainly provide plenty of angular momentum for the B'_{fast} stars, it again seems that such a merger would cause noticeable deviations in a star's subsequent evolution. Furthermore, the presence of planetary companions around metal-poor stars is yet to be demonstrated — all of the exosolar planets found to date orbit stars with significantly *higher* metallicity than solar (Gonzalez & Laws, 2000) — so this seems an *ad hoc* means of explaining fast rotation and the second-parameter effect.

7.2.4 Implications for deep mixing

If BHB progenitor stars do indeed possess rapidly-rotating cores, this raises serious implications for the mixing of fusion-processed material from their cores to the envelope. A great deal of attention has focused recently on the photospheric abundances of RGB stars. Bimodalities appear in the distribution of oxygen (Kraft *et al.*, 1997) and CN (Ivans *et al.*, 1999) abundances, along with correlations between CNO elements and heavier metals like aluminum and magnesium which trace nucleosynthesis in the hydrogen-burning shell (Shetrone, 1996; Cavallo & Nagar, 2000). These distributions of $\log \epsilon$ in different elements suggest that some cluster giants undergo deep mixing, while others do not. If material is being exchanged between the core and the envelope of a star, then angular momentum may also be redistributed. This connection is entirely speculative at this point, but bears consideration by future modeling and observational programs.

Chapter 8 Conclusions and future directions

We summarize our observational results for the compositions and rotations of BHB stars, along with our preliminary conclusions regarding the causes and implications of these results. A great deal of continued work will be necessary before these issues are fully understood, and we offer some suggestions for future investigations.

8.1 Summary of results

We have performed detailed abundance analyses of BHB stars in six different metal-poor globular clusters. The cooler B′ stars, redwards of gap G1, show photospheric abundances which agree with the expected composition for each cluster, while the BT stars at higher $T_{\rm eff}$ exhibit remarkable enhancements of most metal species, and depletion of helium. These abundance variations are attributed to element diffusion — radiative levitation of the metals, gravitational settling of the helium — which occurs in the absence of convection or rotationally-driven circulation currents. Iron and titanium are enhanced by factors of 30 to 300, phosphorus and chromium by factors of 1000 to 3000, while calcium, sulphur, and other species are increased by lesser amounts, and magnesium and silicon are unchanged. Depletion of helium increases with greater $\log g$, up to 2.5 orders of magnitude. The metal enhancements appear to be capable of altering the flux distribution of these stars, thus causing photometric peculiarities in cluster CMDs such as gaps and overluminosities. Furthermore, our data provide a stringent test of theoretical models for the diffusion mechanisms, particularly the abundance behavior of each individual element and the influence of the initial metallicity of the star.

We also measure the projected rotation velocities of our sample set, and again find a significant difference between the B′ and BT stars. Among the cooler stars, we verify the fast population (30–40 $\mathrm{km\,s^{-1}}$) previously reported in the literature, and find similar bimodal velocity distributions in several new clusters. The hotter BT stars, however, are almost exclusively slow rotators, with $v \sin i < 8\,\mathrm{km\,s^{-1}}$. This dichotomy offers some new clues regarding the origin of the range of HB rotation rates, and the potential role of rotation

in explaining characteristics of RGB and HB stars.

8.2 Unresolved issues

Although we have uncovered some important and intriguing new aspects of HB stars and HB morphology, the second-parameter problem remains as inscrutable as before. Basic issues, such as how BT and EBT stars are produced, and why the B'_{fast} stars are rotating so quickly, remain unresolved. With the findings reported herein, however, we can identify some key intermediate questions, which can be answered via direct observational or theoretical programs, and which will lead us closer to an ultimate solution:

- *How much photospheric enhancement or depletion will a specific element show, given* $T_{\rm eff}$, $\log g$, *initial* [Fe/H], *and* $v_{\rm rot}$*?* Our abundance derivations provide a good initial indication of the effectiveness of the diffusion mechanisms under different conditions, but these trends need to be duplicated by models, and confronted with more abundance measurements over a larger volume of parameter space.

- *How will these metal enhancements and helium depletions change the spectral energy distribution emitted from the photosphere, and what impact will this have on the measured broadband colors?* The combination of more advanced diffusion models and more extensive measurements of BHB abundances will allow us to refine the atmosphere models, incorporating non-solar-scaled abundance patterns. We can then more accurately convert evolutionary models into isochrones for comparison to globular cluster CMDs, and better constrain both the models and the derived cluster parameters.

- *How closely connected are the slow BT rotation rates and the diffusion-driven abundance variations?* The data for M13 and M15, particularly the two metal-poor, $v_{\rm rot}^{\rm fast}$ BT stars in M15, are strongly suggestive regarding the link between rotation and diffusion, but again, a larger sample size would help solidify and refine this claim. In particular, we would like to (a) delineate the blueward extent of any such fast BT population, to see whether it could be considered a small extension of the fast B′ set, instead of a part of the BT proper, and (b) find the critical $v_{\rm rot}$ at which diffusion is prevented from altering the photospheric abundances.

- *Is the distribution of* B′ $v_{\rm rot}$ *truly bimodal, and if so, how do the values of* $v_{\rm rot}^{\rm fast}$ *and* $v_{\rm rot}^{\rm slow}$ *vary from cluster to cluster?* The currently-available data — Peterson *et al.* (1995) and this work — make a fairly convincing case for distinct fast and slow populations in M13, M15, M68, and M92, but the exact shape of the distributions could be more accurately determined with better $v \sin i$ values for the Peterson stars, and larger sample sizes. Some clusters, like M3 and NGC288, do not show an obvious $\mathrm{B}'_{\rm fast}$ element, but two separate populations may be lurking there, and will appear with $v \sin i$ errors of $\sim 0.5\,\mathrm{km\,s^{-1}}$ instead of $5\,\mathrm{km\,s^{-1}}$. There have also been suggestions that fast stellar rotation may be a function of the overall angular momentum of the parent globular cluster, or may result from close stellar encounters in the cores of the more concentrated clusters. With additional measurements of peak $v \sin i$ in other clusters (as well as in the very different dynamical environment of the metal-poor Galactic halo), we can perhaps identify which factor(s) regulate the $\mathrm{B}'_{\rm fast}$ population, and thus uncover the mechanism responsible.

8.3 Other HB stars in current GCs

Future observations of BHB stars could go in a variety of different directions, but continued study of the six clusters which we have already observed is certainly in order. Although we have a good handle on the rotation and abundance trends within each cluster, there are several clearly-defined holes in our coverage which need to be filled.

As mentioned in the laundry list in the previous section, we would like to put the bimodality of B′ rotation rates on a more solid statistical footing. The data set for M15 and M92 is large, but could be improved, especially since there are hints of trimodality in M92. Furthermore, M3, M13, and NGC288 have been well-sampled by Peterson *et al.* (1995), but their $v \sin i$ measurements have large error bars, which obscure important details of the velocity distribution.

The short blue tails of M68 and M92 should receive additional attention, because the few BT stars that we have observed in these clusters have been "anomalous," showing metal-poor cluster composition and faster rotation. If the short BTs are composed of a different category of star than the long BTs, then this would be a critical factor towards explaining the presence of BTs.

We also need to push our temperature coverage further in both directions. To the blue, it will be interesting to see whether the abundance anomalies persist past gap G3, or whether EBT stars show normal composition. We have recently received HST/STIS time to look at some of M13's EBT stars in the ultraviolet. The spectral resolution will not be sufficient to measure rotational broadening, but we will be able to determine the photospheric abundances under even more extreme conditions of flux and gravity. The cool RHB stars, on the other hand, are not expected to show any diffusion effects, since their atmospheres are fully convective, so with observations of some of these stars in each cluster, we can verify the cluster metallicities and evaluate rotation rate for stars that have undergone minimal mass loss.

8.4 Other globular clusters

Turning to BHB stars in other clusters, we should first study other "major" (*i.e.*, close and bright) metal-poor GCs, particularly those in the southern hemisphere which were not accessible from Keck. NGC 6752 is one obvious target, with a long blue tail and EBT with gaps, similar to M13. Metal enhancement and helium depletion have already been found in its BT stars, so we expect a similar transition to slow rotation as well. High-resolution observations of this cluster are being planned for the UVES spectrograph at the ESO VLT 8-meter facilities, and other programs are underway to make similar measurements of NGC6093 (M80) and the more metal-rich NGC6441.

It would also be useful to make measurements of other second-parameter pairs, similar to M3 versus M13, as we then reduce the number of free variables and stand a better chance of identifying relevant second parameters. NGC362 is often cited as a twin of NGC288, and is at a similar distance, so observations of some of its BHB stars would be eminently feasible. Other sets of twins, including clusters that have already been studied, can also be identified and pursued.

In an extreme case of the second-parameter effect, some metal-rich globulars are revealing small but unmistakable BTs and EBTs (Rich *et al.*, 1997; Moehler *et al.*, 1999a). Observations of these faint stars would be challenging, but it would be fascinating to determine the degree of similarity between these anomalous hot stars and our metal-enhanced, slow-rotating BT stars.

8.5 HB stars in the Galactic halo

BHB stars are found not only within globular clusters, but also in the field, in the metal-poor Galactic halo. These field horizontal-branch (FHB) stars offer an additional venue for studying the diffusion and rotation behavior, and are also useful as tracers of halo dynamics and formation history.

Since the halo population shows photometric gaps comparable to those in clusters, it appears likely that similar diffusion mechanisms are at work. A paucity of stars at $T_{\rm eff} \simeq 11000\,{\rm K}$ was detected in UBV photometry of high-latitude faint blue stars by Newell (1973) and subsequently confirmed by several other studies. Since this gap coincides with the position of G1 in globular clusters, it is tempting to assume that this component of the FHB morphology is due to the same onset of metal enhancements, but this claim needs to be tested.

If diffusion is indeed active in the hotter halo stars, then this provides us with the possibility of evaluating the effects of diffusion over a wide range of stellar metallicity. With a sufficiently large sample of bona fide FHB stars, we could chart the amplitude and $T_{\rm eff}$ dependence of the photospheric abundance variations over [Fe/H] $\simeq -2.5$ to 0.0. Such a sample would prove extremely useful for exploring the details of the diffusion mechanisms, and would allow theorists to fine-tune their models of element migration in stellar atmospheres. An obvious challenge in this effort, of course, is to accurately determine the "true" [Fe/H] of a star in the presence of these very same metal enhancements that we are trying to measure. Fortunately, the magnesium abundance appears to be immune to diffusion effects, as the [Mg/H] values that we measure for our BHB stars in M13 and M15 are effectively constant, even when the other metals are strongly enhanced. Since [Mg/H] behaves consistently in the globular cluster context, we can use it, with reasonable confidence, as an unbiased metallicity diagnostic in the halo.

We would also gain a new vantage point on the rotation issue. The literature reports measurements of $v \sin i$ rotation for only a handful of FHB stars (Peterson *et al.*, 1983), so it is unclear whether the field population exhibits the same B′/BT differences and B′ bimodality as the GC stars. The halo represents a very different dynamical environment from a globular cluster, and spans a much wider range of metallicity, so any differences in rotation signature between the halo and the cluster stars, or trends with [Fe/H] in the halo

stars, would provide important clues regarding the origins of the high-$v \sin i$ and low-$v \sin i$ populations.

Determining how the diffusion-driven abundance anomalies vary with other stellar parameters is important, not only for improving our fundamental understanding of BHB stellar atmospheres, but also because FHB stars are often used to map the formation of the Galactic halo. Schuster *et al.* (1993), for instance, use stellar metallicities derived from Strömgren photometry as a chronometer, assuming [Fe/H] increases monotonically with time as the halo becomes more metal-rich. Coupled with radial velocities and proper motions for each star, these observations demonstrate how the dispersion and rotation of the halo and thick disk evolve over time. However, any BHB stars in their sample which have metal-enhanced photospheres will exhibit misleadingly high Strömgren metal indices, and thus would be misclassified as being younger than they actually are. Their general conclusions are unlikely to change due to this contamination of their higher-metallicity bins, but some important details may require modification. By identifying and accounting for the possible influence of abundance anomalies in evolved stars, we gain a clearer view of the era of Galactic formation.

Appendix A Abundance results

Table A.1: Abundance results for program stars

star	species	$\log\epsilon$	[X/H]	σ_Σ	$N_{\rm lines}$	σ_N	σ_T	σ_g	σ_ξ	σ_W
M3/B125	He I	< 11.70	< +0.71							
	C I	< 8.78	< +0.26							
	C II	< 10.11	< +1.59							
	N I	< 8.64	< +0.72							
	O I	< 9.37	< +0.54							
	Mg I	6.45	−1.13	0.16	3	+0.14	+0.10	−0.02	−0.05	+0.08
	Mg II	6.04	−1.54	0.09	2	+0.06	+0.01	+0.00	−0.05	+0.05
	Al II	< 7.24	< +0.77							
	Si I	< 13.04	< +5.49							
	Si II	6.23	−1.32	0.19	3	+0.24	−0.02	+0.02	−0.01	+0.12
	S I	< 8.40	< +1.07							
	S II	< 8.78	< +1.45							
	Ca I	5.02	−1.34	0.17	1	+0.00	+0.14	−0.04	−0.02	+0.08
	Ca II	< 6.57	< +0.21							
	Sc II	1.87	−1.30	0.12	1	+0.00	+0.08	+0.00	−0.03	+0.08
	Ti I	< 6.01	< +0.99							
	Ti II	3.99	−1.03	0.09	12	+0.17	+0.06	+0.00	−0.04	+0.08
	V II	< 4.51	< +0.51							
	Cr I	< 5.45	< −0.22							
	Cr II	4.46	−1.21	0.09	1	+0.00	+0.04	+0.01	−0.02	+0.08
	Mn I	< 5.67	< +0.28							
	Mn II	< 5.95	< +0.56							
	Fe I	6.05	−1.45	0.14	9	+0.17	+0.11	−0.02	−0.03	+0.11
	Fe II	6.06	−1.44	0.08	19	+0.21	+0.04	+0.01	−0.05	+0.09
	Co I	< 6.46	< +1.54							
	Co II	< 6.05	< +1.13							
	Ni I	< 7.04	< +0.79							
	Ni II	< 5.70	< −0.55							
	Zn I	< 5.51	< +0.91							
	Sr II	< 1.62	< −1.35							
	Y II	< 2.24	< +0.00							
	Zr I	< 5.74	< +3.14							
	Zr II	2.26	−0.34	0.13	1	+0.00	+0.06	+0.01	−0.01	+0.12
	Ba II	< 1.97	< −0.16							
M3/B244	He I	11.20	+0.21	0.34	1	+0.00	−0.28	+0.04	−0.05	+0.18
	C I	< 8.98	< +0.46							
	C II	< 9.57	< +1.05							
	N I	< 8.77	< +0.85							
	O I	< 9.39	< +0.56							
	Mg I	< 6.52	< −1.06							
	Mg II	6.05	−1.53	0.20	2	+0.12	+0.02	+0.00	−0.14	+0.07
	Al II	< 7.42	< +0.95							
	Si I	< 13.33	< +5.78							
	Si II	< 6.95	< −0.60							
	S II	< 8.76	< +1.43							
	Ca I	< 5.80	< −0.56							
	Ca II	< 7.00	< +0.64							
	Sc II	< 2.23	< −0.94							
	Ti II	3.55	−1.47	0.35	2	+0.25	+0.20	+0.01	−0.03	+0.13
	V II	< 4.69	< +0.69							
	Cr I	< 5.94	< +0.27							
	Cr II	< 4.75	< −0.92							

star	species	log ϵ	[X/H]	σ_Σ	$N_{\rm lines}$	σ_N	σ_T	σ_g	σ_ξ	σ_W
M3/B244	Mn I	< 5.89	< +0.50							
cont.	Mn II	< 6.11	< +0.72							
	Fe I	< 6.40	< −1.10							
	Fe II	6.05	−1.45	0.28	7	+0.39	+0.11	+0.01	−0.19	+0.20
	Co II	< 6.36	< +1.44							
	Ni I	< 7.33	< +1.08							
	Ni II	< 5.68	< −0.57							
	Zn I	< 6.30	< +1.70							
	Sr II	< 2.11	< −0.86							
	Y II	< 2.51	< +0.27							
	Zr II	< 3.23	< +0.63							
	Ba II	< 2.83	< +0.70							
M3/B445	He I	10.99	+0.00	0.41	1	+0.00	−0.36	+0.03	−0.05	+0.18
	C I	< 9.67	< +1.15							
	C II	< 9.40	< +0.88							
	N I	< 9.72	< +1.80							
	N II	< 11.22	< +3.30							
	O I	< 9.10	< +0.27							
	Na I	< 6.93	< +0.60							
	Mg I	< 7.44	< −0.14							
	Mg II	6.15	−1.43	0.20	2	+0.01	+0.04	+0.00	−0.15	+0.12
	Al I	< 9.28	< +2.81							
	Al II	< 7.31	< +0.84							
	Si I	< 10.49	< +2.94							
	Si II	< 6.83	< −0.72							
	S II	< 8.61	< +1.28							
	Ca I	< 8.08	< +1.72							
	Ca II	< 5.58	< −0.78							
	Sc II	< 3.67	< +0.50							
	Ti II	< 4.96	< −0.06							
	V II	< 6.75	< +2.75							
	Cr II	< 5.77	< +0.10							
	Mn II	< 6.70	< +1.31							
	Fe I	< 8.15	< +0.65							
	Fe II	< 6.51	< −0.99							
	Fe III	< 10.17	< +2.67							
	Ni II	< 7.94	< +1.69							
	Sr II	< 4.63	< +1.66							
M3/B518	He I	< 12.35	< +1.36							
	C I	< 8.34	< −0.18							
	C II	< 9.99	< +1.47							
	N I	< 8.93	< +1.01							
	O I	< 8.70	< −0.13							
	Na I	< 6.42	< +0.09							
	Mg I	6.35	−1.23	0.22	4	+0.28	+0.11	−0.02	−0.09	+0.06
	Mg II	6.05	−1.53	0.12	2	+0.09	+0.00	+0.01	−0.06	+0.06
	Al I	4.84	−1.63	0.17	1	+0.00	+0.11	−0.02	−0.04	+0.12
	Al II	< 7.59	< +1.12							
	Si I	< 8.29	< +0.74							
	Si II	< 6.89	< −0.66							
	S I	< 7.92	< +0.59							
	Ca I	4.55	−1.81	0.18	1	+0.00	+0.15	−0.02	−0.05	+0.08
	Ca II	< 4.62	< −1.74							
	Sc II	1.52	−1.65	0.12	1	+0.00	+0.08	+0.01	−0.04	+0.08
	Ti I	< 5.38	< +0.36							
	Ti II	3.66	−1.36	0.09	19	+0.17	+0.07	+0.02	−0.04	+0.08
	V I	< 5.41	< +1.41							
	V II	< 4.38	< +0.38							
	Cr I	< 5.06	< −0.61							
	Cr II	4.34	−1.33	0.12	4	+0.17	+0.05	+0.01	−0.02	+0.07
	Mn I	< 5.36	< −0.03							
	Mn II	< 5.75	< +0.36							
	Fe I	5.76	−1.74	0.16	11	+0.19	+0.13	−0.02	−0.05	+0.09
	Fe II	5.82	−1.68	0.10	17	+0.16	+0.06	+0.02	−0.07	+0.08

star	species	log ϵ	[X/H]	σ_Σ	$N_{\rm lines}$	σ_N	σ_T	σ_g	σ_ξ	σ_W
M3/B518	Co I	< 6.01	< +1.09							
cont.	Co II	< 6.31	< +1.39							
	Ni I	< 5.98	< −0.27							
	Ni II	< 6.02	< −0.23							
	Zn I	< 4.94	< +0.34							
	Sr II	< 1.72	< −1.25							
	Y II	< 1.89	< −0.35							
	Zr I	< 4.83	< +2.23							
	Zr II	3.46	+0.86	0.11	1	+0.00	+0.07	+0.01	−0.02	+0.08
	Ba II	< 1.39	< −0.74							
	La II	< 2.85	< +1.68							
	Ce II	< 3.07	< +1.49							
	Nd II	< 3.01	< +1.51							
	Eu II	< 1.66	< +1.15							
M3/B831	He I	< 11.42	< +0.43							
	C I	< 8.55	< +0.03							
	C II	< 9.60	< +1.08							
	N I	< 8.62	< +0.70							
	O I	< 9.24	< +0.41							
	Mg I	6.37	−1.21	0.21	3	+0.24	+0.11	−0.03	−0.03	+0.05
	Mg II	6.17	−1.41	0.09	2	+0.06	+0.01	+0.00	−0.06	+0.04
	Al II	< 7.08	< +0.61							
	Si I	< 13.06	< +5.51							
	Si II	6.48	−1.07	0.09	1	+0.00	−0.02	+0.02	−0.03	+0.08
	S II	< 9.02	< +1.69							
	Ca I	< 5.40	< −0.96							
	Ca II	< 6.53	< +0.17							
	Sc II	< 1.96	< −1.21							
	Ti I	< 6.13	< +1.11							
	Ti II	3.79	−1.23	0.09	13	+0.14	+0.07	+0.01	−0.02	+0.07
	V II	< 4.69	< +0.69							
	Cr I	< 5.41	< −0.26							
	Cr II	4.42	−1.25	0.09	1	+0.00	+0.04	+0.01	−0.02	+0.08
	Mn I	< 5.60	< +0.21							
	Mn II	< 6.02	< +0.63							
	Fe I	5.95	−1.55	0.14	5	+0.08	+0.12	−0.03	−0.03	+0.07
	Fe II	5.94	−1.56	0.08	22	+0.18	+0.05	+0.01	−0.04	+0.09
	Co I	< 6.33	< +1.41							
	Co II	< 5.82	< +0.90							
	Ni I	< 7.02	< +0.77							
	Ni II	< 5.54	< −0.71							
	Zn I	< 5.63	< +1.03							
	Sr II	< 1.86	< −1.11							
	Y II	< 2.41	< +0.17							
	Zr II	< 3.11	< +0.51							
	Ba II	< 1.99	< −0.14							
M3/B1241	He I	11.07	+0.08	0.29	1	+0.00	−0.17	+0.03	−0.02	+0.23
	C I	< 9.02	< +0.50							
	C II	< 10.16	< +1.64							
	N I	< 9.17	< +1.25							
	O I	< 8.92	< +0.09							
	Na I	< 6.01	< −0.32							
	Mg I	6.26	−1.32	0.22	2	+0.04	+0.18	−0.03	−0.06	+0.09
	Mg II	6.21	−1.37	0.21	2	+0.17	+0.02	−0.01	−0.09	+0.08
	Al I	< 8.38	< +1.91							
	Al II	< 7.98	< +1.51							
	Si I	< 9.24	< +1.69							
	Si II	6.29	−1.26	0.18	1	+0.00	−0.04	+0.02	−0.03	+0.17
	S I	< 8.88	< +1.55							
	S II	< 9.18	< +1.85							
	Ca I	< 7.16	< +0.80							
	Ca II	3.99	−2.37	0.32	2	+0.14	+0.20	−0.04	−0.17	+0.12
	Sc II	< 2.86	< −0.31							
	Ti I	< 6.67	< +1.65							

star	species	log ϵ	[X/H]	σ_Σ	$N_{\rm lines}$	σ_N	σ_T	σ_g	σ_ξ	σ_W
M3/B1241	Ti II	3.96	−1.06	0.18	6	+0.22	+0.12	+0.01	−0.06	+0.14
cont.	V I	6.29	+2.29	0.26	1	+0.00	+0.20	−0.03	−0.01	+0.17
	V II	< 5.29	< +1.29							
	Cr I	< 6.32	< +0.65							
	Cr II	< 5.37	< −0.30							
	Mn I	< 6.59	< +1.20							
	Mn II	< 6.52	< +1.13							
	Fe I	6.06	−1.44	0.29	2	+0.13	+0.20	−0.03	−0.07	+0.15
	Fe II	6.05	−1.45	0.19	11	+0.28	+0.09	+0.01	−0.14	+0.14
	Co I	< 8.40	< +3.48							
	Co II	< 7.56	< +2.64							
	Ni I	< 7.19	< +0.94							
	Ni II	< 7.34	< +1.09							
	Zn I	< 5.95	< +1.35							
	Sr II	< 3.28	< +0.31							
	Y II	< 3.43	< +1.19							
	Zr II	< 4.79	< +2.19							
	Ba II	< 3.07	< +0.94							
M13/IV-83	He I	< 11.33	< +0.34							
	C I	< 8.14	< −0.38							
	C II	< 9.43	< +0.91							
	N I	< 8.33	< +0.41							
	O I	< 9.06	< +0.23							
	Mg I	6.48	−1.10	0.26	2	+0.19	+0.15	−0.02	−0.08	+0.06
	Mg II	6.08	−1.50	0.07	1	+0.00	+0.01	+0.01	−0.05	+0.04
	Al I	< 8.27	< +1.80							
	Al II	< 7.12	< +0.65							
	Si I	< 12.45	< +4.90							
	Si II	< 6.27	< −1.28							
	S I	< 7.80	< +0.47							
	Ca I	4.80	−1.57	0.22	2	+0.08	+0.18	−0.03	−0.06	+0.08
	Ca II	< 5.27	< −1.09							
	Sc II	1.73	−1.44	0.14	1	+0.00	+0.10	+0.01	−0.06	+0.07
	Ti I	< 5.16	< +0.14							
	Ti II	3.97	−1.05	0.13	11	+0.13	+0.09	+0.01	−0.08	+0.07
	V I	< 4.85	< +0.85							
	V II	< 3.38	< −0.62							
	Cr I	< 4.60	< −1.07							
	Cr II	< 4.08	< −1.59							
	Mn I	< 4.40	< −0.99							
	Mn II	< 4.74	< −0.65							
	Fe I	6.04	−1.46	0.19	9	+0.11	+0.16	−0.02	−0.08	+0.09
	Fe II	6.05	−1.45	0.18	10	+0.24	+0.08	+0.02	−0.14	+0.09
	Co I	< 5.11	< +0.19							
	Co II	< 5.52	< +0.60							
	Ni I	< 7.20	< +0.95							
	Ni II	< 4.90	< −1.35							
	Zn I	< 4.74	< +0.14							
	Sr II	1.02	−1.95	0.24	3	+0.23	+0.15	+0.00	−0.05	+0.11
	Y I	< 4.64	< +2.40							
	Y II	< 1.58	< −0.66							
	Zr I	< 4.73	< +2.13							
	Zr II	< 2.14	< −0.46							
	Ba II	< 1.06	< −1.07							
	La II	< 1.75	< +0.58							
	Ce II	< 2.50	< +0.92							
	Nd II	< 2.38	< +0.88							
	Eu II	< 1.26	< +0.75							
M13/J11	He I	< 12.55	< +1.56							
	C I	< 7.65	< −0.87							
	C II	< 10.25	< +1.73							
	N I	< 8.32	< +0.40							
	O I	< 9.18	< +0.35							
	Mg I	6.25	−1.33	0.16	3	+0.18	+0.07	−0.01	−0.06	+0.05

star	species	log ϵ	[X/H]	σ_Σ	$N_{\rm lines}$	σ_N	σ_T	σ_g	σ_ξ	σ_W
M13/J11	Mg II	5.92	−1.66	0.04	1	+0.00	−0.01	+0.02	−0.01	+0.03
cont.	Al I	4.10	−2.37	0.11	1	+0.00	+0.09	−0.01	−0.01	+0.06
	Al II	< 7.05	< +0.58							
	Si I	< 8.75	< +1.20							
	Si II	< 6.64	< −0.91							
	S I	< 7.27	< −0.06							
	Ca I	4.55	−1.81	0.11	1	+0.00	+0.08	−0.01	−0.05	+0.06
	Ca II	< 4.72	< −1.64							
	Sc I	< 3.94	< +0.77							
	Sc II	1.54	−1.63	0.10	4	+0.10	+0.07	+0.03	−0.01	+0.06
	Ti I	< 4.44	< −0.58							
	Ti II	3.70	−1.32	0.06	22	+0.14	+0.04	+0.02	−0.02	+0.05
	V I	< 4.08	< +0.08							
	V II	< 3.01	< −0.99							
	Cr I	3.84	−1.83	0.11	1	+0.00	+0.09	+0.00	+0.00	+0.06
	Cr II	4.08	−1.59	0.06	2	+0.00	+0.02	+0.02	−0.00	+0.05
	Mn I	< 3.76	< −1.63							
	Mn II	< 4.60	< −0.79							
	Fe I	5.68	−1.82	0.10	15	+0.15	+0.08	−0.00	−0.03	+0.06
	Fe II	5.68	−1.82	0.06	20	+0.17	+0.03	+0.02	−0.02	+0.05
	Co I	< 4.31	< −0.61							
	Co II	< 5.35	< +0.43							
	Ni I	< 6.48	< +0.23							
	Ni II	< 4.85	< −1.40							
	Zn I	< 4.19	< −0.41							
	Sr II	0.94	−2.03	0.10	3	+0.07	+0.06	+0.02	−0.04	+0.05
	Y II	< 1.27	< −0.97							
	Zr II	< 1.92	< −0.68							
	Ba II	0.45	−1.68	0.10	1	+0.00	+0.08	+0.01	+0.00	+0.06
	La II	< 1.08	< −0.09							
	Ce II	2.04	+0.46	0.17	1	+0.00	+0.11	+0.01	+0.00	+0.13
	Nd II	< 1.51	< +0.01							
	Eu II	< 0.58	< +0.07							
M13/SA113	He I	10.99	+0.00	0.15	1	+0.00	−0.09	+0.03	−0.03	+0.11
	C I	< 9.47	< +0.95							
	C II	< 9.35	< +0.83							
	N I	< 8.84	< +0.92							
	O I	< 9.45	< +0.62							
	Mg I	< 7.10	< −0.48							
	Mg II	6.04	−1.54	0.14	2	+0.04	+0.00	−0.01	−0.12	+0.06
	Al I	< 6.38	< −0.09							
	Al II	< 7.04	< +0.57							
	Si II	6.10	−1.45	0.11	3	+0.08	−0.03	+0.02	−0.06	+0.09
	S II	< 8.55	< +1.22							
	Ca I	< 6.97	< +0.61							
	Ca II	< 6.76	< +0.40							
	Sc II	< 2.92	< −0.25							
	Ti II	< 4.39	< −0.63							
	V II	< 4.69	< +0.69							
	Cr I	< 6.74	< +1.07							
	Cr II	< 5.14	< −0.53							
	Mn I	< 6.76	< +1.37							
	Mn II	< 6.55	< +1.16							
	Fe I	< 7.21	< −0.29							
	Fe II	5.88	−1.62	0.20	5	+0.18	+0.02	+0.01	−0.17	+0.08
	Ni II	< 5.73	< −0.52							
	Sr II	< 2.99	< +0.02							
	Y II	< 3.60	< +1.36							
	Zr II	< 3.90	< +1.30							
	Ba II	< 3.82	< +1.69							
M13/SA404	He I	11.18	+0.19	0.14	1	+0.00	−0.09	+0.02	−0.01	+0.10
	C I	< 9.31	< +0.79							
	C II	< 9.12	< +0.60							
	N I	< 8.69	< +0.77							

star	species	log ϵ	[X/H]	σ_Σ	$N_{\rm lines}$	σ_N	σ_T	σ_g	σ_ξ	σ_W
M13/SA404	O I	< 9.36	< +0.53							
cont.	Mg I	< 7.03	< −0.55							
	Mg II	6.02	−1.56	0.15	2	+0.13	+0.00	−0.01	−0.06	+0.04
	Al I	< 6.08	< −0.39							
	Al II	< 7.12	< +0.65							
	Si II	6.07	−1.48	0.11	4	+0.16	−0.03	+0.02	−0.02	+0.09
	S II	< 8.62	< +1.29							
	Ca I	< 6.23	< −0.13							
	Ca II	< 6.49	< +0.13							
	Sc II	< 2.64	< −0.53							
	Ti II	< 4.21	< −0.81							
	V II	< 4.52	< +0.52							
	Cr I	< 6.42	< +0.75							
	Cr II	< 4.82	< −0.85							
	Mn I	< 6.43	< +1.04							
	Mn II	< 6.23	< +0.84							
	Fe I	< 6.72	< −0.78							
	Fe II	5.56	−1.94	0.07	5	+0.06	+0.02	+0.01	−0.05	+0.07
	Ni II	< 5.73	< −0.52							
	Sr II	< 2.51	< −0.46							
	Y II	< 3.14	< +0.90							
	Zr II	< 3.46	< +0.86							
	Ba II	< 3.30	< +1.17							
M13/WF2-820	He I	9.99	−0.99	0.31	2	+0.19	−0.12	+0.03	−0.01	+0.21
	C I	< 9.91	< +1.39							
	C II	7.83	−0.69	0.13	1	+0.00	−0.09	+0.03	−0.02	+0.08
	N I	< 9.30	< +1.38							
	N II	< 9.16	< +1.24							
	O I	< 9.85	< +1.02							
	O II	< 10.58	< +1.75							
	Mg I	< 9.14	< +1.56							
	Mg II	< 7.40	< −0.18							
	Al I	< 10.03	< +3.56							
	Al II	< 6.66	< +0.19							
	Al III	< 8.20	< +1.73							
	Si I	< 10.01	< +2.46							
	Si II	< 7.03	< −0.52							
	Si III	< 8.75	< +1.20							
	P I	< 9.75	< +4.30							
	P II	7.02	+1.57	0.11	4	+0.14	−0.03	+0.02	−0.04	+0.09
	P III	< 8.48	< +3.03							
	S I	< 10.05	< +2.72							
	S II	< 7.65	< +0.32							
	S III	< 9.84	< +2.51							
	Ca I	< 9.58	< +3.22							
	Ca II	< 6.91	< +0.55							
	Sc II	4.40	+1.23	0.25	1	+0.00	+0.12	−0.01	−0.01	+0.22
	Sc III	< 7.04	< +3.87							
	Ti II	5.03	+0.01	0.16	2	+0.04	+0.12	−0.01	−0.02	+0.10
	Ti III	< 8.34	< +3.32							
	V I	< 9.17	< +5.17							
	V II	6.24	+2.24	0.14	1	+0.00	+0.10	−0.01	−0.02	+0.09
	V III	< 8.21	< +4.21							
	Cr II	5.26	−0.41	0.13	1	+0.00	+0.10	+0.00	−0.02	+0.08
	Cr III	< 8.93	< +3.26							
	Mn I	< 8.56	< +3.17							
	Mn II	7.21	+1.82	0.15	12	+0.40	+0.08	+0.00	−0.03	+0.10
	Mn III	< 9.37	< +3.98							
	Fe I	8.46	+0.96	0.21	4	+0.03	+0.19	−0.03	−0.05	+0.11
	Fe II	7.74	+0.24	0.10	32	+0.33	+0.06	+0.01	−0.04	+0.10
	Fe I	8.23	+0.73	0.17	1	+0.00	−0.07	+0.04	−0.05	+0.14
	Co II	< 6.86	< +1.94							
	Ni I	< 9.67	< +3.42							
	Ni II	7.40	+1.15	0.14	1	+0.00	−0.01	+0.00	−0.04	+0.13
	Ni III	< 10.75	< +4.50							
	Zn I	< 7.45	< +2.85							

star	species	log ϵ	[X/H]	σ_Σ	$N_{\rm lines}$	σ_N	σ_T	σ_g	σ_ξ	σ_W
M13/WF2-820	Sr II	< 4.73	< +1.76							
cont	Y II	< 5.25	< +3.01							
	Zr II	< 4.72	< +2.12							
	Ba II	< 4.88	< +2.75							
M13/WF2-2541	He I	9.70	−1.28	0.12	2	+0.01	−0.07	+0.02	−0.02	+0.09
	C I	< 10.03	< +1.51							
	C II	< 8.02	< −0.50							
	N I	< 9.75	< +1.83							
	N II	< 8.86	< +0.94							
	O I	< 9.10	< +0.27							
	O II	< 9.89	< +1.06							
	Na I	< 8.44	< +2.11							
	Mg II	6.01	−1.57	0.19	2	+0.16	+0.03	−0.01	−0.02	+0.10
	Al I	< 9.54	< +3.07							
	Al II	< 6.69	< +0.22							
	Al III	< 7.44	< +0.97							
	Si II	6.05	−1.50	0.16	3	+0.20	+0.02	+0.01	−0.01	+0.09
	Si III	< 8.63	< +1.08							
	P II	6.84	+1.39	0.09	12	+0.27	−0.02	+0.02	−0.03	+0.08
	P III	< 7.86	< +2.41							
	S II	< 7.22	< −0.11							
	S III	< 9.37	< +2.04							
	Ca II	5.38	−0.98	0.22	2	+0.00	+0.07	−0.02	−0.16	+0.14
	Sc II	< 5.47	< +2.30							
	Ti II	< 6.23	< +1.21							
	Ti III	< 8.86	< +3.84							
	V II	< 6.99	< +2.99							
	Cr II	< 6.61	< +0.94							
	Cr III	< 9.69	< +4.02							
	Mn II	< 6.87	< +1.48							
	Fe I	< 9.59	< +2.09							
	Fe II	7.45	−0.05	0.08	39	+0.25	+0.06	+0.00	−0.03	+0.08
	Fe I	7.74	+0.24	0.14	2	+0.06	−0.05	+0.04	−0.04	+0.10
	Co II	< 7.19	< +2.27							
	Ni II	< 7.24	< +0.99							
	Sr II	< 5.33	< +2.36							
	Y II	4.66	+2.42	0.13	1	+0.00	+0.08	−0.01	−0.01	+0.10
	Zr II	< 6.16	< +3.56							
	Ba II	< 5.23	< +3.10							
M13/WF2-2692	He I	9.29	−1.70	0.27	1	+0.00	−0.14	+0.03	−0.10	+0.20
	C I	< 10.43	< +1.91							
	C II	< 7.66	< −0.86							
	N I	< 10.06	< +2.14							
	N II	8.84	+0.92	0.29	1	+0.00	−0.10	+0.04	−0.18	+0.20
	N III	< 14.93	< +7.01							
	O I	< 9.21	< +0.38							
	O II	< 9.79	< +0.96							
	Na I	< 8.79	< +2.46							
	Mg II	6.10	−1.48	0.12	3	+0.07	+0.07	−0.01	−0.06	+0.09
	Al I	< 10.40	< +3.93							
	Al II	< 6.94	< +0.47							
	Al III	< 7.54	< +1.07							
	Si II	6.72	−0.83	0.13	1	+0.00	+0.05	+0.00	−0.06	+0.11
	Si III	< 8.49	< +0.94							
	P II	7.07	+1.62	0.13	9	+0.25	−0.01	+0.01	−0.09	+0.11
	P III	< 7.78	< +2.33							
	S I	< 10.86	< +3.53							
	S II	< 7.53	< +0.20							
	S III	< 9.39	< +2.06							
	Ca II	6.22	−0.14	0.55	1	+0.00	+0.14	−0.03	−0.50	+0.17
	Sc II	< 5.87	< +2.70							
	Sc III	< 7.17	< +4.00							
	Ti II	5.98	+0.96	0.21	1	+0.00	+0.15	−0.01	−0.02	+0.14
	Ti III	< 8.66	< +3.64							

star	species	$\log \epsilon$	[X/H]	σ_Σ	$N_{\rm lines}$	σ_N	σ_T	σ_g	σ_ξ	σ_W
M13/WF2-2692	V II	< 7.76	$< +3.76$							
cont.	Cr II	< 7.13	$< +1.46$							
	Mn II	< 7.22	$< +1.83$							
	Mn III	< 9.58	$< +4.19$							
	Fe I	9.64	$+2.14$	0.38	1	$+0.00$	$+0.28$	-0.04	-0.14	$+0.22$
	Fe II	8.06	$+0.56$	0.14	41	$+0.32$	$+0.10$	-0.00	-0.08	$+0.11$
	Fe I	7.98	$+0.48$	0.37	2	$+0.17$	-0.08	$+0.03$	-0.11	$+0.30$
	Co II	< 7.93	$< +3.01$							
	Ni II	< 7.60	$< +1.35$							
	Sr II	< 5.97	$< +3.00$							
	Y II	< 6.19	$< +3.95$							
	Zr II	< 6.15	$< +3.55$							
	Ba II	< 6.14	$< +4.01$							
M13/WF2-3035	He I	< 11.69	$< +0.70$							
	C I	< 8.16	< -0.36							
	C II	< 9.61	$< +1.09$							
	N I	< 8.51	$< +0.59$							
	O I	< 8.43	< -0.40							
	Na I	< 6.56	$< +0.23$							
	Mg I	6.11	-1.47	0.13	2	$+0.08$	$+0.07$	-0.03	-0.05	$+0.05$
	Mg II	6.10	-1.48	0.08	2	$+0.06$	$+0.00$	$+0.00$	-0.04	$+0.04$
	Al I	< 5.38	< -1.09							
	Al II	< 6.92	$< +0.45$							
	Si I	< 6.49	< -1.06							
	Si II	6.14	-1.41	0.09	1	$+0.00$	-0.01	$+0.02$	-0.01	$+0.09$
	S I	< 8.18	$< +0.85$							
	Ca I	< 4.96	< -1.40							
	Ca II	3.72	-2.64	0.12	1	$+0.00$	$+0.08$	-0.03	-0.08	$+0.04$
	Sc II	< 1.77	< -1.40							
	Ti I	< 5.46	$< +0.44$							
	Ti II	3.42	-1.60	0.11	7	$+0.22$	$+0.05$	$+0.01$	-0.02	$+0.07$
	V II	< 3.52	< -0.48							
	Cr I	< 5.05	< -0.62							
	Cr II	< 4.43	< -1.24							
	Mn I	< 5.15	< -0.24							
	Mn II	< 5.75	$< +0.36$							
	Fe I	5.60	-1.90	0.12	3	$+0.06$	$+0.09$	-0.02	-0.03	$+0.08$
	Fe II	5.78	-1.72	0.09	10	$+0.15$	$+0.04$	$+0.01$	-0.06	$+0.07$
	Co I	< 5.82	$< +0.90$							
	Co II	< 5.88	$< +0.96$							
	Ni I	< 6.31	$< +0.06$							
	Ni II	< 5.37	< -0.88							
	Zn I	< 4.97	$< +0.37$							
	Sr II	< 1.39	< -1.58							
	Y II	< 1.75	< -0.49							
	Zr II	< 2.70	$< +0.10$							
	Ba II	< 1.38	< -0.75							
	La II	< 2.90	$< +1.73$							
M13/WF2-3123	He I	8.41	-2.58	0.13	1	$+0.00$	-0.03	$+0.02$	-0.08	$+0.09$
	C II	< 7.09	< -1.43							
	C III	< 9.95	$< +1.43$							
	N I	< 10.26	$< +2.34$							
	N II	< 8.05	$< +0.13$							
	N III	< 11.39	$< +3.47$							
	O I	< 11.09	$< +2.26$							
	O II	< 8.56	< -0.27							
	O III	< 14.15	$< +5.32$							
	Na I	< 8.80	$< +2.47$							
	Mg I	< -1.57	< -9.15							
	Mg II	6.41	-1.17	0.08	1	$+0.00$	$+0.04$	-0.01	-0.02	$+0.06$
	Al I	< 11.80	$< +5.33$							
	Al II	< 7.39	$< +0.92$							
	Al III	< 6.54	$< +0.07$							
	Si II	6.77	-0.78	0.13	4	$+0.16$	$+0.05$	-0.01	-0.04	$+0.11$

star	species	log ϵ	[X/H]	σ_Σ	$N_{\rm lines}$	σ_N	σ_T	σ_g	σ_ξ	σ_W
M13/WF2-3123	Si III	< 7.55	< +0.00							
cont.	Si III	< 9.86	< +2.31							
	P II	6.75	+1.30	0.13	4	+0.19	+0.04	+0.00	−0.03	+0.10
	P III	< 7.16	< +1.71							
	S II	< 6.90	< −0.43							
	S III	< 8.27	< +0.94							
	Ca II	6.25	−0.11	0.36	1	+0.00	+0.08	−0.03	−0.34	+0.10
	Sc II	< 6.72	< +3.55							
	Sc III	< 6.49	< +3.32							
	Ti II	< 7.61	< +2.59							
	Ti III	< 7.67	< +2.65							
	V II	< 8.42	< +4.42							
	V III	< 8.57	< +4.57							
	Cr II	< 8.06	< +2.39							
	Cr III	< 8.92	< +3.25							
	Mn II	< 7.65	< +2.26							
	Mn III	< 8.96	< +3.57							
	Fe II	8.50	+1.00	0.21	9	+0.25	+0.10	−0.01	−0.16	+0.12
	Fe I	7.93	+0.43	0.18	1	+0.00	−0.04	+0.04	−0.12	+0.12
	Co II	< 8.69	< +3.77							
	Co III	< 9.29	< +4.37							
	Ni II	7.32	+1.07	0.23	1	+0.00	+0.10	−0.01	−0.09	+0.19
	Ni III	< 9.11	< +2.86							
	Zn III	< 8.72	< +4.12							
	Sr II	< 6.62	< +3.65							
	Ba II	< 6.94	< +4.81							
M13/WF3-548	He I	8.82	−2.17	0.12	1	+0.00	−0.05	+0.02	+0.00	+0.11
	C II	< 7.33	< −1.19							
	N I	< 9.90	< +1.98							
	N II	< 8.34	< +0.42							
	N III	< 14.18	< +6.26							
	O I	< 10.49	< +1.66							
	O II	< 9.59	< +0.76							
	Mg II	6.34	−1.24	0.18	2	+0.13	+0.03	−0.02	−0.02	+0.11
	Al I	< 9.45	< +2.98							
	Al II	< 7.07	< +0.60							
	Al III	< 7.07	< +0.60							
	Si II	6.49	−1.06	0.09	4	+0.12	+0.03	−0.01	−0.01	+0.09
	Si III	< 7.87	< +0.32							
	P II	< 6.95	< +1.50							
	P III	< 7.16	< +1.71							
	S II	< 7.20	< −0.13							
	S III	< 8.61	< +1.28							
	Ca II	5.75	−0.61	0.14	1	+0.00	+0.06	−0.02	−0.09	+0.08
	Sc II	< 5.31	< +2.14							
	Sc III	< 6.32	< +3.15							
	Ti II	< 6.98	< +1.96							
	Ti III	< 7.92	< +2.90							
	V II	7.19	+3.19	0.15	1	+0.00	+0.07	−0.01	−0.01	+0.13
	V III	< 8.14	< +4.14							
	Cr II	< 6.96	< +1.29							
	Cr III	< 8.59	< +2.92							
	Mn II	< 7.74	< +2.35							
	Mn III	< 9.08	< +3.69							
	Fe I	< 10.78	< +3.28							
	Fe II	7.93	+0.43	0.10	18	+0.16	+0.07	−0.01	−0.05	+0.11
	Fe III	< 8.62	< +1.12							
	Co II	< 7.65	< +2.73							
	Ni II	< 7.47	< +1.22							
	Ni III	< 9.82	< +3.57							
	Sr II	< 5.76	< +2.79							
M13/WF3-1718	He I	< 10.18	< −0.81							
	O I	< 9.67	< +0.84							
	O II	< 11.21	< +2.38							

star	species	log ϵ	[X/H]	σ_Σ	$N_{\rm lines}$	σ_N	σ_T	σ_g	σ_ξ	σ_W
M13/WF3-1718	Na I	< 7.99	< +1.66							
cont.	Mg I	< 7.54	< −0.04							
	Mg II	6.03	−1.55	0.08	2	+0.06	+0.02	−0.01	−0.01	+0.05
	Al I	< 7.57	< +1.10							
	Al II	< 6.41	< −0.06							
	Al III	< 8.97	< +2.50							
	Si I	< 10.61	< +3.06							
	Si II	5.44	−2.11	0.13	1	+0.00	−0.01	+0.02	+0.00	+0.11
	P I	< 9.23	< +3.78							
	P II	6.60	+1.15	0.11	6	+0.16	−0.04	+0.03	−0.01	+0.11
	P III	< 8.98	< +3.53							
	S I	< 9.72	< +2.39							
	S II	< 7.73	< +0.40							
	S III	< 10.97	< +3.64							
	Ca I	< 8.62	< +2.26							
	Ca II	5.18	−1.18	0.12	1	+0.00	+0.08	−0.03	−0.02	+0.07
	Sc II	< 3.44	< +0.27							
	Ti II	5.15	+0.13	0.09	26	+0.15	+0.07	−0.00	−0.01	+0.09
	V I	< 8.17	< +4.17							
	V II	6.42	+2.42	0.12	1	+0.00	+0.06	+0.00	+0.00	+0.10
	V III	< 8.84	< +4.84							
	Cr I	< 7.65	< +1.98							
	Cr II	5.24	−0.43	0.10	6	+0.20	+0.03	+0.01	−0.00	+0.08
	Mn I	< 8.04	< +2.65							
	Mn II	6.62	+1.23	0.08	31	+0.27	+0.02	+0.01	−0.01	+0.09
	Mn III	< 10.00	< +4.61							
	Fe I	7.65	+0.15	0.10	11	+0.13	+0.08	−0.02	−0.00	+0.09
	Fe II	7.60	+0.10	0.04	151	+0.24	+0.01	+0.01	−0.02	+0.09
	Fe III	< 9.30	< +1.80							
	Co I	< 8.27	< +3.35							
	Co II	6.23	+1.31	0.20	1	+0.00	+0.03	+0.03	+0.00	+0.19
	Co III	< 10.88	< +5.96							
	Ni II	5.03	−1.22	0.16	1	+0.00	+0.07	+0.03	+0.00	+0.14
	Zn I	< 7.00	< +2.40							
	Sr II	< 4.28	< +1.31							
	Y II	4.47	+2.23	0.15	11	+0.19	+0.08	−0.01	+0.10	+0.14
	Zr II	< 4.38	< +1.78							
	Ba II	< 4.53	< +2.40							
M13/WF4-3085	He I	9.43	−1.56	0.22	1	+0.00	−0.10	+0.02	−0.02	+0.08
	C I	< 10.18	< +1.66							
	C II	< 7.97	< −0.55							
	N I	< 9.56	< +1.64							
	N II	< 8.94	< +1.02							
	O I	< 9.95	< +1.12							
	O II	< 9.97	< +1.14							
	Mg I	< 9.32	< +1.74							
	Mg II	5.98	−1.60	0.22	2	+0.19	+0.05	−0.01	+0.00	+0.09
	Al I	< 8.00	< +1.53							
	Al II	< 6.42	< −0.05							
	Al III	< 7.64	< +1.17							
	Si I	< 10.98	< +3.43							
	Si II	6.92	−0.63	0.10	5	+0.18	+0.02	−0.00	−0.01	+0.06
	Si III	< 8.68	< +1.13							
	P I	< 10.11	< +4.66							
	P II	7.22	+1.77	0.07	17	+0.12	−0.03	+0.01	−0.01	+0.08
	P I	7.19	+1.74	0.33	2	+0.19	−0.11	+0.04	−0.02	+0.13
	S I	< 10.45	< +3.12							
	S II	< 7.59	< +0.26							
	S III	< 9.32	< +1.99							
	Ca I	< 10.12	< +3.76							
	Ca II	< 7.16	< +0.80							
	Sc II	< 5.32	< +2.15							
	Sc III	< 6.98	< +3.81							
	Ti II	5.81	+0.79	0.58	2	+0.52	+0.14	−0.00	+0.01	+0.18
	Ti III	< 8.47	< +3.45							

star	species	log ϵ	[X/H]	σ_Σ	$N_{\rm lines}$	σ_N	σ_T	σ_g	σ_ξ	σ_W
M13/WF4-3085	V II	< 6.01	< +2.01							
cont.	Cr I	< 8.87	< +3.20							
	Cr II	6.10	+0.43	0.14	4	+0.12	+0.10	+0.00	+0.00	+0.08
	Cr III	< 8.75	< +3.08							
	Mn I	< 9.03	< +3.64							
	Mn II	6.54	+1.15	0.13	1	+0.00	+0.08	+0.00	+0.00	+0.09
	Mn III	< 9.32	< +3.93							
	Fe I	8.45	+0.95	0.29	3	+0.24	+0.17	−0.03	+0.01	+0.11
	Fe II	8.18	+0.68	0.08	85	+0.18	+0.07	−0.00	−0.02	+0.08
	Fe I	8.25	+0.75	0.28	2	+0.23	−0.06	+0.03	−0.02	+0.11
	Co II	< 7.21	< +2.29							
	Ni II	6.11	−0.14	0.49	2	+0.47	+0.06	+0.02	+0.00	+0.09
	Sr II	< 5.07	< +2.10							
	Y II	< 5.50	< +3.26							
	Zr II	< 5.49	< +2.89							
	Ba II	< 5.34	< +3.21							
M13/WF4-3485	He I	9.50	−1.49	0.17	1	+0.00	−0.13	+0.03	−0.01	+0.10
	C I	< 9.98	< +1.46							
	C II	< 8.47	< −0.05							
	N I	< 9.40	< +1.48							
	N II	< 9.57	< +1.65							
	O I	< 9.95	< +1.12							
	O II	< 10.91	< +2.08							
	Mg I	< 8.10	< +0.52							
	Mg II	5.96	−1.62	0.14	2	+0.10	+0.03	−0.01	−0.01	+0.09
	Al I	< 7.75	< +1.28							
	Al II	< 6.80	< +0.33							
	Al III	< 8.50	< +2.03							
	Si I	< 9.11	< +1.56							
	Si II	6.12	−1.43	0.07	4	+0.07	−0.02	+0.01	−0.01	+0.09
	Si III	< 9.29	< +1.74							
	P II	< 7.46	< +2.01							
	P III	< 8.73	< +3.28							
	S I	< 10.38	< +3.05							
	S II	< 7.93	< +0.60							
	S III	< 10.44	< +3.11							
	Ca II	4.70	−1.66	0.15	1	+0.00	+0.13	−0.02	−0.06	+0.05
	Sc II	< 4.18	< +1.01							
	Ti II	4.49	−0.53	0.16	1	+0.00	+0.12	−0.01	+0.00	+0.10
	V II	< 5.55	< +1.55							
	Cr I	< 8.19	< +2.52							
	Cr II	< 5.55	< −0.12							
	Cr III	< 9.08	< +3.41							
	Mn I	< 8.57	< +3.18							
	Mn II	< 6.93	< +1.54							
	Fe I	7.59	+0.09	0.20	1	+0.00	+0.16	−0.03	+0.00	+0.11
	Fe II	7.43	−0.07	0.07	58	+0.23	+0.05	+0.01	−0.03	+0.11
	Fe III	< 9.08	< +1.58							
	Co II	< 7.03	< +2.11							
	Ni I	< 9.68	< +3.43							
	Ni II	< 7.01	< +0.76							
	Zn I	< 7.62	< +3.02							
	Sr II	< 4.72	< +1.75							
	Y II	< 5.16	< +2.92							
	Zr II	< 4.95	< +2.35							
	Ba II	< 5.39	< +3.26							
M15/B78	He I	< 12.39	< +1.40							
	C I	< 8.07	< −0.45							
	O I	< 9.11	< +0.28							
	Mg I	5.78	−1.80	0.18	3	+0.07	+0.07	−0.01	−0.16	+0.04
	Mg II	5.53	−2.05	0.07	1	+0.00	−0.01	+0.01	−0.06	+0.04
	Al I	< 7.84	< +1.37							
	Si I	< 12.03	< +4.48							
	Si II	< 6.77	< −0.78							

star	species	log ϵ	[X/H]	σ_Σ	$N_{\rm lines}$	σ_N	σ_T	σ_g	σ_ξ	σ_W
M15/B78	Ca I	4.16	−2.20	0.16	2	+0.01	+0.10	−0.02	−0.11	+0.05
cont.	Ca II	< 4.88	< −1.48							
	Sc II	0.76	−2.41	0.08	1	+0.00	+0.06	+0.01	−0.03	+0.04
	Ti I	< 4.91	< −0.11							
	Ti II	3.18	−1.84	0.10	11	+0.13	+0.05	+0.02	−0.07	+0.05
	V II	< 3.23	< −0.77							
	Cr I	< 4.28	< −1.39							
	Cr II	3.85	−1.82	0.09	1	+0.00	+0.03	+0.02	−0.03	+0.08
	Mn I	< 4.10	< −1.29							
	Mn II	< 4.82	< −0.57							
	Fe I	5.11	−2.39	0.12	10	+0.09	+0.09	−0.01	−0.07	+0.06
	Fe II	5.07	−2.43	0.14	5	+0.10	+0.03	+0.02	−0.12	+0.06
	Co I	< 4.98	< +0.06							
	Ni I	< 10.75	< +4.50							
	Ni II	< 4.95	< −1.30							
	Zn I	< 4.59	< −0.01							
	Sr II	0.28	−2.69	0.22	2	+0.18	+0.09	+0.01	−0.04	+0.08
	Y II	< 1.46	< −0.78							
	Zr II	< 1.82	< −0.78							
	Ba II	< 0.74	< −1.39							
	La II	< 1.44	< +0.27							
M15/B84	He I	< 10.11	< −0.88							
	C I	< 9.94	< +1.42							
	C II	< 8.35	< −0.17							
	N I	< 9.14	< +1.22							
	N II	< 9.94	< +2.02							
	O I	< 9.86	< +1.03							
	O II	< 11.18	< +2.35							
	Mg I	< 8.09	< +0.51							
	Mg II	5.41	−2.17	0.13	2	+0.06	+0.05	+0.00	−0.00	+0.11
	Al I	< 7.61	< +1.14							
	Al II	< 6.63	< +0.16							
	Al III	< 8.72	< +2.25							
	Si I	< 9.65	< +2.10							
	Si II	6.22	−1.33	0.08	3	+0.07	−0.01	+0.02	−0.01	+0.08
	Si III	< 9.49	< +1.94							
	P II	< 7.21	< +1.76							
	P III	< 8.68	< +3.23							
	S I	< 10.22	< +2.89							
	S II	< 7.85	< +0.52							
	S III	< 10.78	< +3.45							
	Ca II	4.93	−1.43	0.24	2	+0.14	+0.15	−0.03	−0.06	+0.11
	Sc II	< 4.12	< +0.95							
	Ti II	< 5.41	< +0.39							
	V II	< 5.56	< +1.56							
	Cr I	< 8.20	< +2.53							
	Cr II	< 5.43	< −0.24							
	Cr III	< 9.55	< +3.88							
	Mn I	< 8.26	< +2.87							
	Mn II	< 6.70	< +1.31							
	Fe I	< 8.81	< +1.31							
	Fe II	7.47	−0.03	0.07	48	+0.21	+0.05	+0.01	−0.04	+0.10
	Fe III	< 9.09	< +1.59							
	Co I	< 11.33	< +6.41							
	Co II	< 6.73	< +1.81							
	Ni II	< 6.43	< +0.18							
	Zn I	< 7.41	< +2.81							
	Sr II	< 4.51	< +1.54							
	Y II	< 5.30	< +3.06							
	Zr II	< 5.04	< +2.44							
	Ba II	< 5.30	< +3.17							
M15/B124	He I	< 12.03	< +1.04							
	C I	< 8.15	< −0.37							
	N I	< 8.65	< +0.73							

star	species	log ϵ	[X/H]	σ_Σ	$N_{\rm lines}$	σ_N	σ_T	σ_g	σ_ξ	σ_W
M15/B124	O I	$<$ 9.34	$<$ +0.51							
cont.	Mg I	6.22	−1.36	0.19	3	+0.21	+0.08	−0.01	−0.06	+0.08
	Mg II	5.34	−2.24	0.14	2	+0.11	−0.01	+0.01	−0.01	+0.08
	Al I	4.14	−2.33	0.35	2	+0.33	+0.09	−0.01	−0.00	+0.08
	Al II	$<$ 7.33	$<$ +0.86							
	Si I	$<$ 12.16	$<$ +4.61							
	Si II	$<$ 6.77	$<$ −0.78							
	Ca I	4.61	−1.76	0.33	2	+0.28	+0.12	−0.02	−0.05	+0.10
	Ca II	$<$ 5.01	$<$ −1.35							
	Sc II	1.05	−2.12	0.10	1	+0.00	+0.07	+0.02	−0.01	+0.07
	Ti I	$<$ 5.26	$<$ +0.24							
	Ti II	3.26	−1.76	0.07	13	+0.14	+0.05	+0.01	−0.02	+0.07
	V II	$<$ 3.58	$<$ −0.42							
	Cr I	$<$ 4.61	$<$ −1.06							
	Cr II	$<$ 4.13	$<$ −1.54							
	Mn I	$<$ 4.65	$<$ −0.74							
	Mn II	$<$ 5.38	$<$ −0.01							
	Fe I	5.37	−2.13	0.11	13	+0.07	+0.10	−0.01	−0.02	+0.09
	Fe II	5.35	−2.15	0.08	9	+0.14	+0.04	+0.02	−0.03	+0.09
	Co I	$<$ 5.42	$<$ +0.50							
	Ni I	$<$ 10.92	$<$ +4.67							
	Ni II	$<$ 5.28	$<$ −0.97							
	Zn I	$<$ 4.95	$<$ +0.35							
	Sr II	0.38	−2.59	0.13	3	+0.10	+0.09	+0.01	−0.02	+0.08
	Y II	$<$ 1.72	$<$ −0.52							
	Zr II	$<$ 2.17	$<$ −0.43							
	Ba II	$<$ 1.20	$<$ −0.93							
	La II	$<$ 2.42	$<$ +1.25							
	Eu II	$<$ 1.94	$<$ +1.43							
M15/B130	He I	$<$ 12.48	$<$ +1.49							
	C I	$<$ 8.17	$<$ −0.35							
	O I	$<$ 8.55	$<$ −0.28							
	Na I	$<$ 6.18	$<$ −0.15							
	Mg I	5.67	−1.91	0.11	3	+0.01	+0.09	−0.01	−0.05	+0.06
	Mg II	5.47	−2.11	0.13	4	+0.19	−0.02	+0.01	−0.02	+0.10
	Si I	$<$ 7.68	$<$ +0.13							
	Si II	$<$ 6.41	$<$ −1.14							
	Ca I	4.04	−2.32	0.17	1	+0.00	+0.13	−0.01	−0.03	+0.11
	Ca II	$<$ 6.33	$<$ −0.03							
	Sc II	0.79	−2.38	0.19	1	+0.00	+0.07	+0.02	−0.01	+0.17
	Ti I	$<$ 5.28	$<$ +0.26							
	Ti II	3.14	−1.88	0.09	11	+0.16	+0.06	+0.02	−0.03	+0.08
	V II	$<$ 4.42	$<$ +0.42							
	Cr I	$<$ 4.51	$<$ −1.16							
	Cr II	$<$ 4.56	$<$ −1.11							
	Mn I	$<$ 5.44	$<$ +0.05							
	Mn II	$<$ 5.81	$<$ +0.42							
	Fe I	4.98	−2.52	0.15	4	+0.12	+0.12	−0.01	−0.02	+0.11
	Fe II	4.99	−2.51	0.09	5	+0.06	+0.04	+0.02	−0.06	+0.08
	Co I	$<$ 6.15	$<$ +1.23							
	Ni I	$<$ 6.01	$<$ −0.24							
	Ni II	$<$ 6.62	$<$ +0.37							
	Zn I	$<$ 4.99	$<$ +0.39							
	Sr II	$<$ 2.24	$<$ −0.73							
	Y II	$<$ 1.96	$<$ −0.28							
	Zr II	$<$ 3.29	$<$ +0.69							
	Ba II	$<$ 1.79	$<$ −0.34							
M15/B153	He I	$<$ 12.72	$<$ +1.73							
	C I	$<$ 8.23	$<$ −0.29							
	O I	$<$ 8.45	$<$ −0.38							
	Na I	$<$ 6.36	$<$ +0.03							
	Mg I	5.58	−2.00	0.26	2	+0.11	+0.17	−0.02	−0.08	+0.14
	Mg II	5.47	−2.11	0.12	1	+0.00	−0.01	+0.02	−0.07	+0.09
	Si I	$<$ 7.99	$<$ +0.44							

star	species	log ϵ	[X/H]	σ_Σ	$N_{\rm lines}$	σ_N	σ_T	σ_g	σ_ξ	σ_W
M15/B153	Si II	<6.08	<-1.47							
cont.	Ca I	<4.41	<-1.95							
	Ca II	<6.23	<-0.13							
	Sc II	<1.49	<-1.68							
	Ti I	<5.32	$<+0.30$							
	Ti II	<3.31	<-1.71							
	V II	<4.62	$<+0.62$							
	Cr I	<4.75	<-0.92							
	Cr II	<4.39	<-1.28							
	Mn I	<5.60	$<+0.21$							
	Mn II	<5.86	$<+0.47$							
	Fe I	<6.13	<-1.37							
	Fe II	5.12	-2.38	0.37	2	$+0.04$	$+0.07$	$+0.02$	-0.31	$+0.19$
	Co I	<7.41	$<+2.49$							
	Ni I	<5.99	<-0.26							
	Ni II	<7.04	$<+0.79$							
	Zn I	<4.95	$<+0.35$							
	Sr II	<2.39	<-0.58							
	Y II	<1.96	<-0.28							
	Zr II	<3.36	$<+0.76$							
	Ba II	<1.61	<-0.52							
M15/B177	He I	<12.54	$<+1.55$							
	C I	<8.10	<-0.42							
	O I	<8.60	<-0.23							
	Na I	<6.17	<-0.16							
	Mg I	5.75	-1.83	0.21	3	$+0.17$	$+0.08$	-0.01	-0.15	$+0.06$
	Mg II	5.61	-1.97	0.09	2	$+0.01$	-0.01	$+0.01$	-0.06	$+0.07$
	Si I	<7.76	$<+0.21$							
	Si II	5.74	-1.81	0.10	1	$+0.00$	$+0.00$	$+0.02$	-0.04	$+0.09$
	Ca I	4.28	-2.08	0.21	1	$+0.00$	$+0.11$	-0.02	-0.14	$+0.11$
	Ca II	<6.26	<-0.10							
	Sc II	<2.15	<-1.02							
	Ti I	<5.04	$<+0.02$							
	Ti II	3.12	-1.90	0.11	11	$+0.19$	$+0.06$	$+0.02$	-0.06	$+0.08$
	V II	<4.34	$<+0.34$							
	Cr I	<4.68	<-0.99							
	Cr II	<4.35	<-1.32							
	Mn I	<5.40	$<+0.01$							
	Mn II	<5.63	$<+0.24$							
	Fe I	5.07	-2.43	0.17	5	$+0.18$	$+0.10$	-0.01	-0.07	$+0.14$
	Fe II	5.14	-2.36	0.16	5	$+0.18$	$+0.03$	$+0.02$	-0.12	$+0.08$
	Co I	<5.72	$<+0.80$							
	Ni I	<5.71	<-0.54							
	Ni II	<6.94	$<+0.69$							
	Zn I	<4.60	$<+0.00$							
	Sr II	<1.23	<-1.74							
	Y II	<1.50	<-0.74							
	Zr I	<4.93	$<+2.33$							
	Zr II	<2.93	$<+0.33$							
	Ba II	<1.16	<-0.97							
M15/B203	He I	9.54	-1.45	0.28	1	$+0.00$	-0.16	$+0.03$	-0.01	$+0.23$
	C I	<10.22	$<+1.70$							
	C II	<8.46	<-0.06							
	N I	<10.02	$<+2.10$							
	N II	<10.16	$<+2.24$							
	O I	<9.14	$<+0.31$							
	O II	<11.52	$<+2.69$							
	Na I	<8.81	$<+2.48$							
	Mg I	<8.69	$<+1.11$							
	Mg II	5.86	-1.72	0.45	2	$+0.42$	$+0.06$	-0.01	-0.01	$+0.15$
	Al I	<10.44	$<+3.97$							
	Al II	<7.15	$<+0.68$							
	Al III	<8.92	$<+2.45$							
	Si I	<11.99	$<+4.44$							

star	species	log ϵ	[X/H]	σ_Σ	$N_{\rm lines}$	σ_N	σ_T	σ_g	σ_ξ	σ_W
M15/B203	Si II	6.62	−0.93	0.16	3	+0.13	−0.00	+0.01	−0.02	+0.18
cont.	Si III	< 9.56	< +2.01							
	P II	< 6.92	< +1.47							
	P III	< 9.32	< +3.87							
	S II	< 7.64	< +0.31							
	S III	< 11.07	< +3.74							
	Ca II	5.13	−1.23	0.43	1	+0.00	+0.16	−0.02	−0.09	+0.39
	Sc II	< 5.57	< +2.40							
	Ti II	< 6.44	< +1.42							
	V I	< 10.27	< +6.27							
	V II	< 7.51	< +3.51							
	V III	< 10.20	< +6.20							
	Cr I	< 9.26	< +3.59							
	Cr II	6.35	+0.68	0.46	1	+0.00	+0.16	−0.01	−0.02	+0.43
	Cr III	< 10.78	< +5.11							
	Mn I	< 9.92	< +4.53							
	Mn II	< 7.11	< +1.72							
	Fe I	< 10.11	< +2.61							
	Fe II	7.44	−0.06	0.13	33	+0.23	+0.10	+0.00	−0.06	+0.15
	Fe III	< 9.46	< +1.96							
	Co II	< 8.30	< +3.38							
	Ni I	< 9.99	< +3.74							
	Ni II	< 7.84	< +1.59							
	Ni III	< 11.69	< +5.44							
	Zn I	< 8.28	< +3.68							
	Sr II	< 6.34	< +3.37							
	Y II	< 5.99	< +3.75							
	Zr II	< 6.80	< +4.20							
	Ba II	< 6.18	< +4.05							
M15/B218	He I	< 12.97	< +1.98							
	C I	< 8.32	< −0.20							
	O I	< 8.65	< −0.18							
	Na I	< 6.08	< −0.25							
	Mg I	5.80	−1.78	0.15	3	+0.04	+0.11	−0.01	−0.08	+0.09
	Mg II	5.62	−1.96	0.22	2	+0.20	−0.01	+0.01	−0.03	+0.09
	Si I	< 7.74	< +0.19							
	Si II	< 6.32	< −1.23							
	Ca I	3.92	−2.44	0.20	1	+0.00	+0.15	−0.02	−0.03	+0.13
	Ca II	< 6.10	< −0.26							
	Sc II	< 2.13	< −1.04							
	Ti I	< 5.17	< +0.15							
	Ti II	3.21	−1.81	0.15	7	+0.24	+0.08	+0.02	−0.05	+0.12
	V II	< 4.36	< +0.36							
	Cr I	< 5.00	< −0.67							
	Cr II	< 4.49	< −1.18							
	Mn I	< 5.57	< +0.18							
	Mn II	< 5.73	< +0.34							
	Fe I	5.36	−2.14	0.55	2	+0.52	+0.13	−0.01	−0.04	+0.12
	Fe II	5.06	−2.44	0.20	3	+0.20	+0.05	+0.02	−0.10	+0.11
	Co I	< 6.58	< +1.66							
	Ni I	< 5.87	< −0.38							
	Ni II	< 6.80	< +0.55							
	Zn I	< 4.88	< +0.28							
	Sr II	< 2.05	< −0.92							
	Y II	< 2.11	< −0.13							
	Zr II	< 3.25	< +0.65							
	Ba II	< 1.18	< −0.95							
M15/B244	He I	< 12.47	< +1.48							
	C I	< 8.28	< −0.24							
	O I	< 8.40	< −0.43							
	Na I	< 6.23	< −0.10							
	Mg I	5.77	−1.81	0.25	3	+0.20	+0.17	−0.01	−0.12	+0.06
	Mg II	5.36	−2.22	0.26	2	+0.23	−0.02	+0.01	−0.06	+0.10
	Si I	< 7.85	< +0.30							

star	species	log ϵ	[X/H]	σ_Σ	$N_{\rm lines}$	σ_N	σ_T	σ_g	σ_ξ	σ_W
M15/B244	Si II	< 6.35	< −1.20							
cont.	Ca I	4.30	−2.06	0.26	1	+0.00	+0.22	−0.02	−0.10	+0.09
	Ca II	< 6.33	< −0.03							
	Sc II	1.07	−2.10	0.17	1	+0.00	+0.13	+0.02	−0.05	+0.10
	Ti I	< 5.43	< +0.41							
	Ti II	3.16	−1.86	0.14	9	+0.14	+0.10	+0.02	−0.07	+0.08
	V II	< 4.54	< +0.54							
	Cr I	< 4.94	< −0.73							
	Cr II	< 4.42	< −1.25							
	Mn I	< 5.40	< +0.01							
	Mn II	< 5.79	< +0.40							
	Fe I	5.40	−2.10	0.22	4	+0.05	+0.19	−0.01	−0.09	+0.10
	Fe II	5.03	−2.47	0.18	5	+0.22	+0.08	+0.02	−0.11	+0.08
	Co I	< 6.09	< +1.17							
	Ni I	< 5.98	< −0.27							
	Ni II	< 6.68	< +0.43							
	Zn I	< 4.84	< +0.24							
	Sr II	< 1.74	< −1.23							
	Y II	< 1.77	< −0.47							
	Zr II	< 2.97	< +0.37							
	Ba II	< 1.28	< −0.85							
M15/B267	He I	9.74	−1.25	0.60	2	+0.52	−0.04	+0.04	−0.04	+0.29
	C I	< 10.21	< +1.69							
	C II	7.97	−0.55	0.15	1	+0.00	−0.08	+0.02	−0.01	+0.12
	N I	< 9.56	< +1.64							
	N II	8.61	+0.69	0.47	1	+0.00	+0.02	+0.05	−0.10	+0.46
	O I	< 10.54	< +1.71							
	O II	< 10.85	< +2.02							
	Mg I	< 9.51	< +1.93							
	Mg II	5.96	−1.62	0.09	1	+0.00	+0.05	+0.00	−0.01	+0.07
	Al I	< 8.43	< +1.96							
	Al II	< 7.42	< +0.95							
	Al III	< 8.56	< +2.09							
	Si I	< 9.65	< +2.10							
	Si II	< 6.43	< −1.12							
	Si III	< 9.10	< +1.55							
	P I	< 9.91	< +4.46							
	P II	6.90	+1.45	0.14	4	+0.17	+0.00	+0.02	−0.03	+0.16
	P III	< 8.40	< +2.95							
	S I	< 10.35	< +3.02							
	S II	< 7.94	< +0.61							
	S III	< 10.04	< +2.71							
	Ca II	5.86	−0.51	0.20	2	+0.13	+0.11	−0.04	−0.05	+0.08
	Sc II	< 4.56	< +1.39							
	Ti II	6.27	+1.25	0.15	24	+0.29	+0.12	−0.01	−0.05	+0.11
	Ti III	< 8.97	< +3.95							
	V II	< 6.07	< +2.07							
	Cr I	< 8.84	< +3.17							
	Cr II	6.29	+0.62	1.37	2	+0.98	+0.66	−0.22	−0.14	+0.64
	Cr III	< 9.56	< +3.89							
	Mn I	< 9.50	< +4.11							
	Mn II	< 7.21	< +1.82							
	Mn III	< 9.98	< +4.59							
	Fe I	8.40	+0.90	0.22	2	+0.04	+0.18	−0.03	−0.03	+0.11
	Fe II	7.99	+0.49	0.09	69	+0.25	+0.07	+0.00	−0.05	+0.12
	Fe III	< 9.61	< +2.11							
	Co I	< 11.82	< +6.90							
	Co II	< 7.38	< +2.46							
	Ni II	5.70	−0.55	0.15	1	+0.00	+0.05	+0.02	−0.02	+0.14
	Zn I	< 8.26	< +3.66							
	Sr II	< 5.32	< +2.35							
	Y II	4.78	+2.54	0.21	2	+0.01	+0.13	−0.01	−0.06	+0.15
	Zr II	< 5.82	< +3.22							
	Ba II	< 5.67	< +3.54							

star	species	log ϵ	[X/H]	σ_Σ	$N_{\rm lines}$	σ_N	σ_T	σ_g	σ_ξ	σ_W
M15/B279	He I	9.39	−1.60	0.15	1	+0.00	−0.08	+0.03	+0.00	+0.12
	C I	< 10.03	< +1.51							
	C II	< 8.27	< −0.25							
	N I	< 9.36	< +1.44							
	N II	< 9.61	< +1.69							
	O I	< 10.16	< +1.33							
	O II	< 11.14	< +2.31							
	Mg I	< 8.11	< +0.53							
	Mg II	5.85	−1.73	0.09	3	+0.07	+0.03	+0.00	−0.01	+0.09
	Al I	< 7.61	< +1.14							
	Al II	< 7.10	< +0.63							
	Al III	< 8.63	< +2.16							
	Si I	< 10.54	< +2.99							
	Si II	< 6.28	< −1.27							
	Si III	< 9.48	< +1.93							
	P II	6.80	+1.35	0.12	1	+0.00	−0.03	+0.02	+0.00	+0.11
	P III	< 8.62	< +3.17							
	S I	< 9.96	< +2.63							
	S II	< 7.60	< +0.27							
	S III	< 10.23	< +2.90							
	Ca I	< 9.21	< +2.85							
	Ca II	5.82	−0.55	0.14	2	+0.09	+0.08	−0.04	−0.02	+0.06
	Sc II	< 4.01	< +0.84							
	Sc III	< 7.50	< +4.33							
	Ti I	< 8.97	< +3.95							
	Ti II	5.47	+0.45	0.11	21	+0.18	+0.10	−0.01	−0.01	+0.09
	Ti III	< 8.86	< +3.84							
	V II	< 5.99	< +1.99							
	Cr I	< 7.95	< +2.28							
	Cr II	5.69	+0.02	0.10	5	+0.14	+0.06	+0.01	−0.01	+0.09
	Cr III	< 9.38	< +3.71							
	Mn I	< 8.45	< +3.06							
	Mn II	< 6.87	< +1.48							
	Fe I	8.22	+0.72	0.13	11	+0.19	+0.11	−0.03	−0.01	+0.10
	Fe II	7.94	+0.44	0.04	126	+0.22	+0.02	+0.01	−0.02	+0.10
	Fe I	7.78	+0.28	0.16	1	+0.00	−0.06	+0.04	−0.01	+0.14
	Co I	< 8.65	< +3.73							
	Co II	< 6.95	< +2.03							
	Ni II	< 6.47	< +0.22							
	Zn I	< 7.54	< +2.94							
	Sr II	< 4.35	< +1.38							
	Y II	< 5.13	< +2.89							
	Zr II	< 5.03	< +2.43							
	Ba II	< 4.89	< +2.76							
M15/B315	He I	< 10.48	< −0.51							
	C I	< 10.44	< +1.92							
	C II	< 8.79	< +0.27							
	N I	< 10.24	< +2.32							
	N II	< 10.55	< +2.63							
	O I	< 9.52	< +0.69							
	O II	11.68	+2.85	0.34	1	+0.00	−0.16	+0.01	−0.01	+0.20
	Na I	< 8.94	< +2.61							
	Mg I	< 8.88	< +1.30							
	Mg II	5.73	−1.85	0.17	4	+0.19	+0.05	+0.00	−0.01	+0.20
	Al I	< 10.44	< +3.97							
	Al II	< 7.49	< +1.02							
	Al III	< 9.04	< +2.57							
	Si I	< 11.53	< +3.98							
	Si II	6.59	−0.96	0.14	3	+0.08	−0.00	+0.00	−0.02	+0.17
	Si III	< 9.73	< +2.18							
	P II	6.64	+1.19	0.15	3	+0.07	−0.06	+0.02	−0.02	+0.15
	P III	< 9.50	< +4.05							
	S I	< 10.69	< +3.36							
	S II	8.47	+1.14	0.25	1	+0.00	−0.08	+0.02	−0.01	+0.21
	S III	< 10.85	< +3.52							

star	species	log ϵ	[X/H]	σ_Σ	$N_{\rm lines}$	σ_N	σ_T	σ_g	σ_ξ	σ_W
M15/B315	Ca II	5.59	−0.77	0.36	2	+0.21	+0.12	−0.02	−0.06	+0.25
cont.	Sc II	< 5.65	< +2.48							
	Ti II	5.15	+0.13	0.18	1	+0.00	+0.12	−0.01	−0.02	+0.12
	Ti III	< 10.46	< +5.44							
	V II	< 7.82	< +3.82							
	Cr I	< 9.88	< +4.21							
	Cr II	< 6.87	< +1.20							
	Cr III	< 10.86	< +5.19							
	Mn I	< 11.17	< +5.78							
	Mn II	< 7.18	< +1.79							
	Fe I	7.91	+0.41	0.28	1	+0.00	+0.18	−0.02	−0.01	+0.19
	Fe II	7.62	+0.12	0.08	74	+0.34	+0.05	+0.00	−0.04	+0.15
	Fe III	< 9.24	< +1.74							
	Co II	< 8.23	< +3.31							
	Ni I	< 9.41	< +3.16							
	Ni II	< 8.04	< +1.79							
	Zn I	< 8.32	< +3.72							
	Sr II	< 6.31	< +3.34							
	Y II	< 5.99	< +3.75							
	Zr II	< 6.65	< +4.05							
	Ba II	< 6.32	< +4.19							
M15/B331	He I	< 12.49	< +1.50							
	C I	< 8.11	< −0.41							
	N I	< 9.10	< +1.18							
	O I	< 8.38	< −0.45							
	Na I	< 6.42	< +0.09							
	Mg I	5.91	−1.67	0.21	3	+0.18	+0.15	−0.02	−0.03	+0.07
	Mg II	5.77	−1.81	0.07	2	+0.01	−0.01	+0.01	−0.02	+0.06
	Al II	< 7.61	< +1.14							
	Si I	< 8.26	< +0.71							
	Si II	< 6.74	< −0.81							
	S I	< 8.10	< +0.77							
	Ca I	3.78	−2.58	0.24	1	+0.00	+0.21	−0.03	−0.01	+0.10
	Ca II	< 6.49	< +0.13							
	Sc II	0.95	−2.22	0.16	1	+0.00	+0.12	+0.02	−0.01	+0.11
	Ti I	< 5.74	< +0.72							
	Ti II	3.30	−1.72	0.17	5	+0.24	+0.09	+0.02	−0.04	+0.11
	V I	< 5.67	< +1.67							
	V II	< 4.58	< +0.58							
	Cr I	< 4.80	< −0.87							
	Cr II	< 4.99	< −0.68							
	Mn I	< 5.68	< +0.29							
	Mn II	< 5.92	< +0.53							
	Fe I	5.25	−2.25	0.31	2	+0.18	+0.21	−0.01	−0.03	+0.14
	Fe II	5.59	−1.91	0.14	5	+0.08	+0.06	+0.02	−0.09	+0.15
	Co I	< 7.35	< +2.43							
	Co II	< 6.93	< +2.01							
	Ni I	< 6.13	< −0.12							
	Ni II	< 7.26	< +1.01							
	Zn I	< 4.89	< +0.29							
	Sr II	< 2.62	< −0.35							
	Y II	< 1.98	< −0.26							
	Zr II	< 3.55	< +0.95							
	Ba II	< 1.80	< −0.33							
	La II	< 3.05	< +1.88							
	Ce II	< 4.16	< +2.58							
	Nd II	< 5.93	< +4.43							
	Eu II	< 2.60	< +2.09							
M15/B334	He I	10.25	−0.74	0.24	1	+0.00	−0.21	+0.03	−0.02	+0.10
	C II	< 8.74	< +0.22							
	Mg I	< 7.40	< −0.18							
	Mg II	5.45	−2.13	0.17	2	+0.15	+0.01	+0.00	−0.06	+0.06
	Al I	< 7.24	< +0.77							
	Al II	< 7.00	< +0.53							

star	species	log ϵ	[X/H]	σ_Σ	$N_{\rm lines}$	σ_N	σ_T	σ_g	σ_ξ	σ_W
M15/B334	Si I	< 8.15	< +0.60							
cont.	Si II	5.68	−1.87	0.17	2	+0.13	−0.05	+0.01	−0.05	+0.09
	S II	< 7.97	< +0.64							
	Ca II	4.22	−2.14	0.64	1	+0.00	+0.20	−0.02	−0.60	+0.08
	Sc II	< 3.20	< +0.03							
	Ti II	< 4.78	< −0.24							
	Cr II	< 5.18	< −0.49							
	Fe I	< 7.64	< +0.14							
	Fe II	5.46	−2.04	0.23	1	+0.00	+0.04	+0.02	−0.18	+0.13
	Ni II	< 5.72	< −0.53							
	Sr II	< 3.81	< +0.84							
M15/B348	He I	11.11	+0.12	0.28	2	+0.10	−0.22	+0.02	−0.03	+0.13
	C II	< 8.96	< +0.44							
	Mg I	< 7.35	< −0.23							
	Mg II	5.20	−2.38	0.08	1	+0.00	+0.02	+0.01	−0.03	+0.07
	Al I	< 7.34	< +0.87							
	Al II	< 7.18	< +0.71							
	Si I	< 8.45	< +0.90							
	Si II	< 6.73	< −0.82							
	Ca II	< 5.28	< −1.08							
	Sc II	< 3.53	< +0.36							
	Ti II	< 4.73	< −0.29							
	Cr II	< 5.14	< −0.53							
	Fe I	< 7.64	< +0.14							
	Fe II	5.17	−2.33	0.17	1	+0.00	+0.04	+0.02	−0.05	+0.16
	Ni II	< 6.26	< +0.01							
	Sr II	< 3.78	< +0.81							
M15/B374	He I	9.37	−1.62	0.22	1	+0.00	−0.10	+0.03	+0.00	+0.19
	C I	< 10.47	< +1.95							
	C II	< 8.64	< +0.12							
	N I	< 10.14	< +2.22							
	N II	< 10.29	< +2.37							
	O I	< 9.66	< +0.83							
	O II	< 11.54	< +2.71							
	Na I	< 8.59	< +2.26							
	Mg I	< 8.99	< +1.41							
	Mg II	5.86	−1.72	0.18	3	+0.16	+0.04	−0.00	−0.02	+0.19
	Al I	< 10.10	< +3.63							
	Al II	< 7.34	< +0.87							
	Al III	< 9.08	< +2.61							
	Si I	< 11.52	< +3.97							
	Si II	6.26	−1.29	0.22	1	+0.00	−0.01	+0.01	−0.02	+0.22
	Si III	< 9.66	< +2.11							
	P I	< 10.00	< +4.55							
	P II	7.04	+1.59	0.17	3	+0.10	−0.04	+0.02	−0.03	+0.21
	P III	< 9.28	< +3.83							
	S I	< 10.67	< +3.34							
	S II	< 8.07	< +0.74							
	S III	< 10.98	< +3.65							
	Ca II	5.68	−0.68	0.47	2	+0.41	+0.10	−0.03	−0.05	+0.21
	Sc II	< 5.51	< +2.34							
	Ti II	5.67	+0.65	0.15	9	+0.20	+0.11	−0.01	−0.02	+0.17
	Ti III	< 9.85	< +4.83							
	V II	< 7.80	< +3.80							
	Cr I	< 10.22	< +4.55							
	Cr II	7.24	+1.57	0.35	2	+0.25	+0.09	+0.01	−0.03	+0.23
	Cr III	< 10.23	< +4.56							
	Mn I	< 9.61	< +4.22							
	Mn II	< 7.50	< +2.11							
	Fe I	8.26	+0.76	0.35	2	+0.26	+0.15	−0.03	−0.02	+0.18
	Fe II	7.98	+0.48	0.07	108	+0.31	+0.04	+0.00	−0.05	+0.17
	Fe III	< 9.90	< +2.40							
	Co I	< 11.88	< +6.96							
	Co II	< 8.47	< +3.55							

star	species	log ϵ	[X/H]	σ_Σ	$N_{\rm lines}$	σ_N	σ_T	σ_g	σ_ξ	σ_W
M15/B374	Ni I	< 9.98	< +3.73							
cont.	Ni II	6.93	+0.68	0.28	1	+0.00	+0.01	+0.02	−0.01	+0.28
	Zn I	< 8.92	< +4.32							
	Sr II	< 6.51	< +3.54							
	Y II	< 6.09	< +3.85							
	Zr II	< 6.89	< +4.29							
	Ba II	< 6.22	< +4.09							
M15/B424	He I	< 12.46	< +1.47							
	C I	< 8.27	< −0.25							
	N I	< 8.97	< +1.05							
	O I	< 8.61	< −0.22							
	Na I	< 6.25	< −0.08							
	Mg I	5.49	−2.09	0.22	2	+0.06	+0.10	−0.01	−0.14	+0.13
	Mg II	5.52	−2.06	0.25	2	+0.22	−0.01	+0.01	−0.08	+0.09
	Si I	< 7.82	< +0.27							
	Si II	< 6.27	< −1.28							
	Ca I	< 4.91	< −1.45							
	Ca II	< 6.20	< −0.16							
	Sc II	< 1.63	< −1.54							
	Ti I	< 5.13	< +0.11							
	Ti II	< 3.15	< −1.87							
	V II	< 4.45	< +0.45							
	Cr I	< 4.66	< −1.01							
	Cr II	< 4.41	< −1.26							
	Mn I	< 5.38	< −0.01							
	Mn II	< 5.63	< +0.24							
	Fe I	< 5.63	< −1.87							
	Fe II	5.33	−2.17	0.62	2	+0.40	+0.04	+0.01	−0.44	+0.16
	Co I	< 6.35	< +1.43							
	Ni I	< 5.73	< −0.52							
	Ni II	< 7.03	< +0.78							
	Zn I	< 4.69	< +0.09							
	Sr II	< 2.09	< −0.88							
	Y II	< 2.01	< −0.23							
	Zr II	< 3.27	< +0.67							
	Ba II	< 1.30	< −0.83							
M15/B558	He I	< 12.65	< +1.66							
	C I	< 8.34	< −0.18							
	N I	< 9.38	< +1.46							
	O I	< 8.58	< −0.25							
	Na I	< 6.46	< +0.13							
	Mg I	5.64	−1.94	0.36	2	+0.30	+0.14	−0.01	−0.11	+0.10
	Mg II	5.16	−2.42	0.11	2	+0.03	−0.01	+0.01	−0.02	+0.10
	Si I	< 8.05	< +0.50							
	Si II	< 6.62	< −0.93							
	Ca I	4.00	−2.36	0.27	1	+0.00	+0.20	−0.02	−0.04	+0.18
	Ca II	< 6.44	< +0.08							
	Sc II	< 2.54	< −0.63							
	Ti I	< 5.53	< +0.51							
	Ti II	3.21	−1.81	0.15	7	+0.12	+0.10	+0.02	−0.08	+0.13
	V II	< 5.00	< +1.00							
	Cr I	< 5.00	< −0.67							
	Cr II	< 4.62	< −1.05							
	Mn I	< 5.78	< +0.39							
	Mn II	< 5.80	< +0.41							
	Fe I	5.15	−2.35	0.30	3	+0.28	+0.17	−0.02	−0.06	+0.17
	Fe II	5.19	−2.31	0.22	4	+0.17	+0.06	+0.02	−0.17	+0.14
	Co I	< 7.53	< +2.61							
	Ni I	< 6.01	< −0.24							
	Ni II	< 7.00	< +0.75							
	Zn I	< 4.70	< +0.10							
	Sr II	< 3.10	< +0.13							
	Y II	< 2.35	< +0.11							
	Zr II	< 3.55	< +0.95							
	Ba II	< 1.74	< −0.39							

star	species	$\log\epsilon$	[X/H]	σ_Σ	$N_{\rm lines}$	σ_N	σ_T	σ_g	σ_ξ	σ_W
M68/W71	He I	< 12.06	< +1.07							
	C I	< 8.53	< +0.01							
	N I	< 8.90	< +0.98							
	O I	< 9.40	< +0.57							
	Mg I	5.63	−1.95	0.26	2	+0.20	+0.10	−0.03	−0.09	+0.10
	Mg II	5.49	−2.09	0.12	2	+0.06	+0.00	+0.01	−0.09	+0.06
	Al II	< 7.64	< +1.17							
	Si II	< 6.92	< −0.63							
	Ca I	< 5.13	< −1.23							
	Ca II	< 6.67	< +0.31							
	Sc II	< 2.19	< −0.98							
	Ti I	< 5.99	< +0.97							
	Ti II	3.31	−1.71	0.21	4	+0.26	+0.07	+0.01	−0.10	+0.12
	V II	< 4.75	< +0.75							
	Cr I	< 5.51	< −0.16							
	Cr II	< 4.61	< −1.06							
	Mn I	< 5.98	< +0.59							
	Mn II	< 5.80	< +0.41							
	Fe I	5.34	−2.16	0.21	2	+0.06	+0.11	−0.03	−0.11	+0.12
	Fe II	5.68	−1.82	0.47	3	+0.10	+0.04	+0.01	−0.45	+0.15
	Ni I	< 7.40	< +1.15							
	Ni II	< 5.96	< −0.29							
	Sr II	< 1.77	< −1.20							
	Y II	< 2.72	< +0.48							
	Zr II	< 3.64	< +1.04							
	Ba II	< 3.07	< +0.94							
M68/W72	He I	10.85	−0.14	0.27	1	+0.00	−0.21	+0.03	−0.04	+0.16
	C I	< 9.58	< +1.06							
	C II	< 9.54	< +1.02							
	O I	< 9.52	< +0.69							
	Mg I	< 6.75	< −0.83							
	Mg II	5.41	−2.17	0.24	2	+0.21	+0.00	+0.00	−0.08	+0.09
	Al II	< 7.41	< +0.94							
	Si II	< 6.82	< −0.73							
	Ca I	< 7.32	< +0.96							
	Sc II	< 3.28	< +0.11							
	Ti II	< 4.27	< −0.75							
	Cr II	< 5.24	< −0.43							
	Mn II	< 7.17	< +1.78							
	Fe I	< 7.45	< −0.05							
	Fe II	< 5.97	< −1.53							
	Ni II	< 6.91	< +0.66							
	Sr II	< 3.97	< +1.00							
M68/W114	He I	< 12.81	< +1.82							
	C I	< 8.08	< −0.44							
	O I	< 9.53	< +0.70							
	Mg I	5.59	−1.99	0.15	3	+0.13	+0.07	−0.00	−0.09	+0.07
	Mg II	5.71	−1.87	0.18	2	+0.14	−0.01	+0.02	−0.04	+0.10
	Si I	< 11.85	< +4.30							
	Si II	< 7.07	< −0.48							
	Ca I	3.91	−2.45	0.14	1	+0.00	+0.10	−0.01	−0.06	+0.08
	Ca II	< 6.21	< −0.15							
	Sc II	0.82	−2.35	0.08	1	+0.00	+0.05	+0.01	−0.03	+0.05
	Ti I	< 4.84	< −0.18							
	Ti II	3.03	−1.99	0.08	14	+0.14	+0.05	+0.02	−0.04	+0.07
	V II	< 3.78	< −0.22							
	Cr I	< 4.17	< −1.50							
	Cr II	< 4.13	< −1.54							
	Mn I	< 4.41	< −0.98							
	Mn II	< 5.13	< −0.26							
	Fe I	5.07	−2.43	0.11	14	+0.22	+0.08	−0.01	−0.04	+0.09
	Fe II	5.09	−2.41	0.11	7	+0.15	+0.03	+0.02	−0.07	+0.10
	Co I	< 5.53	< +0.61							
	Ni I	< 5.78	< −0.47							

star	species	log ϵ	[X/H]	σ_Σ	$N_{\rm lines}$	σ_N	σ_T	σ_g	σ_ξ	σ_W
M68/W114	Ni II	< 5.26	< −0.99							
cont.	Zn I	< 4.52	< −0.08							
	Sr II	< 0.84	< −2.13							
	Y II	< 1.26	< −0.98							
	Zr II	< 2.50	< −0.10							
	Ba II	< 0.79	< −1.34							
	La II	< 1.74	< +0.57							
	Eu II	< 1.11	< +0.60							
M68/W120	He I	< 12.29	< +1.30							
	C I	< 8.60	< +0.08							
	N I	< 8.61	< +0.69							
	O I	< 9.47	< +0.64							
	Mg I	5.45	−2.12	0.31	2	+0.22	+0.19	−0.03	−0.03	+0.10
	Mg II	5.53	−2.05	0.08	2	+0.04	−0.01	+0.01	−0.02	+0.07
	Al II	< 7.58	< +1.11							
	Si I	< 12.46	< +4.91							
	Si II	< 6.82	< −0.73							
	Ca I	< 5.26	< −1.10							
	Ca II	< 6.39	< +0.03							
	Sc II	< 1.73	< −1.44							
	Ti I	< 5.75	< +0.73							
	Ti II	3.15	−1.87	0.16	1	+0.00	+0.12	+0.02	−0.02	+0.10
	V II	< 4.74	< +0.74							
	Cr I	< 5.13	< −0.54							
	Cr II	< 4.64	< −1.03							
	Mn I	< 5.42	< +0.03							
	Mn II	< 5.94	< +0.55							
	Fe I	< 6.07	< −1.43							
	Fe II	5.38	−2.12	0.17	3	+0.06	+0.09	+0.02	−0.10	+0.13
	Co I	< 7.24	< +2.32							
	Ni I	< 6.79	< +0.54							
	Ni II	< 6.10	< −0.15							
	Zn I	< 5.58	< +0.98							
	Sr II	< 2.17	< −0.80							
	Y II	< 2.83	< +0.59							
	Zr II	< 3.72	< +1.12							
	Ba II	< 2.35	< +0.22							
M68/W161	He I	< 12.13	< +1.14							
	C I	< 8.49	< −0.03							
	N I	< 8.82	< +0.90							
	O I	< 9.48	< +0.65							
	Mg I	5.59	−1.99	0.20	2	+0.15	+0.09	−0.02	−0.02	+0.09
	Mg II	5.45	−2.13	0.08	1	+0.00	+0.00	+0.01	−0.01	+0.08
	Al I	4.49	−1.98	0.13	1	+0.00	+0.09	−0.02	−0.01	+0.09
	Al II	< 7.43	< +0.96							
	Si I	< 12.49	< +4.94							
	Si II	< 6.95	< −0.60							
	Ca I	4.04	−2.32	0.15	1	+0.00	+0.12	−0.03	−0.01	+0.09
	Sc II	< 2.23	< −0.94							
	Ti I	< 6.03	< +1.01							
	Ti II	3.19	−1.83	0.11	9	+0.23	+0.06	+0.01	−0.02	+0.10
	V II	< 4.11	< +0.11							
	Cr I	< 5.29	< −0.38							
	Cr II	< 4.96	< −0.71							
	Mn I	5.78	+0.39	0.15	1	+0.00	+0.09	−0.02	+0.00	+0.12
	Mn II	< 6.07	< +0.68							
	Fe I	5.31	−2.19	0.13	6	+0.11	+0.10	−0.02	−0.02	+0.11
	Fe II	5.28	−2.22	0.10	6	+0.09	+0.04	+0.02	−0.06	+0.10
	Co I	< 6.13	< +1.21							
	Ni II	< 6.01	< −0.24							
	Zn I	< 5.63	< +1.03							
	Sr II	< 2.33	< −0.64							
	Y II	< 2.57	< +0.33							
	Zr II	< 3.44	< +0.84							
	Ba II	< 2.47	< +0.34							

star	species	$\log \epsilon$	[X/H]	σ_Σ	$N_{\rm lines}$	σ_N	σ_T	σ_g	σ_ξ	σ_W
M68/W279	He I	< 12.20	$< +1.21$							
	C I	< 8.64	$< +0.12$							
	O I	< 9.54	$< +0.71$							
	Mg I	5.72	-1.86	0.17	2	$+0.06$	$+0.12$	-0.03	-0.03	$+0.09$
	Mg II	5.51	-2.07	0.13	2	$+0.06$	$+0.00$	$+0.01$	-0.03	$+0.11$
	Si I	< 12.78	$< +5.23$							
	Si II	< 6.88	< -0.67							
	Ca I	< 5.49	< -0.87							
	Ca II	< 6.44	$< +0.08$							
	Sc II	2.19	-0.98	0.29	1	$+0.00$	$+0.10$	$+0.01$	-0.04	$+0.27$
	Ti I	< 6.15	$< +1.13$							
	Ti II	3.26	-1.76	0.12	8	$+0.19$	$+0.08$	$+0.01$	-0.03	$+0.10$
	V II	< 4.69	$< +0.69$							
	Cr I	< 5.86	$< +0.19$							
	Cr II	< 4.61	< -1.06							
	Mn I	< 5.98	$< +0.59$							
	Mn II	< 6.09	$< +0.70$							
	Fe I	5.29	-2.21	0.23	2	$+0.14$	$+0.14$	-0.02	-0.01	$+0.12$
	Fe II	5.41	-2.09	0.15	7	$+0.12$	$+0.07$	$+0.01$	-0.11	$+0.14$
	Ni I	< 7.46	$< +1.21$							
	Ni II	< 6.39	$< +0.14$							
	Sr II	< 2.89	< -0.08							
	Y II	< 2.45	$< +0.21$							
	Zr II	< 4.03	$< +1.43$							
	Ba II	< 3.36	$< +1.23$							
M68/W324	He I	< 12.82	$< +1.83$							
	C I	< 8.08	< -0.44							
	N I	< 8.66	$< +0.74$							
	O I	< 9.39	$< +0.56$							
	Mg I	6.08	-1.50	0.45	3	$+0.30$	$+0.07$	-0.00	-0.37	$+0.18$
	Mg II	5.70	-1.88	0.16	2	$+0.11$	-0.02	$+0.02$	-0.08	$+0.08$
	Si I	< 11.70	$< +4.15$							
	Si II	< 6.63	< -0.92							
	S I	< 7.69	$< +0.36$							
	Ca I	3.90	-2.46	0.21	1	$+0.00$	$+0.09$	-0.01	-0.12	$+0.15$
	Ca II	< 5.99	< -0.37							
	Sc II	1.18	-1.99	0.22	1	$+0.00$	$+0.05$	$+0.02$	-0.12	$+0.18$
	Ti I	< 4.83	< -0.19							
	Ti II	3.26	-1.76	0.17	8	$+0.24$	$+0.05$	$+0.02$	-0.12	$+0.12$
	V I	< 4.36	$< +0.36$							
	V II	< 3.65	< -0.35							
	Cr I	< 3.96	< -1.71							
	Cr II	< 4.08	< -1.59							
	Mn I	< 4.11	< -1.28							
	Mn II	< 5.11	< -0.28							
	Fe I	5.07	-2.43	0.18	6	$+0.16$	$+0.09$	-0.00	-0.13	$+0.12$
	Fe II	5.15	-2.35	0.26	4	$+0.26$	$+0.03$	$+0.02$	-0.19	$+0.14$
	Co I	< 5.00	$< +0.08$							
	Ni I	< 5.70	< -0.55							
	Ni II	< 5.25	< -1.00							
	Zn I	< 4.27	< -0.33							
	Sr II	< 0.34	< -2.63							
	Y II	< 1.21	< -1.03							
	Zr II	< 2.08	< -0.52							
	Ba II	< 0.52	< -1.61							
	La II	< 1.59	$< +0.42$							
	Ce II	< 2.05	$< +0.47$							
	Nd II	< 1.81	$< +0.31$							
	Eu II	< 0.83	$< +0.32$							
M68/W340	He I	< 12.84	$< +1.85$							
	C I	< 8.27	< -0.25							
	N I	< 9.11	$< +1.19$							
	O I	< 9.38	$< +0.55$							
	Mg I	5.82	-1.76	0.24	3	$+0.21$	$+0.06$	-0.01	-0.16	$+0.09$

star	species	log ϵ	[X/H]	σ_Σ	$N_{\rm lines}$	σ_N	σ_T	σ_g	σ_ξ	σ_W
M68/W340	Mg II	5.53	−2.05	0.09	1	+0.00	+0.00	+0.02	−0.03	+0.08
cont.	Si I	< 11.84	< +4.29							
	Si II	< 7.08	< −0.47							
	S I	< 7.69	< +0.36							
	Ca I	4.13	−2.23	0.18	1	+0.00	+0.09	−0.01	−0.13	+0.09
	Ca II	< 6.38	< +0.02							
	Sc II	0.83	−2.34	0.09	1	+0.00	+0.05	+0.02	−0.04	+0.06
	Ti I	< 5.13	< +0.11							
	Ti II	3.23	−1.79	0.12	12	+0.17	+0.04	+0.02	−0.09	+0.09
	V I	< 5.42	< +1.42							
	V II	< 4.44	< +0.44							
	Cr I	< 4.65	< −1.02							
	Cr II	< 4.26	< −1.41							
	Mn I	< 4.92	< −0.47							
	Mn II	< 5.63	< +0.24							
	Fe I	5.17	−2.33	0.14	11	+0.16	+0.08	−0.01	−0.09	+0.11
	Fe II	5.31	−2.19	0.16	7	+0.15	+0.03	+0.02	−0.14	+0.11
	Co I	< 6.53	< +1.61							
	Co II	< 5.89	< +0.97							
	Ni I	< 6.21	< −0.04							
	Ni II	< 5.87	< −0.38							
	Zn I	< 4.87	< +0.27							
	Sr II	< 1.13	< −1.84							
	Y II	< 1.89	< −0.35							
	Zr II	< 3.03	< +0.43							
	Ba II	< 1.15	< −0.98							
	La II	< 2.76	< +1.59							
	Ce II	< 2.71	< +1.13							
	Nd II	< 2.42	< +0.92							
	Eu II	< 1.70	< +1.19							
M68/W464	He I	< 12.86	< +1.87							
	C I	< 7.95	< −0.57							
	N I	< 8.89	< +0.97							
	O I	< 9.40	< +0.57							
	Mg I	5.34	−2.24	0.14	3	+0.14	+0.04	−0.01	−0.05	+0.11
	Mg II	5.27	−2.31	0.08	1	+0.00	−0.01	+0.02	−0.01	+0.08
	Si I	< 11.55	< +4.00							
	Si II	< 6.94	< −0.61							
	S I	< 7.49	< +0.16							
	Ca I	4.54	−1.82	0.32	1	+0.00	+0.05	+0.00	−0.17	+0.27
	Ca II	< 5.97	< −0.39							
	Sc II	1.10	−2.07	0.11	1	+0.00	+0.03	+0.02	−0.04	+0.10
	Ti I	< 4.62	< −0.40							
	Ti II	3.14	−1.88	0.08	9	+0.11	+0.03	+0.03	−0.04	+0.09
	V I	< 4.12	< +0.12							
	V II	< 3.47	< −0.53							
	Cr I	< 3.75	< −1.92							
	Cr II	< 3.72	< −1.95							
	Mn I	< 3.88	< −1.51							
	Mn II	< 4.88	< −0.51							
	Fe I	5.11	−2.39	0.16	6	+0.29	+0.05	−0.00	−0.06	+0.14
	Fe II	5.31	−2.19	0.13	5	+0.08	+0.02	+0.03	−0.09	+0.16
	Co I	< 4.88	< −0.04							
	Co II	< 5.34	< +0.42							
	Ni I	< 5.32	< −0.93							
	Ni II	< 4.99	< −1.26							
	Zn I	< 4.24	< −0.36							
	Sr II	< 0.37	< −2.60							
	Y II	< 0.71	< −1.53							
	Zr II	< 2.01	< −0.59							
	Ba II	< 0.21	< −1.92							
	La II	< 1.28	< +0.11							
	Ce II	< 1.63	< +0.05							
	Nd II	< 1.63	< +0.13							
	Eu II	< 0.54	< +0.03							

star	species	$\log\epsilon$	[X/H]	σ_Σ	$N_{\rm lines}$	σ_N	σ_T	σ_g	σ_ξ	σ_W
M68/W468	He I	<12.37	$<+1.38$							
	C I	<8.35	<-0.17							
	N I	<8.94	$<+1.02$							
	O I	<9.41	$<+0.58$							
	Mg I	5.15	-2.43	0.18	1	$+0.00$	$+0.17$	-0.02	-0.02	$+0.05$
	Mg II	5.32	-2.26	0.10	3	$+0.13$	-0.01	$+0.01$	-0.01	$+0.07$
	Si I	<12.44	$<+4.89$							
	Si II	<7.04	<-0.51							
	Ca I	<4.59	<-1.77							
	Ca II	<6.34	<-0.02							
	Sc II	<1.68	<-1.49							
	Ti I	<5.57	$<+0.55$							
	Ti II	3.00	-2.02	0.13	6	$+0.13$	$+0.11$	$+0.01$	-0.02	$+0.09$
	V II	<4.42	$<+0.42$							
	Cr I	<4.98	<-0.69							
	Cr II	<4.52	<-1.15							
	Mn I	<5.63	$<+0.24$							
	Mn II	<5.81	$<+0.42$							
	Fe I	4.96	-2.54	0.30	2	$+0.20$	$+0.18$	-0.02	-0.02	$+0.14$
	Fe II	5.14	-2.36	0.13	6	$+0.11$	$+0.09$	$+0.02$	-0.06	$+0.09$
	Co I	<6.38	$<+1.46$							
	Ni I	<6.60	$<+0.35$							
	Ni II	<5.66	<-0.59							
	Zn I	<4.99	$<+0.39$							
	Sr II	<1.74	<-1.23							
	Y II	<1.95	<-0.29							
	Zr II	<3.32	$<+0.72$							
	Ba II	<1.66	<-0.47							
M68/W510	He I	<12.79	$<+1.80$							
	C I	<8.08	<-0.44							
	O I	<9.47	$<+0.64$							
	Mg I	5.60	-1.98	0.23	3	$+0.07$	$+0.04$	$+0.00$	-0.22	$+0.07$
	Mg II	5.59	-1.99	0.13	2	$+0.10$	-0.02	$+0.02$	-0.06	$+0.06$
	Si I	<11.64	$<+4.09$							
	Si II	<7.18	<-0.37							
	S I	<7.50	$<+0.17$							
	Ca I	3.86	-2.50	0.18	1	$+0.00$	$+0.06$	-0.01	-0.14	$+0.10$
	Ca II	<5.90	<-0.46							
	Sc II	1.10	-2.08	0.14	2	$+0.08$	$+0.03$	$+0.02$	-0.06	$+0.09$
	Ti I	<4.62	<-0.40							
	Ti II	3.07	-1.95	0.11	13	$+0.17$	$+0.03$	$+0.02$	-0.09	$+0.07$
	V I	<4.45	$<+0.45$							
	V II	<3.57	<-0.43							
	Cr I	<3.82	<-1.85							
	Cr II	<3.96	<-1.71							
	Mn I	<3.98	<-1.41							
	Mn II	<4.90	<-0.49							
	Fe I	5.00	-2.50	0.13	11	$+0.16$	$+0.05$	-0.01	-0.11	$+0.09$
	Fe II	5.05	-2.45	0.14	7	$+0.20$	$+0.01$	$+0.02$	-0.11	$+0.08$
	Co I	<5.09	$<+0.17$							
	Ni I	<5.38	<-0.87							
	Ni II	<5.18	<-1.07							
	Zn I	<4.29	<-0.31							
	Sr II	0.43	-2.54	0.14	1	$+0.00$	$+0.05$	$+0.02$	-0.09	$+0.10$
	Y II	<0.95	<-1.29							
	Zr II	<2.04	<-0.56							
	Ba II	<0.50	<-1.63							
	La II	<1.17	$<+0.00$							
	Ce II	<1.98	$<+0.40$							
	Nd II	<1.76	$<+0.26$							
	Eu II	<0.84	$<+0.33$							
M92/B29	He I	<12.95	$<+1.96$							
	C I	<8.10	<-0.42							
	N I	<9.08	$<+1.16$							

star	species	log ϵ	[X/H]	σ_Σ	$N_{\rm lines}$	σ_N	σ_T	σ_g	σ_ξ	σ_W
M92/B29	O I	< 8.45	< −0.38							
cont.	Na I	< 5.98	< −0.35							
	Mg I	5.27	−2.31	0.18	3	+0.18	+0.10	−0.01	−0.04	+0.09
	Mg II	5.62	−1.96	0.11	2	+0.08	−0.02	+0.02	−0.03	+0.07
	Si I	< 7.82	< +0.27							
	Si II	< 6.42	< −1.13							
	S I	< 7.65	< +0.32							
	Ca I	3.28	−3.08	0.15	1	+0.00	+0.11	−0.02	−0.02	+0.09
	Ca II	< 6.22	< −0.14							
	Sc II	< 1.77	< −1.40							
	Ti I	< 4.94	< −0.08							
	Ti II	2.76	−2.26	0.09	5	+0.10	+0.05	+0.02	−0.03	+0.09
	V I	< 4.66	< +0.66							
	V II	< 4.23	< +0.23							
	Cr I	< 4.41	< −1.26							
	Cr II	< 4.03	< −1.64							
	Mn I	< 5.13	< −0.26							
	Mn II	< 5.07	< −0.32							
	Fe I	4.67	−2.83	0.24	2	+0.14	+0.11	−0.01	−0.04	+0.16
	Fe II	5.10	−2.40	0.15	5	+0.08	+0.04	+0.02	−0.12	+0.13
	Co I	< 5.86	< +0.94							
	Co II	< 6.13	< +1.21							
	Ni I	< 5.42	< −0.83							
	Ni II	< 6.84	< +0.59							
	Zn I	< 4.47	< −0.13							
	Sr II	< 1.13	< −1.84							
	Y II	< 1.55	< −0.69							
	Zr II	< 2.73	< +0.13							
	Ba II	< 0.72	< −1.41							
	La II	< 1.58	< +0.41							
	Ce II	< 2.42	< +0.84							
	Nd II	< 2.38	< +0.88							
	Eu II	< 1.42	< +0.91							
M92/B30	He I	< 11.65	< +0.66							
	C I	< 8.20	< −0.32							
	N I	< 8.35	< +0.43							
	O I	< 9.09	< +0.26							
	Mg I	6.19	−1.39	0.21	3	+0.07	+0.12	−0.01	−0.15	+0.07
	Mg II	5.60	−1.98	0.07	2	+0.04	−0.01	+0.01	−0.04	+0.03
	Al II	< 7.36	< +0.89							
	Si I	< 12.23	< +4.68							
	Si II	< 6.65	< −0.90							
	Ca I	4.76	−1.60	0.23	1	+0.00	+0.15	−0.03	−0.15	+0.07
	Ca II	< 5.94	< −0.42							
	Sc II	1.26	−1.91	0.11	1	+0.00	+0.09	+0.01	−0.05	+0.05
	Ti I	< 5.09	< +0.07							
	Ti II	3.48	−1.54	0.11	13	+0.07	+0.08	+0.02	−0.06	+0.06
	V II	< 3.88	< −0.12							
	Cr I	< 4.34	< −1.33							
	Cr II	< 4.01	< −1.66							
	Mn I	< 4.35	< −1.04							
	Mn II	< 5.06	< −0.33							
	Fe I	5.46	−2.04	0.15	11	+0.09	+0.13	−0.02	−0.05	+0.08
	Fe II	5.41	−2.09	0.11	12	+0.13	+0.06	+0.02	−0.07	+0.08
	Co I	< 5.47	< +0.55							
	Co II	< 5.63	< +0.71							
	Ni I	< 6.10	< −0.15							
	Ni II	< 4.97	< −1.28							
	Zn I	< 5.04	< +0.44							
	Sr II	< 0.81	< −2.16							
	Y II	< 1.40	< −0.84							
	Zr II	< 2.13	< −0.47							
	Ba II	< 1.02	< −1.11							
	La II	< 2.00	< +0.83							
	Eu II	< 1.10	< +0.59							

star	species	$\log \epsilon$	[X/H]	σ_Σ	$N_{\rm lines}$	σ_N	σ_T	σ_g	σ_ξ	σ_W
M92/B103	He I	< 12.31	$< +1.32$							
	C I	< 7.83	< -0.69							
	O I	< 8.37	< -0.46							
	Na I	< 5.72	< -0.61							
	Mg I	5.75	-1.83	0.30	3	$+0.10$	$+0.12$	-0.00	-0.26	$+0.04$
	Mg II	5.51	-2.07	0.09	2	$+0.05$	-0.02	$+0.02$	-0.05	$+0.04$
	Si I	< 7.36	< -0.19							
	Si II	< 5.95	< -1.60							
	S I	< 7.34	$< +0.01$							
	Ca I	4.05	-2.31	0.25	1	$+0.00$	$+0.15$	-0.02	-0.18	$+0.07$
	Ca II	< 5.70	< -0.66							
	Sc II	0.76	-2.41	0.14	1	$+0.00$	$+0.10$	$+0.03$	-0.05	$+0.08$
	Ti I	< 4.57	< -0.45							
	Ti II	3.07	-1.95	0.12	12	$+0.10$	$+0.08$	$+0.02$	-0.08	$+0.06$
	V I	< 4.28	$< +0.28$							
	V II	< 3.88	< -0.12							
	Cr I	< 3.81	< -1.86							
	Cr II	< 3.86	< -1.81							
	Mn I	< 4.73	< -0.66							
	Mn II	< 4.77	< -0.62							
	Fe I	5.05	-2.45	0.18	8	$+0.11$	$+0.15$	-0.00	-0.09	$+0.10$
	Fe II	5.00	-2.50	0.14	6	$+0.13$	$+0.05$	$+0.03$	-0.11	$+0.05$
	Co I	< 4.95	$< +0.03$							
	Ni I	< 5.21	< -1.04							
	Ni II	< 6.37	$< +0.12$							
	Zn I	< 4.18	< -0.42							
	Sr II	0.15	-2.82	0.21	3	$+0.21$	$+0.12$	$+0.02$	-0.05	$+0.09$
	Y II	< 1.02	< -1.22							
	Zr II	< 2.27	< -0.33							
	Ba II	< 0.44	< -1.69							
	La II	< 1.55	$< +0.38$							
	Ce II	< 2.32	$< +0.74$							
	Nd II	< 1.59	$< +0.09$							
	Eu II	< 0.87	$< +0.36$							
M92/B145	He I	< 11.70	$< +0.71$							
	C I	< 8.12	< -0.40							
	N I	< 8.32	$< +0.40$							
	O I	< 8.82	< -0.01							
	Mg I	5.42	-2.16	0.17	3	$+0.06$	$+0.15$	-0.02	-0.04	$+0.08$
	Mg II	5.63	-1.95	0.11	2	$+0.07$	$+0.00$	$+0.01$	-0.06	$+0.05$
	Al II	< 6.83	$< +0.36$							
	Si I	< 12.57	$< +5.02$							
	Si II	< 6.52	< -1.03							
	Ca I	< 4.35	< -2.01							
	Ca II	< 5.97	< -0.39							
	Sc II	< 1.30	< -1.87							
	Ti II	2.98	-2.04	0.15	5	$+0.18$	$+0.09$	$+0.01$	-0.05	$+0.10$
	V II	< 3.77	< -0.23							
	Cr I	< 4.47	< -1.20							
	Cr II	< 3.91	< -1.76							
	Mn I	< 4.74	< -0.65							
	Mn II	< 5.08	< -0.31							
	Fe I	5.11	-2.39	0.19	4	$+0.07$	$+0.16$	-0.02	-0.06	$+0.14$
	Fe II	5.13	-2.37	0.22	5	$+0.10$	$+0.08$	$+0.02$	-0.19	$+0.13$
	Ni I	< 6.11	< -0.14							
	Ni II	< 4.86	< -1.39							
	Zn I	< 5.11	$< +0.51$							
	Sr II	< 1.00	< -1.97							
	Y II	< 1.43	< -0.81							
	Zr II	< 2.31	< -0.29							
	Ba II	< 1.09	< -1.04							
M92/B148	He I	< 12.34	$< +1.35$							
	C I	< 7.91	< -0.61							
	O I	< 8.34	< -0.49							

star	species	log ϵ	[X/H]	σ_Σ	$N_{\rm lines}$	σ_N	σ_T	σ_g	σ_ξ	σ_W
M92/B148	Na I	< 5.95	< −0.38							
cont.	Mg I	5.41	−2.17	0.17	3	+0.11	+0.11	−0.01	−0.09	+0.08
	Mg II	5.52	−2.06	0.10	2	+0.04	−0.02	+0.02	−0.05	+0.07
	Si I	< 7.54	< −0.01							
	Si II	< 5.88	< −1.67							
	Ca I	3.64	−2.72	0.20	1	+0.00	+0.14	−0.02	−0.04	+0.14
	Ca II	< 5.77	< −0.59							
	Sc II	< 1.13	< −2.04							
	Ti I	< 4.77	< −0.25							
	Ti II	2.93	−2.09	0.11	1	+0.00	+0.07	+0.02	−0.03	+0.08
	V II	< 3.70	< −0.30							
	Cr I	< 4.04	< −1.63							
	Cr II	< 3.95	< −1.72							
	Mn I	< 4.96	< −0.43							
	Mn II	< 4.96	< −0.43							
	Fe I	< 5.01	< −2.49							
	Fe II	4.86	−2.64	0.15	4	+0.16	+0.07	+0.03	−0.08	+0.08
	Co I	< 4.96	< +0.04							
	Ni I	< 5.45	< −0.80							
	Ni II	< 6.39	< +0.14							
	Zn I	< 4.23	< −0.37							
	Sr II	< 0.65	< −2.32							
	Y II	< 1.13	< −1.11							
	Zr II	< 2.22	< −0.38							
	Ba II	< 0.60	< −1.53							
M92/B176	He I	10.65	−0.34	0.45	2	+0.21	−0.38	+0.05	−0.07	+0.10
	C II	< 8.43	< −0.09							
	Mg I	< 7.02	< −0.56							
	Mg II	5.26	−2.32	0.10	2	+0.01	+0.04	+0.01	−0.07	+0.05
	Al II	< 6.48	< +0.01							
	Si II	5.63	−1.92	0.15	2	+0.07	−0.06	+0.03	−0.06	+0.09
	S II	< 7.88	< +0.55							
	Sc II	< 2.81	< −0.36							
	Ti II	< 4.38	< −0.64							
	Cr II	< 4.69	< −0.98							
	Fe I	6.83	−0.67	0.35	1	+0.00	+0.33	−0.03	−0.03	+0.11
	Fe II	5.15	−2.35	0.31	2	+0.28	+0.07	+0.03	−0.09	+0.07
	Ni II	< 5.46	< −0.79							
	Sr II	< 3.05	< +0.08							
M92/B202	He I	< 12.06	< +1.07							
	C I	< 7.80	< −0.72							
	O I	< 9.09	< +0.26							
	Mg I	5.98	−1.60	0.20	3	+0.18	+0.10	−0.01	−0.11	+0.06
	Mg II	5.47	−2.11	0.06	2	+0.04	+0.00	+0.02	−0.02	+0.04
	Si I	< 11.87	< +4.32							
	Si II	< 6.45	< −1.10							
	Ca I	4.25	−2.11	0.16	1	+0.00	+0.13	−0.01	−0.07	+0.07
	Ca II	< 5.74	< −0.62							
	Sc II	1.13	−2.04	0.10	1	+0.00	+0.08	+0.02	−0.03	+0.04
	Ti I	< 4.58	< −0.44							
	Ti II	3.29	−1.73	0.08	13	+0.14	+0.06	+0.02	−0.03	+0.05
	V I	< 4.28	< +0.28							
	V II	< 3.33	< −0.67							
	Cr I	< 4.02	< −1.65							
	Cr II	< 3.92	< −1.75							
	Mn I	< 3.88	< −1.51							
	Mn II	< 4.68	< −0.71							
	Fe I	5.29	−2.21	0.14	12	+0.10	+0.12	−0.01	−0.05	+0.06
	Fe II	5.27	−2.23	0.08	10	+0.09	+0.05	+0.02	−0.05	+0.07
	Co I	< 4.63	< −0.29							
	Co II	< 5.31	< +0.39							
	Ni I	< 5.63	< −0.62							
	Ni II	< 4.58	< −1.67							
	Zn I	< 4.43	< −0.17							

star	species	$\log \epsilon$	[X/H]	σ_Σ	$N_{\rm lines}$	σ_N	σ_T	σ_g	σ_ξ	σ_W
M92/B202	Sr II	0.41	−2.56	0.11	4	+0.05	+0.10	+0.01	−0.03	+0.06
cont.	Y II	< 0.91	< −1.33							
	Zr I	< 4.01	< +1.41							
	Zr II	< 1.95	< −0.65							
	Ba II	< 0.55	< −1.58							
	La II	< 1.38	< +0.21							
	Ce II	< 1.93	< +0.35							
	Nd II	< 1.77	< +0.27							
	Eu II	< 0.72	< +0.21							
M92/B219	He I	< 12.07	< +1.08							
	C I	< 7.93	< −0.59							
	N I	< 8.73	< +0.81							
	O I	< 8.28	< −0.55							
	Na I	< 6.16	< −0.17							
	Mg I	6.40	−1.18	0.38	3	+0.30	+0.22	−0.02	−0.21	+0.13
	Mg II	5.50	−2.08	0.11	3	+0.13	−0.02	+0.02	−0.04	+0.06
	Al II	< 7.17	< +0.70							
	Si I	< 7.89	< +0.34							
	Si II	< 5.85	< −1.70							
	Ca I	4.92	−1.44	0.45	1	+0.00	+0.29	−0.02	−0.25	+0.24
	Ca II	< 6.04	< −0.32							
	Sc II	< 1.75	< −1.42							
	Ti I	< 5.20	< +0.18							
	Ti II	3.45	−1.57	0.21	10	+0.24	+0.15	+0.02	−0.11	+0.14
	V II	< 4.16	< +0.16							
	Cr I	< 4.26	< −1.41							
	Cr II	< 4.30	< −1.37							
	Mn I	< 5.19	< −0.20							
	Mn II	< 5.34	< −0.05							
	Fe I	5.34	−2.16	0.33	3	+0.17	+0.28	−0.01	−0.07	+0.14
	Fe II	5.36	−2.14	0.21	5	+0.12	+0.10	+0.02	−0.16	+0.13
	Co I	< 5.55	< +0.63							
	Ni I	< 5.75	< −0.50							
	Ni II	< 6.54	< +0.29							
	Zn I	< 4.60	< +0.00							
	Sr II	1.01	−1.96	0.38	1	+0.00	+0.24	+0.01	−0.20	+0.22
	Y II	< 1.62	< −0.62							
	Zr II	< 2.47	< −0.13							
	Ba II	< 0.87	< −1.26							
	La II	< 2.18	< +1.01							
M92/B233	He I	< 11.84	< +0.85							
	C I	< 7.92	< −0.60							
	N I	< 8.58	< +0.66							
	O I	< 8.28	< −0.55							
	Na I	< 6.06	< −0.27							
	Mg I	5.76	−1.82	0.33	3	+0.38	+0.15	−0.02	−0.09	+0.11
	Mg II	5.71	−1.87	0.22	2	+0.20	−0.01	+0.02	−0.04	+0.07
	Si I	< 7.81	< +0.26							
	Si II	< 6.27	< −1.28							
	Ca I	< 4.57	< −1.79							
	Ca II	< 5.92	< −0.44							
	Sc II	< 1.33	< −1.84							
	Ti I	< 5.07	< +0.05							
	Ti II	3.17	−1.85	0.22	5	+0.34	+0.10	+0.01	−0.05	+0.16
	V II	< 4.30	< +0.30							
	Cr I	< 4.50	< −1.17							
	Cr II	< 3.99	< −1.68							
	Mn I	< 5.14	< −0.25							
	Mn II	< 5.31	< −0.08							
	Fe I	< 5.55	< −1.95							
	Fe II	5.28	−2.22	0.22	4	+0.16	+0.07	+0.02	−0.16	+0.15
	Co I	< 5.72	< +0.80							
	Ni I	< 6.02	< −0.23							
	Ni II	< 6.54	< +0.29							

star	species	log ϵ	[X/H]	σ_Σ	$N_{\rm lines}$	σ_N	σ_T	σ_g	σ_ξ	σ_W
M92/B233	Zn I	< 4.57	< −0.03							
cont.	Sr II	< 1.18	< −1.79							
	Y II	< 1.70	< −0.54							
	Zr II	< 2.69	< +0.09							
	Ba II	< 0.94	< −1.19							
M92/B246	He I	< 13.01	< +2.02							
	C I	< 7.78	< −0.74							
	O I	< 8.34	< −0.49							
	Na I	< 5.73	< −0.60							
	Mg I	5.40	−2.18	0.22	3	+0.13	+0.08	−0.00	−0.18	+0.04
	Mg II	5.47	−2.11	0.07	2	+0.00	−0.01	+0.03	−0.04	+0.05
	Si I	< 7.34	< −0.21							
	Si II	< 5.99	< −1.56							
	Ca I	3.73	−2.63	0.17	1	+0.00	+0.10	+0.00	−0.13	+0.06
	Ca II	< 5.85	< −0.51							
	Sc II	0.54	−2.63	0.10	1	+0.00	+0.06	+0.02	−0.04	+0.07
	Ti I	< 4.43	< −0.59							
	Ti II	2.89	−2.12	0.09	14	+0.14	+0.05	+0.03	−0.06	+0.06
	V I	< 4.10	< +0.10							
	V II	< 3.85	< −0.15							
	Cr I	< 3.68	< −1.99							
	Cr II	< 3.89	< −1.78							
	Mn I	< 4.59	< −0.80							
	Mn II	< 4.63	< −0.76							
	Fe I	4.79	−2.71	0.13	7	+0.15	+0.09	−0.01	−0.06	+0.07
	Fe II	4.90	−2.60	0.13	6	+0.13	+0.03	+0.03	−0.10	+0.06
	Co I	< 4.76	< −0.16							
	Ni I	< 5.12	< −1.13							
	Ni II	< 6.29	< +0.04							
	Zn I	< 3.98	< −0.62							
	Sr II	-0.14	−3.12	0.17	2	+0.11	+0.08	+0.02	−0.04	+0.09
	Y II	< 0.73	< −1.51							
	Zr II	< 2.00	< −0.60							
	Ba II	< 0.29	< −1.84							
	La II	< 1.18	< +0.01							
	Ce II	< 1.88	< +0.30							
	Nd II	< 1.55	< +0.05							
	Eu II	< 0.76	< +0.25							
M92/B251	He I	< 12.09	< +1.10							
	C I	< 7.92	< −0.60							
	O I	< 8.24	< −0.59							
	Na I	< 5.89	< −0.44							
	Mg I	5.47	−2.11	0.17	3	+0.08	+0.11	−0.01	−0.11	+0.04
	Mg II	5.49	−2.09	0.11	2	+0.08	−0.01	+0.01	−0.07	+0.04
	Si I	< 12.08	< +4.53							
	Si II	< 6.24	< −1.31							
	Ca I	3.78	−2.58	0.17	1	+0.00	+0.15	−0.02	−0.06	+0.06
	Ca II	< 5.82	< −0.54							
	Sc II	0.59	−2.58	0.11	1	+0.00	+0.08	+0.01	−0.03	+0.07
	Ti I	< 4.93	< −0.09							
	Ti II	2.90	−2.12	0.11	11	+0.13	+0.08	+0.02	−0.06	+0.06
	V II	< 3.91	< −0.09							
	Cr I	< 4.25	< −1.42							
	Cr II	< 4.05	< −1.62							
	Mn I	< 5.14	< −0.25							
	Mn II	< 5.10	< −0.29							
	Fe I	4.73	−2.77	0.17	3	+0.08	+0.14	−0.01	−0.04	+0.08
	Fe II	4.87	−2.63	0.17	5	+0.22	+0.05	+0.02	−0.11	+0.05
	Co I	< 5.09	< +0.17							
	Ni I	< 5.61	< −0.64							
	Zn I	< 4.42	< −0.18							
	Sr II	< 0.80	< −2.17							
	Y II	< 1.17	< −1.07							
	Zr II	< 2.28	< −0.32							
	Ba II	< 0.73	< −1.40							

star	species	$\log \epsilon$	[X/H]	σ_Σ	$N_{\rm lines}$	σ_N	σ_T	σ_g	σ_ξ	σ_W
M92/B365	He I	10.75	−0.24	0.40	1	+0.00	−0.37	+0.04	−0.07	+0.13
	C II	< 8.58	< +0.06							
	O I	< 9.43	< +0.60							
	Mg I	< 7.00	< −0.58							
	Mg II	5.32	−2.26	0.29	2	+0.27	+0.03	+0.01	−0.09	+0.07
	Al II	< 6.51	< +0.04							
	Si II	< 6.02	< −1.53							
	Si III	< 9.78	< +2.23							
	S II	< 7.94	< +0.61							
	Sc II	< 2.99	< −0.18							
	Ti II	< 4.31	< −0.71							
	Cr II	< 4.95	< −0.72							
	Mn II	< 6.13	< +0.74							
	Fe I	< 7.20	< −0.30							
	Fe II	< 5.57	< −1.93							
	Fe III	< 8.94	< +1.44							
	Ni II	< 5.66	< −0.59							
	Sr II	< 3.23	< +0.26							
M92/B455	He I	< 11.79	< +0.80							
	C I	< 8.17	< −0.35							
	O I	< 8.45	< −0.38							
	Na I	< 6.35	< +0.02							
	Mg I	5.59	−1.99	0.16	2	+0.05	+0.11	−0.02	−0.09	+0.05
	Mg II	5.45	−2.13	0.15	2	+0.12	−0.01	+0.01	−0.08	+0.04
	Si II	< 6.15	< −1.40							
	Ca I	< 4.54	< −1.82							
	Ca II	< 6.01	< −0.35							
	Sc II	< 1.42	< −1.75							
	Ti I	< 5.29	< +0.27							
	Ti II	3.08	−1.94	0.10	6	+0.11	+0.07	+0.01	−0.04	+0.08
	V II	< 4.24	< +0.24							
	Cr I	< 4.87	< −0.80							
	Cr II	< 4.21	< −1.46							
	Mn I	< 5.40	< +0.01							
	Mn II	< 5.30	< −0.09							
	Fe I	4.96	−2.54	0.23	2	+0.10	+0.16	−0.01	−0.04	+0.12
	Fe II	5.07	−2.43	0.14	5	+0.16	+0.05	+0.01	−0.10	+0.06
	Ni I	< 6.07	< −0.18							
	Ni II	< 6.64	< +0.39							
	Sr II	< 1.18	< −1.79							
	Y II	< 1.66	< −0.58							
	Zr II	< 2.73	< +0.13							
	Ba II	< 1.37	< −0.76							
M92/466	He I	< 11.99	< +1.00							
	C I	< 7.83	< −0.69							
	O I	< 9.11	< +0.28							
	Mg I	5.63	−1.95	0.18	3	+0.13	+0.11	−0.01	−0.11	+0.06
	Mg II	5.46	−2.12	0.10	2	+0.08	−0.01	+0.02	−0.05	+0.04
	Si I	< 12.18	< +4.63							
	Si II	< 6.56	< −0.99							
	Ca I	3.99	−2.37	0.17	1	+0.00	+0.15	−0.02	−0.06	+0.06
	Ca II	< 6.00	< −0.36							
	Sc II	0.65	−2.52	0.11	1	+0.00	+0.08	+0.02	−0.02	+0.07
	Ti I	< 4.90	< −0.12							
	Ti II	3.02	−2.00	0.10	13	+0.17	+0.07	+0.02	−0.05	+0.06
	V II	< 3.54	< −0.46							
	Cr I	< 4.26	< −1.41							
	Cr II	< 3.92	< −1.75							
	Mn I	< 4.19	< −1.20							
	Mn II	< 4.87	< −0.52							
	Fe I	4.94	−2.56	0.15	8	+0.13	+0.13	−0.01	−0.04	+0.06
	Fe II	5.00	−2.50	0.13	6	+0.11	+0.05	+0.02	−0.10	+0.08
	Co I	< 5.16	< +0.24							
	Ni I	< 5.92	< −0.33							

star	species	log ϵ	[X/H]	σ_Σ	$N_{\rm lines}$	σ_N	σ_T	σ_g	σ_ξ	σ_W
M92/466	Ni II	< 5.12	< −1.13							
cont.	Zn I	< 4.63	< +0.03							
	Sr II	0.09	−2.88	0.15	1	+0.00	+0.11	+0.00	−0.04	+0.09
	Y II	< 1.27	< −0.97							
	Zr II	< 2.25	< −0.35							
	Ba II	< 0.69	< −1.44							
M92/B516	He I	< 11.36	< +0.37							
	C I	< 8.56	< +0.04							
	C II	< 9.50	< +0.98							
	N I	< 8.34	< +0.42							
	O I	< 9.16	< +0.33							
	Mg I	5.79	−1.79	0.22	2	+0.11	+0.18	−0.03	−0.02	+0.05
	Mg II	5.52	−2.06	0.08	4	+0.10	+0.00	+0.01	−0.01	+0.08
	Al II	< 7.21	< +0.74							
	Si II	< 6.53	< −1.02							
	Ca I	< 5.27	< −1.09							
	Ca II	< 6.37	< +0.01							
	Sc II	< 1.77	< −1.40							
	Ti II	3.20	−1.82	0.14	9	+0.17	+0.12	+0.01	−0.01	+0.08
	V I	< 5.65	< +1.65							
	V II	4.38	+0.38	0.21	1	+0.00	+0.08	+0.01	+0.00	+0.19
	Cr I	< 5.26	< −0.41							
	Cr II	< 4.51	< −1.16							
	Mn I	5.35	−0.04	0.72	1	+0.00	+0.61	−0.17	−0.04	+0.33
	Mn II	< 5.47	< +0.08							
	Fe I	5.69	−1.81	0.24	4	+0.21	+0.20	−0.03	−0.01	+0.09
	Fe II	5.48	−2.02	0.10	6	+0.09	+0.07	+0.01	−0.05	+0.07
	Ni I	< 6.71	< +0.46							
	Ni II	< 5.47	< −0.78							
	Sr II	< 1.83	< −1.14							
	Y II	< 2.40	< +0.16							
	Zr II	< 3.12	< +0.52							
	Ba II	< 2.41	< +0.28							
M92/B527	He I	11.10	+0.11	0.33	1	+0.00	−0.30	+0.04	+0.00	+0.12
	C I	< 8.56	< +0.04							
	C II	< 9.47	< +0.95							
	N I	< 8.43	< +0.51							
	O I	< 9.01	< +0.18							
	Mg I	5.59	−1.99	0.27	1	+0.00	+0.26	−0.03	+0.00	+0.06
	Mg II	5.56	−2.02	0.36	2	+0.36	+0.01	−0.00	−0.01	+0.05
	Al I	4.97	−1.50	0.27	1	+0.00	+0.26	−0.03	+0.00	+0.07
	Al II	< 7.14	< +0.67							
	Si I	< 6.86	< −0.69							
	Si II	5.88	−1.67	0.13	2	+0.03	−0.08	+0.03	+0.00	+0.09
	Ca I	< 5.51	< −0.85							
	Ca II	4.14	−2.22	0.33	2	+0.10	+0.31	−0.04	−0.01	+0.03
	Sc II	< 1.98	< −1.19							
	Ti II	3.39	−1.63	0.18	3	+0.06	+0.17	+0.01	−0.01	+0.07
	V II	< 3.83	< −0.17							
	Cr I	< 5.46	< −0.21							
	Cr II	< 4.31	< −1.36							
	Mn I	< 5.56	< +0.17							
	Mn II	< 5.70	< +0.31							
	Fe I	< 6.06	< −1.44							
	Fe II	5.39	−2.11	0.14	6	+0.13	+0.12	+0.02	−0.03	+0.08
	Ni II	< 5.34	< −0.91							
	Sr II	< 1.80	< −1.17							
	Y II	< 2.29	< +0.05							
	Zr II	< 3.04	< +0.44							
	Ba II	< 2.76	< +0.63							
M92/IV-17	He I	11.18	+0.19	0.52	2	+0.40	−0.26	+0.05	−0.01	+0.19
	C I	< 8.69	< +0.17							
	O I	< 8.85	< +0.02							

star	species	$\log\epsilon$	[X/H]	σ_Σ	$N_{\rm lines}$	σ_N	σ_T	σ_g	σ_ξ	σ_W
M92/IV-17	Na I	< 5.72	< -0.61							
cont.	Mg I	5.45	-2.13	0.26	2	$+0.06$	$+0.23$	-0.02	-0.02	$+0.10$
	Mg II	5.58	-2.00	0.08	1	$+0.00$	$+0.01$	$+0.01$	-0.05	$+0.06$
	Al II	< 7.26	$< +0.79$							
	Si II	< 6.71	< -0.84							
	Ca I	< 6.67	$< +0.31$							
	Ca II	< 6.62	$< +0.26$							
	Sc II	< 2.91	< -0.26							
	Ti II	< 3.69	< -1.33							
	Cr I	< 6.01	$< +0.34$							
	Cr II	< 4.57	< -1.10							
	Mn II	< 6.15	$< +0.76$							
	Fe I	< 6.07	< -1.43							
	Fe II	5.22	-2.28	0.19	4	$+0.19$	$+0.09$	$+0.01$	-0.11	$+0.11$
	Ni I	< 7.02	$< +0.77$							
	Ni II	< 7.36	$< +1.11$							
	Y II	< 2.51	$< +0.27$							
	Ba II	< 2.59	$< +0.46$							
M92/IV-27	He I	< 12.65	$< +1.66$							
	C I	< 7.81	< -0.71							
	O I	< 8.50	< -0.33							
	Na I	3.79	-2.54	0.13	1	$+0.00$	$+0.07$	-0.01	-0.02	$+0.11$
	Mg I	5.83	-1.75	0.20	3	$+0.20$	$+0.07$	-0.01	-0.12	$+0.06$
	Mg II	5.70	-1.88	0.07	1	$+0.00$	-0.03	$+0.02$	-0.03	$+0.05$
	Si I	< 7.09	< -0.46							
	Si II	5.95	-1.60	0.12	1	$+0.00$	-0.02	$+0.02$	-0.03	$+0.11$
	S I	< 7.32	< -0.01							
	Ca I	< 4.97	< -1.39							
	Ca II	< 5.72	< -0.64							
	Sc II	< 1.69	< -1.48							
	Ti I	< 4.50	< -0.52							
	Ti II	3.06	-1.96	0.09	8	$+0.16$	$+0.04$	$+0.02$	-0.04	$+0.06$
	V I	< 3.96	< -0.04							
	V II	< 3.97	< -0.03							
	Cr I	< 3.88	< -1.79							
	Cr II	< 3.91	< -1.76							
	Mn I	< 4.49	< -0.90							
	Mn II	< 5.32	< -0.07							
	Fe I	5.02	-2.48	0.14	6	$+0.22$	$+0.08$	-0.01	-0.03	$+0.10$
	Fe II	5.11	-2.39	0.08	12	$+0.17$	$+0.03$	$+0.02$	-0.04	$+0.08$
	Ni I	< 6.09	< -0.16							
	Ni II	< 6.07	< -0.18							
	Zn I	< 4.22	< -0.38							
	Y II	< 1.00	< -1.24							
	Zr II	< 2.17	< -0.43							
	Ba II	< 0.20	< -1.93							
	La II	< 4.84	$< +3.67$							
M92/VI-10	He I	< 12.34	$< +1.35$							
	C I	< 7.79	< -0.73							
	O I	< 8.19	< -0.64							
	Na I	< 5.77	< -0.56							
	Mg I	5.45	-2.13	0.14	3	$+0.11$	$+0.08$	-0.01	-0.07	$+0.03$
	Mg II	5.36	-2.22	0.07	3	$+0.03$	-0.01	$+0.02$	-0.03	$+0.07$
	Si I	< 7.50	< -0.05							
	Si II	5.53	-2.02	0.07	1	$+0.00$	-0.01	$+0.02$	-0.02	$+0.06$
	Ca I	3.84	-2.52	0.14	1	$+0.00$	$+0.12$	-0.01	-0.05	$+0.05$
	Ca II	< 5.82	< -0.54							
	Sc II	0.60	-2.57	0.10	1	$+0.00$	$+0.07$	$+0.02$	-0.02	$+0.07$
	Ti I	< 4.53	< -0.49							
	Ti II	2.89	-2.13	0.08	12	$+0.13$	$+0.06$	$+0.02$	-0.03	$+0.05$
	V II	< 3.88	< -0.12							
	Cr I	< 4.15	< -1.52							
	Cr II	< 4.03	< -1.64							
	Mn I	< 4.84	< -0.55							

star	species	log ϵ	[X/H]	σ_Σ	$N_{\rm lines}$	σ_N	σ_T	σ_g	σ_ξ	σ_W
M92/VI-10	Mn II	< 4.91	< −0.48							
cont.	Fe I	4.79	−2.71	0.13	7	+0.10	+0.11	−0.01	−0.03	+0.08
	Fe II	4.88	−2.62	0.09	6	+0.11	+0.04	+0.02	−0.06	+0.06
	Co I	< 5.05	< +0.13							
	Ni I	< 5.20	< −1.05							
	Ni II	< 6.28	< +0.03							
	Zn I	< 4.17	< −0.43							
	Sr II	-0.10	−3.07	0.14	1	+0.00	+0.09	+0.01	−0.02	+0.11
	Y II	< 1.04	< −1.20							
	Zr I	< 4.38	< +1.78							
	Zr II	3.36	+0.76	0.08	1	+0.00	+0.04	+0.01	−0.02	+0.07
	Ba II	< 0.43	< −1.70							
M92/X-22	He I	< 12.80	< +1.81							
	C I	< 7.73	< −0.79							
	O I	< 8.35	< −0.48							
	Na I	< 3.97	< −2.36							
	Mg I	5.61	−1.97	0.18	3	+0.16	+0.07	−0.00	−0.12	+0.05
	Mg II	5.52	−2.06	0.06	1	+0.00	−0.01	+0.01	−0.03	+0.05
	Si I	< 7.16	< −0.39							
	Si II	5.59	−1.96	0.16	2	+0.13	−0.01	+0.03	−0.01	+0.09
	Ca I	< 5.09	< −1.27							
	Ca II	< 5.71	< −0.65							
	Sc II	1.09	−2.08	0.13	1	+0.00	+0.04	+0.02	−0.03	+0.12
	Ti I	< 4.50	< −0.52							
	Ti II	2.91	−2.11	0.11	8	+0.21	+0.05	+0.02	−0.05	+0.07
	V I	< 4.26	< +0.26							
	V II	< 4.24	< +0.24							
	Cr I	< 3.95	< −1.72							
	Cr II	< 3.94	< −1.73							
	Mn I	< 4.63	< −0.76							
	Mn II	< 5.53	< +0.14							
	Fe I	4.84	−2.66	0.12	5	+0.08	+0.09	−0.00	−0.06	+0.09
	Fe II	4.89	−2.61	0.10	8	+0.13	+0.03	+0.02	−0.07	+0.07
	Ni I	< 6.20	< −0.05							
	Ni II	< 6.42	< +0.17							
	Zn I	< 4.64	< +0.04							
	Y II	< 1.04	< −1.20							
	Zr I	< 3.86	< +1.26							
	Zr II	< 2.42	< −0.18							
	Ba II	< 0.34	< −1.79							
	La II	< 4.82	< +3.65							
M92/XII-1	He I	< 12.59	< +1.60							
	C I	< 7.78	< −0.74							
	O I	< 8.25	< −0.58							
	Na I	4.07	−2.26	0.15	2	+0.06	+0.07	−0.01	−0.05	+0.10
	Mg I	5.81	−1.77	0.26	3	+0.08	+0.07	−0.00	−0.24	+0.05
	Mg II	5.60	−1.98	0.07	1	+0.00	−0.03	+0.02	−0.04	+0.04
	Si I	< 6.98	< −0.57							
	Si II	5.76	−1.79	0.24	2	+0.20	−0.03	+0.03	−0.03	+0.12
	S I	< 7.03	< −0.30							
	Ca I	< 4.67	< −1.69							
	Ca II	< 5.72	< −0.64							
	Sc II	1.48	−1.69	0.10	1	+0.00	+0.05	+0.02	−0.02	+0.08
	Ti I	< 4.20	< −0.82							
	Ti II	3.16	−1.86	0.11	9	+0.17	+0.05	+0.03	−0.06	+0.07
	V I	< 3.85	< −0.15							
	V II	< 3.83	< −0.17							
	Cr I	< 3.88	< −1.79							
	Cr II	< 3.80	< −1.87							
	Mn I	< 4.34	< −1.05							
	Mn II	< 5.30	< −0.09							
	Fe I	5.20	−2.30	0.19	7	+0.34	+0.09	−0.00	−0.08	+0.08
	Fe II	5.16	−2.34	0.13	7	+0.17	+0.03	+0.03	−0.10	+0.06
	Ni I	< 5.92	< −0.33							

star	species	log ϵ	[X/H]	σ_Σ	$N_{\rm lines}$	σ_N	σ_T	σ_g	σ_ξ	σ_W
M92/XII-1	Ni II	< 6.00	< −0.25							
cont.	Zn I	< 4.17	< −0.43							
	Y II	< 0.90	< −1.34							
	Zr II	< 2.15	< −0.45							
	Ba II	< 0.02	< −2.11							
	La II	< 4.02	< +2.85							
	Ce II	< 1.63	< +0.05							
	Eu II	< 0.62	< +0.11							
M92/XII-9	He I	< 12.36	< +1.37							
	C I	< 7.92	< −0.60							
	O I	< 8.34	< −0.49							
	Na I	< 5.07	< −1.26							
	Mg I	6.04	−1.54	0.19	4	+0.17	+0.08	−0.01	−0.13	+0.06
	Mg II	< 6.95	< −0.63							
	Si I	< 7.51	< −0.04							
	Si II	< 6.06	< −1.49							
	S I	< 7.28	< −0.05							
	Ca I	< 4.97	< −1.39							
	Ca II	< 5.96	< −0.40							
	Sc II	< 1.89	< −1.28							
	Ti I	< 4.70	< −0.32							
	Ti II	3.26	−1.76	0.10	6	+0.13	+0.06	+0.02	−0.05	+0.06
	V I	< 4.38	< +0.38							
	V II	< 4.14	< +0.14							
	Cr I	< 4.29	< −1.38							
	Cr II	< 4.08	< −1.59							
	Mn I	< 4.88	< −0.51							
	Mn II	< 5.35	< −0.04							
	Fe I	5.42	−2.08	0.14	7	+0.12	+0.10	−0.01	−0.07	+0.08
	Fe II	5.31	−2.19	0.12	7	+0.10	+0.04	+0.02	−0.10	+0.06
	Ni I	< 6.42	< +0.17							
	Ni II	< 6.40	< +0.15							
	Zn I	< 4.41	< −0.19							
	Y II	< 1.04	< −1.20							
	Zr II	< 2.49	< −0.11							
	Ba II	< 0.48	< −1.65							
	La II	< 4.88	< +3.71							
N288/B16	He I	< 10.72	< −0.27							
	C I	< 10.58	< +2.06							
	C II	< 9.03	< +0.51							
	N I	< 10.29	< +2.37							
	N II	9.51	+1.59	0.36	1	+0.00	−0.10	+0.05	−0.09	+0.33
	O I	< 10.02	< +1.19							
	O II	< 11.62	< +2.79							
	Na I	< 8.99	< +2.66							
	Mg I	< 8.70	< +1.12							
	Mg II	6.23	−1.35	0.18	4	+0.24	+0.04	−0.01	−0.04	+0.18
	Al I	< 9.95	< +3.48							
	Al II	< 7.88	< +1.41							
	Al III	< 9.07	< +2.60							
	Si I	< 11.59	< +4.04							
	Si II	6.78	−0.77	0.15	5	+0.24	−0.01	+0.01	−0.04	+0.14
	Si III	< 9.78	< +2.23							
	P I	< 10.07	< +4.62							
	P II	7.25	+1.80	0.12	11	+0.25	−0.05	+0.02	−0.04	+0.18
	P III	< 9.56	< +4.11							
	S I	< 10.78	< +3.45							
	S II	< 8.29	< +0.96							
	S III	< 11.15	< +3.82							
	Ca I	< 10.42	< +4.06							
	Ca II	< 6.83	< +0.47							
	Sc II	< 5.90	< +2.73							
	Ti II	5.30	+0.28	0.16	5	+0.20	+0.11	−0.00	−0.02	+0.13
	V I	< 10.47	< +6.47							

star	species	log ϵ	[X/H]	σ_Σ	$N_{\rm lines}$	σ_N	σ_T	σ_g	σ_ξ	σ_W
N288/B16	V II	7.50	+3.50	0.36	1	+0.00	+0.13	−0.01	−0.07	+0.33
cont.	V III	< 9.95	< +5.95							
	Cr I	< 9.86	< +4.19							
	Cr II	7.31	+1.64	0.30	1	+0.00	+0.09	+0.01	−0.05	+0.28
	Cr III	< 10.72	< +5.05							
	Mn I	< 9.54	< +4.15							
	Mn II	< 7.42	< +2.03							
	Fe I	8.22	+0.72	0.29	3	+0.24	+0.15	−0.03	−0.05	+0.24
	Fe II	7.94	+0.44	0.09	104	+0.30	+0.03	+0.01	−0.08	+0.16
	Fe III	< 10.28	< +2.78							
	Co I	< 10.70	< +5.78							
	Co II	< 7.97	< +3.05							
	Ni I	< 9.03	< +2.78							
	Ni II	< 8.14	< +1.89							
	Zn I	< 8.58	< +3.98							
	Sr II	< 6.11	< +3.14							
	Y II	< 6.46	< +4.22							
	Zr II	< 6.54	< +3.94							
	Ba II	< 5.97	< +3.84							
N288/B22	He I	< 10.35	< −0.64							
	C I	< 10.80	< +2.28							
	C II	< 9.15	< +0.63							
	N I	< 10.74	< +2.82							
	N II	< 10.56	< +2.64							
	O I	< 9.85	< +1.02							
	O II	< 11.60	< +2.77							
	Na I	< 9.23	< +2.90							
	Mg I	< 9.48	< +1.90							
	Mg II	6.45	−1.13	0.17	2	+0.01	+0.05	−0.02	−0.06	+0.15
	Al I	< 10.59	< +4.12							
	Al II	< 7.72	< +1.25							
	Al III	< 8.84	< +2.37							
	Si I	< 11.76	< +4.21							
	Si II	6.95	−0.60	0.16	5	+0.24	−0.01	−0.00	−0.06	+0.16
	Si III	< 10.03	< +2.48							
	P I	< 10.12	< +4.67							
	P II	7.44	+1.99	0.12	20	+0.35	−0.05	+0.02	−0.05	+0.17
	P III	< 9.64	< +4.19							
	S I	< 11.03	< +3.70							
	S II	< 8.63	< +1.30							
	S III	< 10.73	< +3.40							
	Ca I	< 11.11	< +4.75							
	Ca II	< 7.14	< +0.78							
	Sc II	< 6.40	< +3.23							
	Ti I	< 11.44	< +6.42							
	Ti II	5.23	+0.21	0.71	2	+0.59	+0.11	+0.00	−0.05	+0.38
	Ti III	< 9.94	< +4.92							
	V I	< 11.04	< +7.04							
	V II	7.63	+3.63	0.23	1	+0.00	+0.13	−0.01	−0.04	+0.19
	V III	< 10.11	< +6.11							
	Cr I	< 10.17	< +4.50							
	Cr II	7.14	+1.47	0.26	3	+0.14	+0.13	+0.00	−0.08	+0.27
	Cr III	< 10.81	< +5.14							
	Mn I	< 10.05	< +4.66							
	Mn II	< 7.74	< +2.35							
	Mn III	< 10.91	< +5.52							
	Fe I	9.76	+2.26	0.35	1	+0.00	+0.18	−0.03	−0.04	+0.29
	Fe II	8.16	+0.66	0.11	117	+0.32	+0.05	+0.00	−0.09	+0.18
	Fe III	< 10.24	< +2.74							
	Co I	< 12.00	< +7.08							
	Co II	< 8.73	< +3.81							
	Ni I	< 10.47	< +4.22							
	Ni II	< 7.86	< +1.61							
	Zn I	< 9.06	< +4.46							
	Sr II	< 6.68	< +3.71							

star	species	log ϵ	[X/H]	σ_Σ	$N_{\rm lines}$	σ_N	σ_T	σ_g	σ_ξ	σ_W
N288/B22	Y II	4.77	+2.53	0.22	1	+0.00	+0.12	−0.01	−0.03	+0.18
cont.	Zr II	< 7.26	< +4.66							
	Ba II	< 6.20	< +4.07							
N288/B186	He I	9.89	−1.10	0.19	1	+0.00	−0.10	+0.04	−0.01	+0.16
	C I	< 10.10	< +1.58							
	C II	< 8.71	< +0.19							
	N I	< 9.77	< +1.85							
	N II	< 10.22	< +2.30							
	O I	< 9.09	< +0.26							
	O II	< 11.25	< +2.42							
	Na I	< 8.39	< +2.06							
	Mg I	< 7.97	< +0.39							
	Mg II	6.13	−1.45	0.11	4	+0.10	+0.03	−0.01	−0.01	+0.14
	Al I	< 8.43	< +1.96							
	Al II	< 7.02	< +0.55							
	Al III	< 8.82	< +2.35							
	Si I	< 10.83	< +3.28							
	Si II	6.20	−1.35	0.09	4	+0.10	−0.01	+0.01	−0.01	+0.12
	Si III	< 9.69	< +2.14							
	P I	< 9.18	< +3.73							
	P II	6.83	+1.38	0.12	4	+0.10	−0.05	+0.03	−0.01	+0.14
	P III	< 9.16	< +3.71							
	S I	< 9.94	< +2.61							
	S II	< 8.14	< +0.81							
	S III	< 10.87	< +3.54							
	Ca I	< 9.45	< +3.09							
	Ca II	< 6.56	< +0.20							
	Sc II	< 4.86	< +1.69							
	Ti II	5.34	+0.32	0.13	16	+0.23	+0.11	−0.00	−0.00	+0.13
	Ti III	< 9.92	< +4.90							
	V II	< 6.95	< +2.95							
	Cr I	< 8.84	< +3.17							
	Cr II	< 6.22	< +0.55							
	Cr III	< 10.31	< +4.64							
	Mn I	< 9.92	< +4.53							
	Mn II	< 7.00	< +1.61							
	Fe I	7.90	+0.40	0.19	5	+0.18	+0.14	−0.03	+0.00	+0.16
	Fe II	7.93	+0.43	0.04	144	+0.24	+0.02	+0.01	−0.02	+0.12
	Fe III	< 9.77	< +2.27							
	Co I	< 9.73	< +4.81							
	Co II	< 7.50	< +2.58							
	Ni I	< 9.16	< +2.91							
	Ni II	< 7.55	< +1.30							
	Zn I	< 7.14	< +2.54							
	Sr II	< 5.57	< +2.60							
	Y II	< 5.56	< +3.32							
	Zr II	< 6.18	< +3.58							
	Ba II	< 5.00	< +2.87							
N288/302	He I	< 9.63	< −1.36							
	C I	< 10.57	< +2.05							
	C II	< 8.37	< −0.15							
	N I	< 10.31	< +2.39							
	N II	10.27	+2.35	0.13	1	+0.00	−0.09	+0.03	−0.03	+0.09
	N III	< 16.19	< +8.27							
	O I	< 9.43	< +0.60							
	O II	10.13	+1.30	0.27	1	+0.00	−0.10	+0.04	−0.01	+0.25
	Na I	< 8.66	< +2.33							
	Mg I	< 9.17	< +1.59							
	Mg II	6.16	−1.41	0.09	4	+0.07	+0.04	−0.01	−0.01	+0.12
	Al I	< 10.45	< +3.98							
	Al II	< 7.01	< +0.54							
	Al III	< 8.38	< +1.91							
	Si I	< 11.58	< +4.03							

star	species	log ϵ	[X/H]	σ_Σ	$N_{\rm lines}$	σ_N	σ_T	σ_g	σ_ξ	σ_W
N288/302	Si II	6.44	−1.11	0.33	4	+0.55	+0.01	−0.00	−0.01	+0.12
cont.	Si III	< 9.01	< +1.46							
	P I	< 9.96	< +4.51							
	P II	7.12	+1.67	0.08	21	+0.31	−0.03	+0.01	−0.02	+0.13
	P III	< 8.84	< +3.39							
	S I	< 10.20	< +2.87							
	S II	< 7.87	< +0.54							
	S III	< 9.93	< +2.60							
	Ca II	< 7.28	< +0.92							
	Sc II	< 5.38	< +2.21							
	Ti II	6.04	+1.02	0.28	1	+0.00	+0.16	−0.03	+0.01	+0.23
	Ti III	< 9.13	< +4.11							
	V I	< 10.39	< +6.39							
	V II	7.96	+3.96	0.17	1	+0.00	+0.10	−0.01	−0.01	+0.14
	V III	< 9.32	< +5.32							
	Cr I	< 9.49	< +3.82							
	Cr II	6.54	+0.87	0.23	5	+0.38	+0.09	−0.01	−0.03	+0.16
	Cr III	< 10.17	< +4.50							
	Mn I	< 9.24	< +3.85							
	Mn II	7.41	+2.02	0.19	1	+0.00	+0.12	+0.00	+0.00	+0.15
	Mn III	< 9.92	< +4.53							
	Fe I	9.01	+1.51	0.23	6	+0.27	+0.16	−0.04	−0.02	+0.21
	Fe II	8.32	+0.82	0.07	194	+0.56	+0.05	−0.00	−0.02	+0.14
	Fe I	8.13	+0.63	0.22	2	+0.11	−0.06	+0.03	−0.03	+0.17
	Co II	< 7.64	< +2.72							
	Ni I	< 9.58	< +3.33							
	Ni II	< 7.35	< +1.10							
	Ni III	< 10.99	< +4.74							
	Zn I	< 8.27	< +3.67							
	Sr II	< 5.93	< +2.96							
	Y II	5.67	+3.43	0.88	2	+0.83	+0.10	−0.02	−0.08	+0.26
	Zr II	< 6.23	< +3.63							
	Ba II	< 5.60	< +3.47							

Appendix B THuCIDIDES

The original proposal for this thesis project included the design and construction of a high-resolution, high-efficiency echelle spectrograph for the Hale 200-inch telescope. This instrument, called "THuCIDIDES," would have permitted us to observe the brighter cluster BHBs from Palomar and thus greatly increase our sample size. Funding for this project was not available, unfortunately, and it was never built, but the basic optical and mechanical design was completed, so we include a description of the system specifications and component layout in this Appendix to the thesis.

B.1 Abstract

We describe the operating parameters and initial design of a new spectrograph proposed for the 200-inch Hale Telescope at Palomar Observatory. The instrument, whose working name is THuCIDIDES (**T**wo **Hu**ndred-inch **C**assegrain **I**mage-**D**eblurred **I**nterchangable **D**isperser/**E**chelle **S**pectrograph), features high system efficiency and multiple modes of operation, including low and intermediate-resolution long slit and multi-slit capability over 12.5×3 arcmin fields, and a cross-dispersed echelle mode covering 3800–8500 Å at $R = 20000$ (with a 1.2 arcsec slit) up to $R = 60000$ (with an image slicer). A 4096×4096 pixel CCD serves as the detector. The quasi-Littrow echelle configuration and use of a prism cross-disperser results in high system efficiency, estimated at $\sim 14\%$. The compact design permits mounting in the Cassegrain ring plane, to reduce susceptibility to flexure. An optional fast-guiding tilt mirror provides modest improvement to seeing FWHM and slit throughput.

B.2 Rationale

The facilities for high-resolution spectroscopy at the Palomar 200-inch telescope are presently rather limited. The only instrument capable of spectral resolutions around $R = 20000$ over a wide wavelength range is the East Arm Echelle Spectrograph (Libbrecht & Peri, 1995), which utilizes a fiber-optic conduit running from prime focus to a fixed-orientation optical bench, in order to eliminate flexure issues and maximize the wavelength stability of the

spectrograph. Consequently, due to lossy fiber coupling, it suffers from poor overall efficiency ($\eta < 2\%$), and the single fiber does not permit a sky background channel. Low-order grating and slit devices like the Double Spectrograph (Oke & Gunn, 1982), although efficient, are limited to $R < 5000$. Many of the scientific pursuits of Palomar observers — stellar abundance work, quasar absorption lines, and globular cluster dynamics — would therefore benefit greatly from the availability of a high-efficiency, high-resolution Cassegrain echelle spectrograph, similar to those currently in operation on the LCO 100-inch (Shectman, 1988), Palomar 60-inch (McCarthy, 1988), and the McDonald 2.1-meter (McCarthy *et al.*, 1993) telescopes.

The underlying design philosophy for the echelle configuration emphasizes simplicity and maximum throughput. Specific design choices stemming from these priorities include use of a single lens system in double-pass as both collimator and camera, a prism (instead of a grating) as the cross-disperser, and an optional fast tip-tilt guider. Details of these subsystems will be discussed below.

Although this proposed instrument was originally conceived solely as a cross-dispersed echelle, it became apparent that other modes of operation could be incorporated into the design at no penalty to the echelle performance. The large format of the CCD detector and the $f/16 \rightarrow f/3.3$ reimaging configuration will permit fields as large as 12.5×3 arcmin (300×75 mm at Cassegrain focus) with either a single long slit or multi-slit mask. In order to accommodate the low-resolution requirements of most long/multi-slit work, the spectrograph follows a modular design, with interchangeable 'bolt-on' disperser, slit, and reimaging packages, which are selected according to the spectral and spatial coverage desired for a given observing run.

B.3 Performance specifications

Basic Optical Parameters

Collimator EFL:	2180 mm
Camera EFL:	455 mm
Collimated beam diameter:	136 mm
Estimated system efficiency:	$\eta = 14\%$ at 6000 Å

Echelle Mode

Grating:	12 × 6 inch 79.1 gr/mm R2 grating
Cross-disperser:	LF5 prism, 45° apex angle
Spectral range:	3800–8500 Å, continuous coverage to 7500 Å, 33 orders
Resolution:	$R\phi = 22400$, 5.4 pixels/arcsec nominal $R = 18700$ (16 $\mathrm{km\,s^{-1}}$) with 1.2 arcsec slit (6.5 pixel res element) maximum $R = 60790$ (4.9 $\mathrm{km\,s^{-1}}$) with 0.37 arcsec slit (2 pixel res element)
Slit length:	8.4 arcsec (45 pixels) nominal
Order spacing:	6 pixels minimum interorder gap

Long Slit Mode

Gratings:	300 gr/mm, 600 gr/mm, 1200 gr/mm from Norris Spectrograph
Spectral resolution and range:	$\Delta\lambda = 7.1$ Å over 4490 Å with 300 gr/mm and 1.2 arcsec slit $\Delta\lambda = 1.7$ Å over 1070 Å with 1200 gr/mm
Maximum slit length:	12.5 arcmin (300 mm at $f/16$)
Spatial scale:	0.19 arcsec/pixel

Multi-slit Mode

Spectral resolution and range:	same as long slit above
Field size:	12.5 × 3 arcmin, 300 × 75 mm masks at $f/16$
Slit width:	1.5 arcsec = 0.6 mm on mask

B.4 Basic component layout

Figure B.1 shows top-view and side-view plans of Thucidides, depicting the system in its short-slit echelle mode. Light at $f/16$ enters through the Cassegrain aperture and is reflected by feed mirror *FM* (optionally tip-tilt guided) into the Cassegrain ring plane, where it is brought to a focus at the slit focal plane *SP*. Reflective slitjaws feed a video guider camera *GC* via a fold mirror (not shown), providing feedback to the tip-tilt system or indigenous telescope guiding. The $f/16$ beam is then collimated by a 240 mm Nikon lens *CL*, bent by *M1* and then reimaged at $f/3.3$ onto an intermediate focal plane *IP* by a 50 mm Nikon lens *RL*. Additional masking of stray light can take place at *IP*. After passing through *IP*, the light is reflected by a small fold mirror *M3* to the main collimator/camera lens *CCL* and is collimated for entry into the disperser unit, which contains the 79.1 gr/mm R2 grating *EG* and double-pass cross-dispersing prism *DP* (45° apex angle of LF5 glass). Exiting the disperser, the light is refocused by *CCL* on to the detector plane, where the spectral image is formed on the detector *CCD*.

Using the collimator/camera in double pass in this fashion (a technique shared by many other echelles) affords a number of advantages. Most notably, the small size of the reimaged

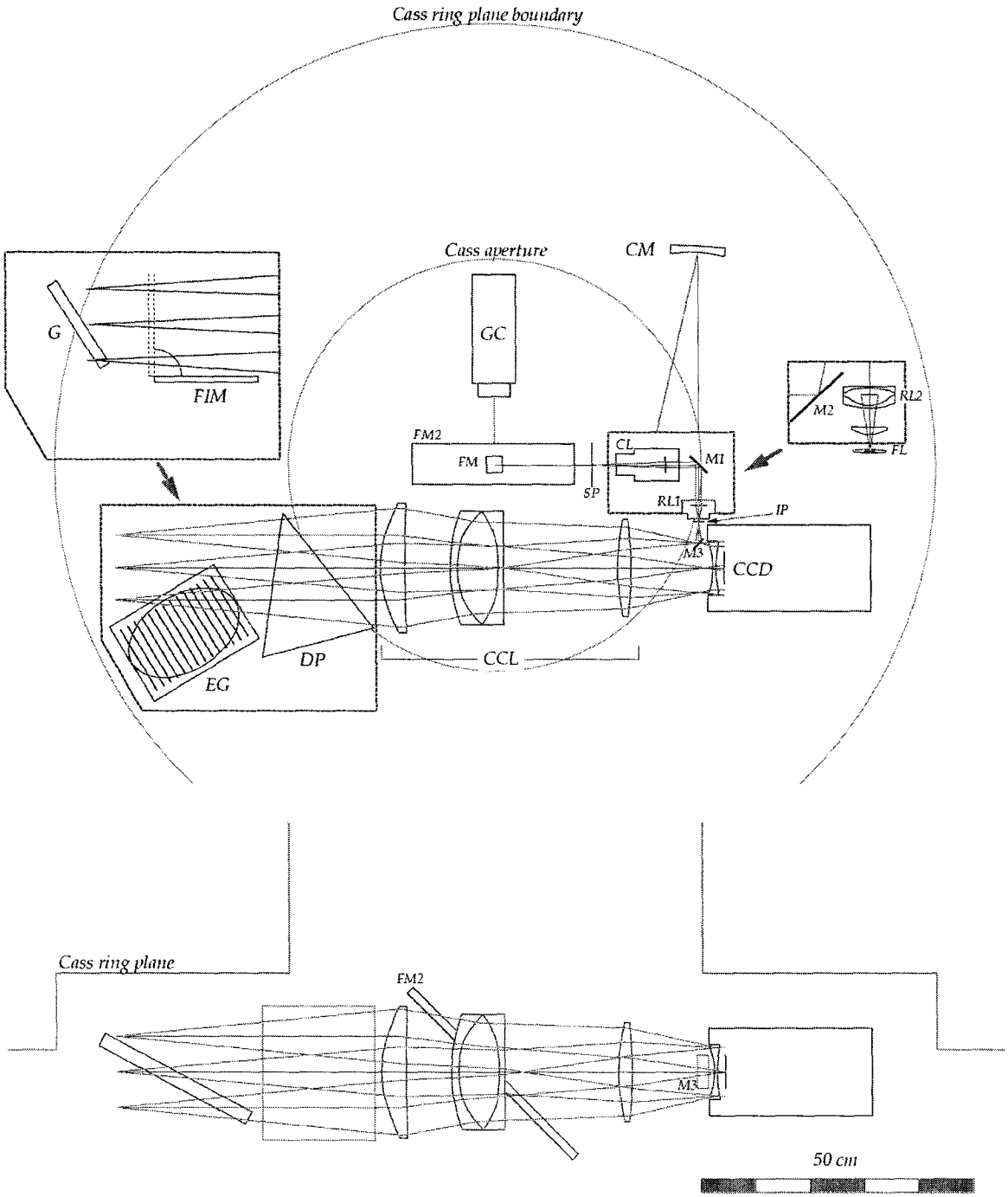

Figure B.1: Top and side views of the echelle spectrograph optomechanical layout.

field at the intermediate focus permits the angle between disperser input and output beams (2γ in echelle nomenclature) to be very small, for smaller prism size and improved efficiency, and the camera can be placed immediately following the disperser exit, before the highly-dispersed output beam has grown to enormous proportions. The design is also relatively compact, since the 2-meter EFL of the collimator does not have to be physically realized, and will mount on the uppermost Cassegrain ring plane, simplifying the mechanical structure of the device and keeping flexure to a minimum.

For long-slit or multi-slit mode, new reimaging and disperser packages, represented by the broken-line boxes, are inserted into the system in place of the echelle reimager and grating/cross-disperser units. A larger feed mirror *FM2* illuminates a long slit or slit mask at *SP*. The beam is reflected by *M2* immediately after the slit plane and sent to a large off-axis spherical collimating mirror *CM* of focal length 510 mm. Collimated beams from *CM* converge towards a pupil, where the lens system *RL2* reimages them at $f/3.3$ onto *IP*. *RL2* will have to be a custom optical system (not yet designed) to handle the wide field requirements, and a field lens *FL* at *IP* will be necessary to maintain telecentricity downstream of *IP*. The echelle disperser package will be exchanged for a low-order grating *G*, including a flip-in mirror *FIM* for slit alignment imaging. We may borrow gratings from Palomar's multifiber Norris spectrograph, mounted in one of the spare motorized grating mounts originally intended for the Double Spectrograph.

Other mode variations are possible. An image slicer can be placed immediately after the slit plane for increased spectral resolution, since the pixel sampling permits effective slit widths as small as 0.4 arcsec. A coronagraphic mode might be implemented by placing an occulting disk at *SP*, a Lyot stop at the pupil position in the small collimated beam between *CL* and *RL*, and a slit at *IP*. With an interference filter just before *RL2* and an alternative echelle disperser package without the prism, a single-order long-slit echelle mode could also prove useful.

B.5 Subsystems

B.5.1 Fast tip-tilt guiding on slit

The Palomar telescopes are equipped with a standardized video guider system which will keep stars or other targets centered on the slit against slow secular changes and pointing

drift, but some advantage might be gained by also including a separate fast-guiding subsystem just upstream of the spectrograph slit. As part of a separate project, a team under J. K. McCarthy has placed a CCD device on a piezo-driven x-y stage, translating the chip in the focal plane under closed-loop feedback from a guide star on a photodiode quad cell. Tests of this system at the 200-inch Cassegrain station indicate that fast guiding at 20 Hz will remove a significant amount of the global tip-tilt component of the atmospheric seeing and wind shake, thereby improving the seeing disk FWHM by $\sim 20\%$ under typical conditions. If such a system were to be implemented by driving mirror *FM* via feedback from the slitjaw image, the slit throughput could be improved by a significant amount, and the extent of the target image along the slit length (the spatial axis) would be reduced as well, minimizing contamination of the sky background channels and pixel readout noise. Such a system could be easily added after the instrument is first commissioned with a fixed mirror at *FM*.

B.5.2 Collimator/camera lens

The lens system labelled *CCL* in Figure B.1 is used in double-pass, as both the collimator and the spectrograph camera. This six-element all-spherical design was adapted from the new Epps camera for the Palomar Double Spectrograph, simplified and optimized for this application using the *Code V* raytracing package. The EFL of the composite lens is 455 mm. Lens element parameters are listed in Table B.1, with glass types from the O'Hara catalog. The calcium fluoride element (#3) is made the center element of a triplet in order to isolate it from atmospheric humidity. The field flattener (#6) doubles as the CCD dewar window.

This lens system produces good spot sizes from collimated light over the entire $(61\ \mathrm{mm})^2$ area of the CCD for most of the desired spectral range. Polychromatic spot sizes ($\lambda = 4000$–8000 Å) are 9μ (RMS diameter) at chip center and 21μ at the corners. The variation of spot size as a function of λ is plotted in Figure B.2, and raytraced spot diagrams for field center, edge, and corner are shown in Figure B.3. Performance degrades sharply below 4000 Å, unfortunately, but an additional lens element and/or more sophisticated design revisions may be able to remedy this weakness.

Table B.1: Optical elements of the collimator/camera lens.

element	R_1 (mm)	R_2 (mm)	center thickness (mm)	glass
1	231.94	706.37	30.00	FPL 51
			107.73	air
2	307.61	135.49	10.00	LAL 7
3	135.49	−212.37	70.00	CaF_2
4	−212.37	−1651.08	10.00	LAL 12
			244.64	air
5	225.75	−491.02	30.00	FPL 51
			99.39	air
6	−179.48	186.05	5.00	SiO_2
			20.00	air

B.5.3 Grating and cross-disperser

A 79.1 gr/mm echelle grating, measuring 12×6 inches, is already in hand (currently in use with the East Arm Echelle), and will serve as THuCIDIDES' primary dispersing element. The collimated beam diameter will completely fill but not overfill the projected grating surface area, so as not to lose light of the edge off the grating. The echellogram image format is well-matched to the available detector size. Thirty-three orders, from $m = 27$ to $m = 59$, will fit on the chip along the cross-dispersion axis, for a spectral coverage from 3800 to 8500 Å. The redmost part of the spectrum ($\lambda > 7500$ Å) will suffer from some wavelength coverage gaps, as the length of the free spectral range for orders $m \leq 29$ exceeds the chip width, but key spectral lines such as the O 7770 triplet will still be observable. By tilting the grating, orders further to the red or to the blue can be selected, but the camera's chromatic performance will deteriorate rapidly outside of the design range.

A Schott LF5 prism with apex angle 45° cross-disperses the echelle orders. We chose a prism rather than a grating for this task in order to achieve greater system efficiency, and to have more regular spacing of echelle orders on the detector. LF5 is an excellent glass for this purpose, as it combines low index, high dispersion, and good throughput even in the blue. The cross-dispersion has been chosen to fit the entire wavelength range of interest on to the detector, while still providing sufficient inter-order separation in the blue to prevent order overlap.

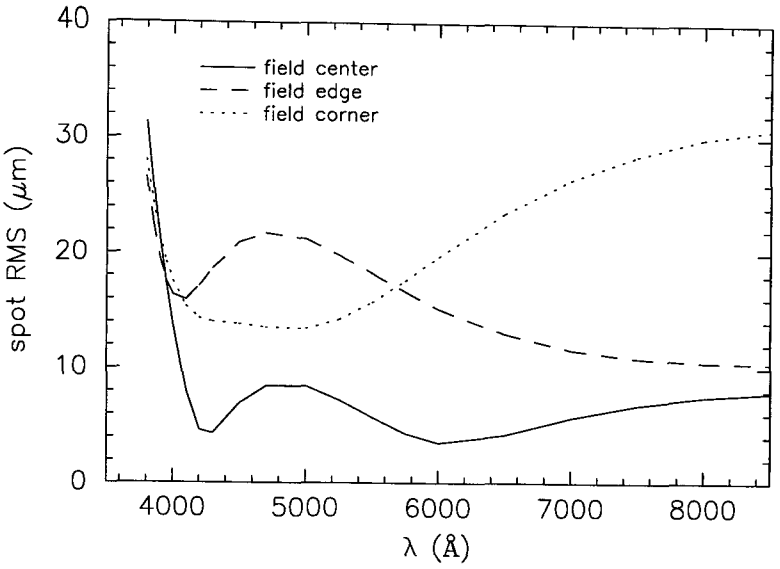

Figure B.2: Spot RMS as a function of λ for lens CCL in single-pass.

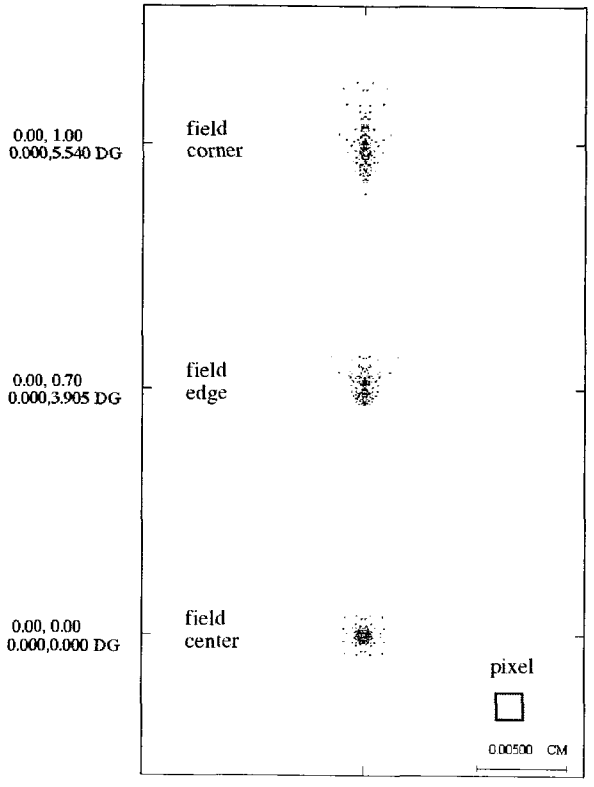

Figure B.3: Polychromatic spot diagrams for lens CCL in single-pass.

B.5.4 Detector

A 4096×4096 CCD with 15μ pixels, manufactured by Lockheed-Martin Fairchild, will be used as the THuCIDIDES detector. The device will be thinned and backside-illuminated for maximum quantum efficiency in the blue. The small pixel size will oversample the normal slit width (1.2 arcsec) by a factor of three, so for work at $R \simeq 20000$, on-chip binning may be desired for lower read noise and faster readout. (Alternatively, for higher-resolution tasks where some efficiency hit is acceptable, a narrow slit or image slicer may be employed.) A standard Palomar dewar will probably house the detector, and as mentioned in the introduction, readout electronics and control systems are yet to be decided upon.

Bibliography

Arp, H. C. 1955, AJ, 60, 317.

Arp, H. C. & Johnson, H. L. 1955, ApJ, 122, 171.

Baschek, B. 1975, in *Problems in stellar atmospheres and envelopes*, (New York: Springer-Verlag), 101.

Baschek, B., Holweger, H., & Traving, G. 1966, *Abhandlungen aus der Hamburger Sternwarte*, 8, 26.

Bidelman, W. P. 1960, PASP, 72, 24.

Bouvier, J., Forestini, M., & Allain, S. 1997, A&A, 326, 1023.

Brun, A. S., Turck-Chize, S., & Morel, P. 1998, ApJ, 506, 913.

Buonanno, R., Buscema, G., Corsi, C. E., Iannicola, G., & Fusi Pecci, F. 1983, A&AS, 51, 83.

Buonanno, R., Buscema, G., Corsi, C. E., Iannicola, G., Smriglio, F., & Fusi Pecci, F. 1983, A&AS, 53, 1.

Buonanno, R., Corsi, C. E., Fusi Pecci, F., Alcaino, G., & Liller, W. 1984, A&AS, 57, 75.

Buonanno, R., Corsi, C. E., & Fusi Pecci, F. 1985, A&A, 145, 97.

Buonanno, R., Corsi, C. E., Buzzoni, A., Cacciari, C., Ferraro, F. R., & Fusi Pecci, F. 1994, A&A, 290, 69.

Buonanno, R., Corsi, C. E., Bellazzini, M., Ferraro, F. R., & Fusi Pecci, F. 1997, AJ, 113, 706.

Caloi, V. 1999, A&A, 343, 904.

Catelan, M., Borissova, J., Sweigart, A. V., & Spassova, N., 1998, ApJ, 494, 265.

Cavallo, R. M. & Nagar, N. M. 2000, astro-ph 0002511.

Charbonneau, P., Tomczyk, S., Schou, J., & Thompson, M. J. 1998, ApJ, 496, 1015.

Cohen, J. G. & McCarthy, J. K. 1997, AJ, 113, 1353.

Corbard, T., Barthomieu, G., Morel, P., Provost, J., Schou, J., & Tomczyk, S. 1997, A&A, 324, 298.

Dorman, B., Rood, R. T., & O'Connell, R. W. 1993, ApJ, 419, 596.

Durrell, P. R. & Harris, W. E. 1993, AJ, 105, 1420.

Ferraro, F. R., Carretta, E., Corsi, C. E., Fusi Pecci, F., Cacciari, C., Buonanno, R., Paltrinieri, B., & Hamilton, D. 1997, A&A, 320, 757.

Ferraro, F. R., Messineo, M., Fusi Pecci, F., Depalo, M. A., Stranerio, O., Chieffi, A., & Limongi, M. 1999, AJ, 118, 1738.

Ferraro, F. R., Paltrinieri, B., Fusi Pecci, F., Cacciari, C., Dorman, B., Rood, R. T., Buonanno, R., Corsi, C. E., Burgarella, D., & Laget, M. 1997, A&A, 324, 915.

Ferraro, F. R., Paltrinieri, B., Fusi Pecci, F., Rood, R. T., & Dorman, B. 1998, ApJ, 500, 311.

Ferraro, F. R., Paltrinieri, B., Rood, R. T., & Dorman, B., 1999, ApJ, 522, 983.

Fusi Pecci, F. & Bellazzini, M. 1998, in *The Third Conference on Faint Blue Stars*, (Cambridge: Cambridge Univ. Press), 255.

Fusi Pecci, F., Ferraro, F. R., Corsi, C. E., Cacciari, C., & Buonanno, R. 1992, AJ, 104, 1831.

Fusi Pecci, F., Ferraro, F. R., Bellazini, M., Djorgovski, S. G., Piotto, G., & Buonanno, R. 1993, AJ, 105, 1145.

Gigas, D. 1986, A&A, 165, 170.

Glaspey, J. W., Michaud, G., Moffat, A. F., & Demers, S. 1989, ApJ, 339, 926.

Gonzalez, G. & Laws, C. 2000, AJ, 119, 390.

Gonzalez, J.-F., LeBlanc, F., Artru, M.-C., & Michaud, G. 1995, A&A, 297, 223.

Greenstein, G. S., Truran, J. W., & Cameron, A. G. W. 1967, Nature, 213, 871.

Grevesse, N. & Sauval, A. J. 1998, *Space Science Reviews*, 85, 161.

Grundahl, F., Catelan, M., Landsman, W. B., Stetson, P. B., & Andersen, M. I. 1999, ApJ, 524, 242.

Harris, W.E. 1996, AJ, 112, 1487.

Hawarden, T. G. 1971, *Obs*, 91, 78.

Heber, U. 1987, in *The Third Conference on Faint Blue Stars*, (Schenectady: L. Davis Press), 79.

Ivans, I. I., Sneden, C., Kraft, R. P., Suntzeff, N. B., Smith, V. V., Langer, G. E., & Fulbright, J. P. 1999, AJ, 118, 1273.

Kraft, R. P., Sneden, C., Smith, G. H., Shetrone, M. D., Langer, G. E., & Pilachowski, C. A. 1997, AJ, 113, 279.

Kurucz, R. 1997, in *Fundamental Stellar Properties, Proceedings of IAU Colloquium No. 189*, (Dordrecht: Kluwer Academic Publishers), 217.

Kurucz, R. & Bell, B. 1995, *Atomic Line Data, CD-ROM No. 23.*

Laget, M., Ferraro, F. R., Paltrinieri, B., & Fusi Pecci, F. 1998, *A&A*, 332, 93.

Lambert, D. L., McWilliam, A., & Smith, V. V. 1992, ApJ, 386, 685.

Lebreton, Y., Perrin, M.-N., Cayrel, R., Baglin, A., & Fernandes, J. 1999 A&A, 350, 587.

Lee, Y.-W., Demarque, P., & Zinn, R. J. 1994, ApJ, 423, 248.

Libbrecht, K. G. & Peri, M. 1995, PASP, 107, 62.

Malatich, J. M. 1999, *Revelations of Gravity and World Order*, (Burlington: Xerox Publications).

McCarthy, J. K. 1988, Ph.D. thesis, California Institute of Technology.

McCarthy, J. K. 1990, *Proc. 2nd ESO/ST-ECF Data Analysis Workshop*, (Garching: European Southern Observatory), 119.

McCarthy, J. K., Sandiford, B. A., Boyd, D., & Booth, J. 1993, PASP, 105, 881.

Mengel, J. G. & Gross, P. G. 1976, APSS, 41, 407.

Moehler, S., Heber, U., & DeBoer, K. S. 1995, A&A, 294, 65.

Moehler, S., Heber, U., & Durrell, P. R. 1997, A&A, 317, L83.

Moehler, S., Heber, U., & Rupprecht, G. 1997, A&A, 319, 109.

Moehler, S., Sweigart, A. V., & Catelan, M. 1999, A&A, 351, 519.

Moehler, S., Sweigart, A. V., Landsman, W. B., Heber, U., & Catelan, M. 1999, A&A, 346, 1.

Newell, E. B. 1973, ApJS, 26, 37.

Oke, J. B. & Gunn, J. E. 1982, PASP, 94, 586.

Oke, J. B. & Gunn, J. E. 1983, ApJ, 266, 713.

Peterson, R. C. 1983, ApJ, 275, 737.

Peterson, R. C. 1985, ApJ, 289, 320.

Peterson, R. C. 1985, ApJL, 294, 35.

Peterson, R. C., Rood, R. T., & Crocker, D. A. 1995, ApJ, 453, 214.

Pinsonneault, M. H., Deliyannis, C. P., & Demarque, P. 1991, ApJ, 367, 239.

Piotto, G., Zoccali, M., King, I. R., Djorgovski, S. G., Sosin, C., Rich, R. M., & Meylan, G. 1999, AJ, 118, 1727.

Press, W. H., Teukolsky, S. A., Vetterling, W. T., & Flannery, B. P. 1992, *Numerical Recipes in C, The Art of Scientific Computing, Second Edition*, (Cambridge University Press: Cambridge), p. 623.

Queloz, D., Allain, S., Mermilliod, J., Bouvier, J., & Mayor, M. 1998, A&A, 335, 183.

Rich, R. M., Sosin, C., Djorgovski, S. G., Piotto, G., King, I. R., Renzini, A., Phinney, E. S., Dorman, B., Liebert, J., & Meylan, G. 1997, ApJ, 484, L25.

Richer, J., Michaud, G., & Turcotte, S. 2000, ApJ, 529, 338.

Rood, R. T. & Seitzer, P. O. 1981, in *Astrophysical Parameters of Globular Clusters, IAU Colloq. 68*, 369.

Sandage, A. 1953, AJ, 58, 61.

Sandage, A. 1969, ApJ, 157, 515.

Sandage, A. & Walker, A. 1966, ApJ, 143, 313.

Sandage, A. & Wallerstein, G. 1960, ApJ, 131, 598.

Sandage, A. & Wildey, R. 1967, ApJ, 150, 469.

Sargent, W. L. W. & Searle, L. 1967, ApJL, 150, 33.

Savedoff, M. P. 1956, AJ, 61, 254.

Schuster, W. J., Parrao, L., & Contreras Martinez, M. E. 1993, A&AS, 97, 951.

Searle, L. & Zinn, R. 1978, ApJ, 225, 357.

Seaton, M. J. 1997, MNRAS, 289, 700.

Shectman, S. A. 1988, unpublished, but see Section 2 of McWilliam, A., Preston, G., Sneden, C., & Shectman, S. A 1995, AJ, 109, 2736.

Shetrone, M. D. 1996, AJ, 112, 1517.

Shortridge, K. 1993, *The Figaro 2.4 Manual.*

Siess, L. & Livio, M. 1999, MNRAS, 308, 1133.

Sills, A. & Pinsonneault, M. H. 1999, astro-ph 9911024.

Soker, N. 1998, AJ, 116, 1308.

Soker, N. & Harpaz, A. 1999, astro-ph 9911003.

Sosin, C., Dorman, B., Djorgovski, S. G., Piotto, G., Liebert, J., Phinney, E. S. & Renzini, A. 1997, ApJ, 480, L35.

Stetson, P. B. & Vandenberg, D. A. 1996, PASP, 108, 560.

Sweigart, A. V. 1997, ApJL, 474, 23.

Sweigart, A. V. 2000, private communication.

Sweigart, A. V. & Catelan, M. 1998, ApJL, 501, 63.

Thevenin, F. & Idiart, T. P. 1999, ApJ, 521, 753.

Turcotte, S., Richer, J., & Michaud, G. 1998, ApJ, 504, 559.

van den Bergh, S. 1967, AJ, 72, 70.

Vink, J. S., Heap, S. R., Sweigart, A. V., Lanz, T., & Hubeny, I. 1999, A&A, 345, 109.

Vogt, S. E., Allen, S., Bigelow, B., Bresee, L., Brown, B., Cantrall, T., Conrad, A., Couture, M., Delaney, C., Epps, H., Hilyard, D., Horn, E., Jern, N., Kanto, D., Keane, M., Kibrick, R., Lewis, J., Osborne, C., Osborne, J., Pardeilhan, G., Pfister, T., Ricketts, T., Robinson, L., Stover, R., Tucker, D., Ward, J., & Wei, M. 1994, *SPIE*, 2198, 362.

Walker, A. 1994, AJ, 108, 555.

Yi, S., Lee, Y.-W., Woo, J.-H., Park, J.-H., Demarque, P., & Oemler, A. 1999, ApJ, 513, 128.

Zinn, R. & West, M. J. 1984, ApJS, 55, 45.

Zoccali, M. 1998, private communication.